GOETHE UNIVERSITÄT FRANKFURT AM MAIN

Large-eddy simulations of the mountain boundary layer: Daytime exchange processes and nocturnal fog formation

Dissertation
zur Erlangung des Doktorgrades
der Naturwissenschaften

vorgelegt beim Fachbereich 11 Geowissenschaften/Geographie
der Johann Wolfgang Goethe-Universität
in Frankfurt am Main

von
Jan Weinkaemmerer

aus Würzburg

Frankfurt am Main, 2023
(D30)

Vom Fachbereich 11 Geowissenschaften/Geographie der
Johann Wolfgang Goethe-Universität als Dissertation angenommen.

Dekan:
Prof. Dr. Jürgen Runge

Gutacher:
Prof. Dr. Jürg Schmidli
Prof. Dr. Mathias Rotach

Datum der Disputation:

Abstract

In this dissertation, different aspects of turbulent transport and thermally driven flows over complex terrain are investigated. Two publications concentrate on the vertical heat and moisture exchange in the convective boundary layer over mountainous terrain. To study this, Large-Eddy Simulation (LES) is used. Both turbulent and advective transport mechanisms are evaluated over the simple orography of a quasi-two-dimensional, periodic valley with prescribed surface fluxes. Here, terrain elevation varies along only one of the horizontal coordinate axes. Even a relatively shallow orography, possibly unresolved in existing numerical weather prediction models, modifies the domain-averaged moisture and temperature profiles. For the analysis, the flow is decomposed into a local turbulent part, a local mean circulation, and a large-scale part. An analysis of the turbulent kinetic energy and turbulent heat and moisture flux budgets shows that the thermal circulation significantly contributes to the vertical transport. It is found that thermal upslope winds are important for the moisture transport from the valley to the mountain tops. In total, moisture export out of the valley is mostly accomplished by the mean circulation. On the temperature distribution, which is horizontally relatively homogeneous, the thermal circulation has a weaker impact. If an upper-level wind is present, it interacts with the thermal circulation. This weakens the vertical transport of moisture and thus reduces its export out of the valley. The heat transport is less affected by the upper-level wind because of its weaker dependence on the thermal circulation. These findings were corroborated in a more realistic experiment simulating the full diurnal cycle using radiation forcing and an interactive land surface model.

Based on these results, coherent turbulent structures in the convective boundary layer over non-flat terrain are studied in further detail. A conditional sampling method based on the concentration of a decaying passive tracer is implemented in order to identify the boundary-layer plumes objectively. Conditional sampling allows to quantify the contribution of plume structures to the vertical transport of heat and moisture. In case of the idealized valley, vertical transport by coherent structures is the dominant contribution to the turbulent components of both heat and moisture flux. It is comparable in magnitude to the advective transport by the mean slope-wind cir-

culation, although it is more important for heat than for moisture transport. A set of less idealized simulations considers the flow over three-dimensional terrain. In this case, conditional sampling is carried out by using a simple domain-decomposition approach. We demonstrate that thermal updrafts are generally more frequent on hill tops than over the surroundings, but they are less persistent on the windward sides when large-scale winds are present in the free atmosphere.

The tools for flow decomposition and budget analysis are also applied in another idealized case with a quasi-two-dimensional valley featuring the stable boundary layer. Here, the formation of a low stratus cloud is investigated. The main driver for the cloud formation is radiative cooling due to outgoing longwave radiation. Despite a purely horizontal flow, the advection terms in the prognostic equations for heat and moisture produce vertical mixing across the upper cloud edge leading to a loss of cloud water content. However, this behavior is not due to any kind of thermally-driven circulation. Instead, this spurious mixing is caused by the diffusive error of the advection scheme in regions where the sloping surfaces of the terrain-following vertical coordinate intersect the cloud top. It is shown that the intensity of the (spurious) numerical diffusion strongly depends on the horizontal resolution, the order of advection, and the choice of the scalar advection scheme. A LES with 4 m horizontal resolution serves as a reference. For horizontal resolutions of a few hundred meters, carried out with a model setup as it is used in Numerical Weather Prediction, a strong reduction of the simulated liquid-water path is observed. In order to keep the (spurious) numerical diffusion at coarser resolutions small, at least a fifth-order advection scheme should be used. In the present case, a WENO scalar advection scheme turns out to increase the numerical diffusion along a sharp cloud edge compared to an upwind scheme. Furthermore, the choice of the vertical coordinate has a strong impact on the simulated liquid-water path over orography. With a modified definition of the terrain-following sigma coordinate, it is possible to produce cloud water where the classical sigma coordinate does not allow any cloud formation.

Kurzzusammenfassung

In dieser Dissertation werden verschiedene Aspekte des turbulenten Transports und des Hangwindsystems über komplexem Gelände untersucht. Zwei Teilveröffentlichungen konzentrieren sich auf den vertikalen Wärme- und Feuchteaustausch in der konvektiven Grenzschicht über Gebirgslandschaften. Dazu werden Large-Eddy-Simulationen (LES) durchgeführt. Sowohl turbulente als auch advektive Transportmechanismen werden über der einfachen Orographie eines quasi-zweidimensionalen, periodischen Tals mit vorgegebenen Oberflächenflüssen untersucht. In diesem Fall variiert die Höhe des Geländes nur entlang einer der horizontalen Koordinatenachsen. Selbst eine relativ kleinskalige Orographie, die in bestehenden numerischen Wettervorhersagemodellen möglicherweise nicht berücksichtigt ist, verändert die gemittelten Feuchte- und Temperaturprofile des Gebiets. Für die Analyse wird die Strömung in einen turbulenten Teil, eine lokale mittlere Zirkulation und einen großräumigen Teil zerlegt. Eine Analyse der turbulenten kinetischen Energie und der turbulenten Wärme- und Feuchteflüsse zeigt, dass die thermisch angetriebene Hangwindzirkulation wesentlich zum vertikalen Transport beiträgt. Es wird festgestellt, dass thermische Hangaufwinde für den Feuchtetransport vom Tal zu den Berggipfeln wesentlich sind. Insgesamt wird der Feuchteexport aus dem Tal hauptsächlich durch die Hangwindzirkulation bewirkt. Auf die Temperaturverteilung, die horizontal relativ homogen ist, hat die thermisch angetriebene Zirkulation einen schwächeren Einfluss. Wenn ein Höhenwind vorhanden ist, interagiert er mit der thermischen Zirkulation. Dadurch wird der vertikale Feuchtetransport reduziert und somit der Export von Feuchte aus dem Tal verringert. Der Wärmetransport wird durch den Höhenwind weniger beeinflusst, da er weniger stark von der thermischen Zirkulation abhängt. Diese Ergebnisse wurden in einem weniger idealisierten Experiment bestätigt, bei dem der gesamte Tageszyklus mit Hilfe von Strahlungsantrieben und einem interaktiven Landoberflächenmodell simuliert wurde.

Auf Grundlage dieser Ergebnisse werden kohärente turbulente Strukturen in der konvektiven Grenzschicht über nicht-flachem Terrain näher untersucht. Um die Grenzschicht-Plumes objektiv zu identifizieren, wird eine Conditional-Sampling-Methode basierend auf der Konzentration eines abklingenden passiven Tracers eingesetzt. Das

Conditional Sampling ermöglicht es, den Beitrag der Plume-Strukturen zum vertikalen Transport von Wärme und Feuchte zu quantifizieren. Im Falle des idealisierten Tals ist der vertikale Transport durch kohärente Strukturen der dominierende Beitrag zum turbulenten Anteil des Wärme- und Feuchteflusses. Er ist von der Größenordnung her vergleichbar mit dem advektiven Transport durch die Hangwindzirkulation, wobei er für den Wärmetransport von größerer Bedeutung ist. Eine Reihe von weniger idealisierten Simulationen berücksichtigt die Strömung über dreidimensionalem Gelände. In diesem Fall wird das Conditional Sampling mit Hilfe eines einfachen Gebietszerlegungsansatzes durchgeführt. Wir zeigen, dass thermische Aufwinde im Allgemeinen auf Berggipfeln häufiger auftreten als in der Umgebung, sie aber auf der Luvseite weniger anhaltend sind, sofern in der freien Atmosphäre ein großräumiger Wind vorherrschend ist.

Die Vorgehensweise bei der Strömungszerlegung und Budgetanalyse wird auch in einem anderen idealisierten Fall mit einem quasi-zweidimensionalen Tal innerhalb der stabilen Grenzschicht angewandt. Hier wird die Bildung einer niedrigen Stratuswolke untersucht. Der Hauptantrieb für die Wolkenbildung ist die Strahlungskühlung durch die ausgehende langwellige Strahlung. Trotz einer rein horizontalen Strömung führen die Advektionsterme in den Prognosegleichungen für Wärme und Feuchte zu einer vertikalen Durchmischung am oberen Wolkenrand, was zu einem Verlust an Wolkenwasser führt. Dieses Verhalten ist jedoch nicht auf irgendeine Art von thermisch angetriebener Zirkulation zurückzuführen. Stattdessen wird diese unerwünschte Durchmischung durch den Diffusionsfehler des Advektionsschemas in Regionen verursacht, in denen die geneigten Koordinatenflächen der geländefolgenden Vertikalkoordinate die Wolkenoberseite schneiden. Es wird gezeigt, dass die Intensität der so verursachten numerischen Diffusion stark von der horizontalen Auflösung, der Ordnung der Advektion und der Art des skalaren Advektionsschemas abhängt. Eine LES mit einer horizontalen Auflösung von 4 m dient als Referenz. Bei horizontalen Auflösungen ab einigen hundert Metern, wie sie in der numerischen Wettervorhersage verwendet werden, wird eine starke Verringerung des simulierten Flüssigwassergehalts beobachtet. Um die numerische Diffusion bei gröberen Auflösungen klein zu halten, sollte mindestens ein Advektionsschema fünfter Ordnung verwendet werden. Im vorliegenden Fall stellt sich heraus, dass ein skalares WENO-Advektionsschema die numerische Diffusion entlang eines scharfen Wolkenrandes im Vergleich zu einem Upwind-Schema erhöht. Außerdem hat die Wahl der Vertikalkoordinate einen starken Einfluss auf den simulierten Flüssigwassergehalt. Mit einer modifizierten Definition der geländefolgenden Sigma-Koordinate ist es möglich, Wolkenwasser zu simulieren, wo die klassische Sigma-Koordinate keine Wolkenbildung zulässt.

Contents

Abstract **4**

Kurzzusammenfassung **6**

1 Introduction **13**

1.1 Thermally-induced advective and turbulent transport over mountainous terrain 14

1.2 Implications for boundary-layer parameterizations 15

1.3 Fog formation in the stable boundary layer over mountains 16

1.4 Numerical aspects of fog formation over rolling terrain 16

1.5 Goals and outline of the thesis 17

2 Model data and analysis methods **21**

2.1 Numerical model 21

2.2 Flow decomposition and averaging 21

3 The impact of large-scale winds on boundary-layer structure, thermally-driven flows, and exchange processes over mountainous terrain **23**

Jan Weinkaemmerer, Ivan Bašták Ďurán, Jürg Schmidli

3.1 Introduction 24

3.2 Analysis methods 27

3.2.1 Flow decomposition 27

3.2.2 Budgets for heat and mass 29

3.2.3 Budgets for TKE and turbulent fluxes 30

3.2.4 Boundary-layer structure 31

3.3 Numerical model simulations 31

3.3.1 Experimental setup 31

3.3.2 Numerical model 33

3.4 Analysis of the reference case 34

3.4.1 Flow structure 34

3.4.2 Temporal evolution . . . 35
3.4.3 Area-mean profiles . . . 36
3.4.4 Budget analysis . . . 40
3.5 Impact of an upper-level wind . . . 44
3.5.1 Flow structure and gravity waves . . . 44
3.5.2 Impact on temperature and moisture distribution . . . 46
3.6 Bulk heat and mass transport . . . 47
3.7 Conclusion . . . 49

4 Boundary-layer plumes over mountainous terrain in idealized large-eddy simulations 53

Jan Weinkaemmerer, Matthias Göbel, Stefano Serafin, Ivan Bašták Ďurán, Jürg Schmidli

4.1 Introduction . . . 54
4.2 Numerical model simulations . . . 57
4.2.1 Experimental setup . . . 57
4.2.2 Numerical model . . . 57
4.3 Analysis methods . . . 58
4.3.1 Conditional sampling . . . 58
4.3.2 Flow decomposition . . . 59
4.3.3 Joint probability density functions . . . 60
4.4 Analysis of the idealized-valley simulation . . . 62
4.4.1 Boundary-layer plume characteristics . . . 62
4.4.2 Heat and moisture flux decomposition . . . 63
4.4.3 JPDFs over the idealized valley . . . 65
4.4.4 Role of the slope-wind circulation . . . 67
4.5 Analysis of the three-dimensional simulations . . . 68
4.5.1 Reference case . . . 68
4.5.2 Impact of an upper-level wind . . . 70
4.6 Conclusions . . . 71

5 Stratus over rolling terrain: LES reference and sensitivity to grid spacing and numerics 75

Jan Weinkaemmerer, Ivan Bašták Ďurán, Stephanie Westerhuis, Jürg Schmidli

5.1 Introduction . . . 76
5.2 Budget analysis . . . 79
5.2.1 Flow averaging and decomposition . . . 79
5.2.2 Heat and water budgets . . . 80

5.3 Numerical model simulations 80
5.3.1 Experimental setup 80
5.3.2 Numerical model 81
5.4 Description of the LES reference 82
5.5 Sensitivity to resolution and advection scheme 84
5.5.1 Resolution dependence 84
5.5.2 Order of advection and WENO 88
5.5.3 Role of the vertical coordinate 89
5.6 Conclusion 89

6 Summary and conclusions **93**
6.1 Turbulent slope winds in the CBL over orography 93
6.2 Fog simulation in the SBL: Impact of resolution and numerics 97
6.3 General outlook 98

7 Zusammenfassung **101**
7.1 Turbulente Hangwinde in der konvektiven Grenzschicht über Orographie 101
7.2 Nebel-Simulation in der stabilen Grenzschicht: Einfluss von Auflösung und Numerik 105
7.3 Allgemeiner Ausblick 107

A CM1 implementations I: Budget computation **109**
A.1 Online calculation of LES statistics 109
A.2 Budgets for heat and moisture 111
A.3 Second-order turbulent moments 112

B CM1 implementations II: Conditional sampling of plumes **115**

Bibliography **117**

Chapter 1

Introduction

In the atmospheric boundary layer (ABL), the lowest layer of the atmosphere, the flow responds directly to the forcings from the Earth's surface. Because of the involved length and time scales, the ABL flows are mostly turbulent and understanding turbulent transport is crucial as it determines the vertical exchange of heat, mass, and momentum between the ground level and the free atmosphere. Due to the stochastic nature of turbulence, the flow variables can be decomposed into an ensemble-mean state and a fluctuating, turbulent part. Based on that, atmospheric flow models usually utilize some kind of averaged equations of motion to describe the transport of scalars and momentum. This means that a physical closure model has to be brought up in order to describe the impact of turbulence on the mean state. As such closure models mostly depend on only a few parameters of the flow, they are usually referred to as parameterizations. For grid sizes above typical ABL heights ($\approx 1\,\mathrm{km}$), it is sufficient for ABL parameterizations to cover only the vertical turbulent transport within the boundary layer as long as the underlying terrain is smooth and horizontal gradients are small (Teixeira et al., 2016). However, over distinct topography with length scales on the order of the ABL height, a variety of flow phenomena arise on the mesoscale and below, such as waves and secondary circulations, which are typically not included in ABL models. Consequently, the scales of the resolved atmospheric motions and the unresolved fluctuations are not sufficiently separated any more. This leads to modeling challenges, especially because the submesoscale phenomena ($< 2\,\mathrm{km}$) and the secondary circulations induced by terrain inhomogeneities are not completely random (Calaf et al., 2022). The spatial scales of the involved processes are determined by the landform, ranging from a single slope to an entire mountain range (Serafin et al., 2018). Over mountainous terrain, we can distinguish between dynamically forced exchange processes, such as gravity waves transporting energy and momentum (Nappo, 2013), and thermally-induced transport, which will be introduced in the next section.

1.1 Thermally-induced advective and turbulent transport over mountainous terrain

Generally, thermally-induced flows respond to differential heating over heterogeneous terrain. They are present especially in fair-weather conditions with weak synoptic forcing. On a scale of typically up to 20 km, anabatic uplsope winds develop as positive buoyancy is generated over the heated slopes in comparison to the cooler neighboring air on the same height level (Whiteman, 2000). During nighttime, the process reverses, leading to katabatic downslope winds. On a larger scale, along-valley breezes appear which are generated by hydrostatic pressure gradients resulting from temperature differences along the valley axis (Schmidli et al., 2009). For instance, an up-valley flow (down-valley during nighttime) can occur between a plain and a valley on a scale of 20 to 200 km (Teixeira et al., 2016). Due to the narrowed volume of air, the heating rates in a valley tend to be higher than over flat terrain (valley-volume effect, Neininger, 1982; Neininger and Liechti, 1984; Steinacker, 1984; Schmidli and Rotunno, 2010). This can be expressed by the topographic amplification factor. On the scale of an entire mountain range, the thermally-induced flows lead to a circulation between a plain and the mountains which is associated with advective and turbulent mixing processes causing vertical mass transport (Weissmann et al., 2005; Zardi and Whiteman, 2013). An example of that is cloud formation over mountains due to moisture convergence and a generally deeper convective boundary layer (CBL) which has also been confirmed by several experimental studies (Geerts et al., 2008; Demko et al., 2009). The work of Henne et al. (2004) used aircraft measurements to demonstrate the high exchange rate of air in the valley CBL associated with vertical mass transport (i.e. moisture and pollutants). In a subsequent study (Henne et al., 2005), the existence of an elevated moisture layer on the leeward side of an Alpine mountain range was explained by non-turbulent, advective transport. Another example is the Mesoscale Alpine Program (MAP)-Riviera field campaign (Rotach et al., 2004) leading to a study on the turbulent structure and the vertical heat exchange in a valley (Weigel and Rotach, 2004) followed by high-resolution modeling studies using large-eddy simulation (LES) for verification (e.g., Weigel et al., 2007).

LES resolve the large, energy-containing turbulent eddies explicitly and parameterize only the smaller ones using turbulence closure models assuming a turbulence energy cascade. For this thesis, we focus on the cross-valley circulation in the daytime CBL being the smallest closed circulation pattern over complex terrain and the closest to the small-scale turbulence. It consists of an upslope branch, a horizontal recirculation, and compensating subsidence over the valley center closing the circulation cell

(Vergeiner and Dreiseitl, 1987). Depending on the valley geometry, we encounter two or more vertically stacked circulation cells (Wagner et al., 2015). The resulting temperature profile often exhibits a three-layer thermal structure (Schmidli and Rotunno, 2010; Schmidli, 2013) with a valley mixed layer, a stable valley inversion, and an upper weakly stable layer followed by the free atmosphere. Schmidli (2013) showed that the high diurnal temperature amplitudes in valleys can be explained to a large extent by the valley-volume effect. From a detailed heat-budget analysis, it becomes clear that advective cooling by the slope winds and heating by subsidence over the valley mixed layer combined with overall turbulent heating lead to a relatively homogeneous heating rate inside the valley.

An essential part of convective turbulence are thermal updrafts and boundary-layer plumes in the CBL. Over flat terrain, such coherent turbulent structures have been shown to transport a major part of heat and moisture between the surface and the free atmosphere. LES can be used to explicitly resolve small-scale coherent motions down to the meter scale. It has been widely used to study both clear and cloudy boundary layers, often with the goal to improve parameterizations (Schumann and Moeng, 1991; Heus and Jonker, 2008). However, most existing studies about boundary-layer plumes are limited to flat terrain. Statistics of LES output can reveal how the total turbulent flux is partitioned between local and non-local components, i.e. diffusive and organized turbulence. To this end, updraft sampling methods were introduced for the identification of coherent structures (e.g., Couvreux et al., 2010). With regard to a possible parameterization development over complex terrain, it is especially interesting how the turbulent fluxes are partitioned between coherent transport and other turbulence at different locations in the valley and how this compares to flat terrain.

1.2 Implications for boundary-layer parameterizations

From the point of view of numerical weather prediction (NWP), a large part of the mountain wind system and especially the slope-wind circulation lies in a so-called gray zone where certain processes in NWP models are neither completely subgrid nor fully resolved (Chow et al., 2019). Gray-zone effects are critical in complex terrain where turbulence and convection parameterizations need to consider the terrain influence even though the orography may not be accurately represented due to coarse grid resolutions or numerical limitations over steep terrain. This also means that there is no clear spatial separation between subgrid turbulence and the resolved scale because of the secondary circulations (Calaf et al., 2022). Over poorly resolved terrain, neither the typical vertical temperature profile nor the slope-wind circulation can be reproduced

properly (Wagner et al., 2014). Errors in the predicted boundary-layer depth and the vertical exchange of heat and mass are the consequence. Early approaches such as the ALPTHERM model (Liechti and Neininger, 1994) account for a subgrid orography by the area-height distribution of a specified geographical region in order to reproduce the topographic amplification factor. However, the variety of the involved scales, their interactions, and the partitioning of the transport between turbulence and mean-flow advection are a challenging aspect for parameterization development.

1.3 Fog formation in the stable boundary layer over mountains

At nighttime, the surface energy balance becomes negative and the air stabilizes because of radiative cooling. This leads to downward katabatic winds over the slopes. Under these conditions, also cold-air pools can develop due to cold-air drainage. Both radiative cooling and the sinking of cooler air into the valleys can contribute to the formation of mountain or valley fog. Under strongly stable conditions, the flow is no longer fully turbulent which gives rise to wave-related mixing processes and small-scale organized motions (Serafin et al., 2018). For NWP models, the simulation of fog is challenging due to the variety of the involved physical processes such as radiation, small-scale motions, intermittent turbulence, microphysics, and land-atmosphere interaction (e.g., Van der Velde et al., 2010; Steeneveld et al., 2015). In particular, radiation fog develops in the stable nocturnal boundary layer (SBL) when the near-surface air cools below its dew-point temperature due to outgoing longwave radiation. Often this fog is lifted up and forms an elevated cloud layer referred to as a low stratus (Scherrer and Appenzeller, 2014). When it has grown vertically, radiative cooling at the top of the now optically thick fog causes turbulent mixing by negatively buoyant air leading to the formation of a nearly adiabatic lapse rate within the fog layer (Price, 2011, 2019).

1.4 Numerical aspects of fog formation over rolling terrain

LES approaches over idealized topography combined with detailed budget analyses may also help to increase process understanding in the SBL. Like in the CBL, only a few modeling studies focus on fog or low stratus over complex terrain (Bergot and Lestringant, 2019). In general, the NWP representation of low stratus over complex

terrain tends to suffer from inaccuracies not only from unresolved processes or inaccurate model physics. In particular, erroneous cloud dissipation can be observed in many cases which was investigated by Westerhuis et al. (2020) in a NWP study focusing on the Swiss Plateau. The spurious mixing between adjacent levels of the terrain-following vertical coordinate has been identified as the root cause for intensified fog dissipation in specific cases (Westerhuis et al., 2021). Over mountainous terrain, sloping coordinate surfaces intersect the typically flat cloud top of fog and low stratus leading to an increased artificial mixing between cloudy and cloud-free grid cells due to the numerical diffusion of the advection scheme. Knowing the effect of terrain-following vertical coordinates over a hilly topography, it is still to clarify how other numerical aspects like the type of the advection scheme and the order of advection influence the simulation of fog and low clouds over complex terrain. In a subproject of this dissertation, we investigate this aspect systematically and compare between rolling and flat terrain over a range of different horizontal grid spacings from the meter scale up to 1 km.

1.5 Goals and outline of the thesis

As stated above, there is a lack of detailed studies on the turbulence characteristics over complex terrain, especially on the interaction between turbulent motions and the large-scale flow. In contrast to flat terrain, secondary circulations appear over mountainous terrain on spatial scales between small-scale turbulent and large-scale atmospheric motions. On the scale of one ridge or a single hill, that is the thermally-induced slope-wind circulation called the local circulation within the scope of this study. This thesis wants to focus on idealized LES cases on the scale of one valley or a group of shallow hills. All aspects addressed in this study relate to the numerical modeling of ridge-scale processes over complex terrain, such as the vertical exchange of heat and moisture over a valley or the formation of an elevated fog layer. Different points are covered ranging from the evaluation of turbulence statistics to numerical aspects like advection schemes and terrain-following vertical coordinates. The main goals of this work are:

- To improve the understanding of vertical heat and moisture exchange over complex terrain and its sensitivity to the large-scale flow. Here, we distinguish between advective transport by the local circulation and small-scale turbulence. The latter comprises organized turbulent motions (coherent plume structures) and other turbulence. The aim is to investigate the interactions over a range of scales from a few tens of meters to several kilometers.

- To identify key issues and prerequisites important for possible future parameterization developments improving the representation of boundary-layer processes over complex terrain in large-scale climate or NWP models where the orography is only partly resolved.

- To increase the process understanding regarding the numerical aspects involved in the spurious dissipation of fog over complex terrain, i.e. the vertical-coordinate formulation, the advection scheme and the order of advection, as well as parameterized and resolved turbulence, and its resolution dependence.

Paper I (Weinkaemmerer et al., 2022a)
For this first paper, the flow decomposition into small-scale turbulence, the slope-wind circulation, and a large-scale wind is applied to the thermally-induced flow in an idealized valley. Flow budgets are investigated with respect to the vertical heat and moisture exchange and the impact of an upper-level wind. Budgets of second-order moments, i.e. the turbulent heat and moisture flux and the TKE, are analyzed as well.

Paper II (Weinkaemmerer et al., 2023, *submitted*)
Single updrafts mark the small-scale end of coherent motions in the CBL over complex terrain. Also, many boundary-layer parameterizations distinguish between vertical transport by updrafts and diffusive turbulent mixing. The aim of the paper is to identify boundary-layer plumes over complex terrain and clarify the partitioning of the vertical transport among plumes, other turbulence, and the slope-wind circulation as well as their interactions with the slope flow and an upper-level wind.

Paper III (Weinkaemmerer et al., 2022b)
For this publication, we switched to a nocturnal SBL case of fog formation over an idealized valley. The aim was to employ the budget-analysis tools to gain insights into the processes involved in spurious cloud dissipation over orography.

Appendix A
An extensive budget analysis-tool has been implemented into CM1 which was applied throughout the whole project. It is designed so that online, accumulative time averaging of prognostic or diagnostic model variables is possible and no vast amount of model output has to be written to the disk to deal with in post-processing. The spatial averaging was adapted to the actual experimental setup, i.e. whether the simulation was performed over a quasi-two-dimensional valley or over real, three-dimensional terrain. It is easily extendable and has been used to calculate the temporal and spatial aver-

ages of single quantities, variances and covariances, or higher-order turbulent moments.

Appendix B

A conditional sampling method based on a passive tracer has been implemented into CM1 in order to identify plume structures in the CBL. The spatial averaging method for the computation of the tracer statistics needs to account for the horizontal inhomogeneity over complex terrain. With the help of conditional sampling, turbulence can be further decomposed into coherent, organized motions and other turbulence. The results are presented in Paper II.

Chapter 2

Model data and analysis methods

2.1 Numerical model

The numerical simulations are performed using the CM1 model (Cloud Model 1, Bryan and Fritsch, 2002). CM1 is a nonhydrostatic, fully compressible numerical model that can be run in both LES and NWP mode. It uses terrain-following σ coordinates. Different options can be selected for the advection schemes. In particular, it is possible to choose between upwind and WENO schemes of different order (Wicker and Skamarock, 2002; Jiang and Shu, 1996). For the subgrid-scale turbulence closure in LES mode, a TKE scheme is used (Deardorff, 1980). The NWP simulations in Weinkaemmerer et al. (2022b) employ a boundary-layer parameterization. The model also provides different options for the surface layer and for the microphysics. Generally, the two CBL studies concentrate on the clear boundary layer with no cloud formation.

2.2 Flow decomposition and averaging

By means of spatial and temporal averaging, the flow is decomposed as shown in Weinkaemmerer et al. (2022a). In order to compute the turbulent fluxes, the turbulent fluctuation a' of a flow variable a is separated from the ensemble average $\overline{a}$ via Reynolds decomposition:

$$a = \overline{a} + a'. \tag{2.1}$$

Over the periodic, sinusoidal valley, the required ensemble average is approximated by an average in time and in the along-valley direction. Over three-dimensional orography, the computation of a spatial average is not straightforward without a symmetry axis of the terrain. Thus, the domain is divided into multiple subdomains. The ensemble mean is the average calculated over each subdomain.

In order to study the local, thermally-driven mean flow, the quantity's domain average $\langle\overline{a}\rangle$ can be removed from the ensemble average leaving a local component $\overline{a}_c$ describing the mean circulation:

$$\overline{a}_c = \overline{a} - \langle\overline{a}\rangle. \tag{2.2}$$

With this, a budget analysis can be performed where the contributions from turbulence and local mean flow are distinguished (see Appendix A).

Chapter 3

The impact of large-scale winds on boundary-layer structure, thermally-driven flows, and exchange processes over mountainous terrain

Jan Weinkaemmerer[1,2], Ivan Bašták Ďurán[1,2], Jürg Schmidli[1,2]

1 – Institute for Atmospheric and Environmental Sciences, Goethe University Frankfurt, Frankfurt/Main, Germany

2 – Hans Ertel Centre for Weather Research, Offenbach, Germany

Abstract

The vertical heat and moisture exchange in the convective boundary layer over mountainous terrain is investigated using large-eddy simulation. Both turbulent and advective transport mechanisms are evaluated over the simple orography of a quasi-two-dimensional, periodic valley with prescribed surface fluxes. For the analysis, the flow is decomposed into a local turbulent part, a local mean circulation, and a large-scale part. It is found that thermal upslope winds are important for the moisture export from the valley to the mountain tops. Even a relatively shallow orography, possibly unresolved in existing numerical weather prediction models, modifies the domain-averaged moisture and temperature profiles. An analysis of the turbulent kinetic energy and turbulent heat and moisture flux budgets shows that the thermal circulation significantly contributes to the vertical transport. This transport depends on the horizontal heterogeneity of the transported variable. Therefore, the thermal circulation has a stronger

impact on the moisture budget and a weaker impact on the temperature budget. If an upper-level wind is present, it interacts with the thermal circulation. This weakens the vertical transport of moisture and thus reduces its export out of the valley. The heat transport is less affected by the upper-level wind because of its weaker dependence on the thermal circulation. These findings were corroborated in a more realistic experiment simulating the full diurnal cycle using radiation forcing and an interactive land-surface model.

3.1 Introduction

Several publications point out the impact of thermally driven slope flows on the exchange of heat, mass, and momentum in the daytime convective boundary layer over mountainous terrain (Rotach et al., 2014; Serafin et al., 2018; Lehner and Rotach, 2018; Gohm et al., 2009). Anabatic upslope winds are generated by horizontal temperature contrasts between the valley sidewalls and the valley center resulting in positive buoyancy over the slopes (Whiteman, 2000). Apart from modifying the vertical profiles of temperature and moisture, thermally driven slope winds also control the transport and dispersion of pollutants over complex terrain (Gohm et al., 2009; Lehner and Gohm, 2010; Giovannini et al., 2020). Together with other baroclinic circulations forming the mountain wind system, they are present especially in fair-weather conditions with weak synoptic forcing. In contrast to the larger-scale along-valley breezes, which are generated by hydrostatic pressure gradients resulting from temperature differences along the valley axis (Schmidli et al., 2009), the smaller-scale slope flows respond directly to the surface sensible heat flux and are generally turbulent (Serafin and Zardi, 2010).

From a ridge-scale perspective, the slope-wind system appears as a cross-valley circulation consisting of an upslope branch, a partial recirculation to the valley center, and compensating subsidence in the stable core of the valley (Vergeiner and Dreiseitl, 1987). Depending on the valley geometry, we encounter two or more vertically stacked circulation cells (Wagner et al., 2015). The resulting temperature profile often exhibits a three-layer thermal structure (Schmidli and Rotunno, 2010; Schmidli, 2013) with a valley mixed layer, a stable valley inversion, and an upper weakly stable layer followed by the free atmosphere.

Compared to the atmosphere over flat terrain, the valley atmosphere heats up more strongly with the same energy input due to the so-called valley-volume effect (Neininger, 1982; Neininger and Liechti, 1984; Schmidli and Rotunno, 2010). This concept explains the higher heating rates by the reduced volume of air inside a valley. In flat terrain, a larger volume of air has to be heated up over the same area by the same

solar energy input. The valley-volume effect can also be quantified in terms of the area-height distribution of a valley (Steinacker, 1984). Using idealized large-eddy simulations (LESs), Schmidli (2013) has shown that the high diurnal temperature amplitudes in valleys can be explained to a large extent by the valley-volume effect. From a detailed heat-budget analysis, it is clear that advective cooling by the slope winds and heating by subsidence over the valley mixed layer combined with overall turbulent heating lead to a relatively homogeneous heating rate inside the valley. The total heating in the valley is reduced by a net export of heat out of the valley by overshooting thermals over the ridge tops.

Complementary to that work, other authors have concentrated on detailed analyses of tracer mass fluxes in idealized setups (Leukauf et al., 2016) or variable valley geometries with three-dimensional configurations of a valley with an adjacent plain (Wagner et al., 2015). Depending on stratification and surface heating, pollution can either be trapped inside a valley or released into the free atmosphere. This contrasting behavior is related to the internal energy necessary to break up the valley inversion. One notable result is that the tracer mass transport from the surface to the free atmosphere is three to four times more effective over valleys than over flat terrain (Wagner et al., 2015). In addition, vertical transport processes are found to be the strongest for deep and narrow valleys.

Another aspect, which is still subject to discussion, is the impact of thermally induced winds on moist convection in complex terrain. Different to mechanically forced orographic convection, the process understanding is still poor and even the influence of basic terrain scales on thermally forced orographic convection remains uncertain (Kirshbaum et al., 2018). While upslope flows may trigger convection by transporting water vapor from the valley floor to the ridge tops inducing moisture convergence (Banta, 1990), their cooling effect may also cause the contrary. Demko et al. (2009) argue that the advection of colder air along the slopes of a single mountain reduces the convective available potential energy (CAPE) thus inhibiting the initiation of convection. In contrast, Panosetti et al. (2016) come to the result that mass convergence and weaker convective inhibition (CIN) above mountains increase the probability of triggering convection. This is primarily due to the higher elevation of mountainous terrain in combination with water-vapor advection by upslope winds. Thus, convection initiation over mountain ridges may be enhanced or suppressed by thermal circulations depending on the given conditions (Schmidli, 2013).

From the point of view of numerical weather prediction (NWP), thermally-driven winds lie in a so-called gray zone where certain processes in the NWP models are neither completely subgrid nor fully resolved (Chow et al., 2019). Gray-zone effects are espe-

cially critical in complex terrain where turbulence and convection parameterizations need to consider the terrain influence even though the orography may not be accurately represented due to coarse grid resolutions or numerical limitations over steep terrain. Over a poorly resolved valley orography, neither the typical vertical temperature profile nor the slope-wind circulation can be reproduced properly (Wagner et al., 2014). Errors in the predicted boundary-layer depth and the vertical exchange of heat and mass are the consequence. Apart from the gray-zone problem, already the processes in a convective boundary layer (CBL) in a fairly idealized setup over a quasi-two-dimensional valley-ridge orography involve three different scales (Lehner and Rotach, 2018). First, small-scale turbulence dominating in the horizontally inhomogeneous mixed layer, second, the thermal cross-valley circulation, and third, an upper-level, geostrophic wind which can be treated as the large-scale flow given by the synoptic conditions.

The overall goal of our study is to gain insight into the interaction between these scales, with a special focus on the role of an upper-level wind on the vertical transport and exchange processes. This aspect has not yet received much attention in the literature. Catalano and Moeng (2010) have shown second-order turbulent moments and turbulent kinetic energy (TKE) budgets for a similar case, but only locally at different positions along the slope and not in presence of a large-scale background wind. Panosetti et al. (2016) have found that the convective updraft is shifted downstream from the summit in presence of a background wind, however, no general correlation to the updraft strength or the formation of precipitation has been determined.

With regard to a possible future parameterization development, we are not only interested in the local effects of the involved processes, but also in their impact on averaged quantities. Therefore, LES is used over a simple orography to analyze the vertical heat and moisture transport in more detail. We decompose the flow into three components: a turbulent part, a thermal circulation, and a large-scale flow in order to study their interactions. The influence of the upper-level wind on the vertical transport is analyzed. Because the main goal of boundary-layer models is the parameterization of heat and moisture fluxes, we take a close look at the budgets of these fluxes.

This paper is structured as follows: in the next section, the flow decomposition into turbulent part, thermal circulation, and large-scale flow, as well as the horizontal averaging method are introduced. Besides, the budget equations for TKE, turbulent sensible, and latent heat flux are presented. The experimental setup and the numerical model are presented in section 3.3. In the sections 3.4 to 3.6, the simulation results are discussed. Conclusions are given in section 3.7.

3.2 Analysis methods

3.2.1 Flow decomposition

With the aim to distinguish between local turbulent fluctuations, the thermal circulation, and the large-scale background flow, the flow is decomposed into these three components with the help of corresponding averaging operators. A sinusoidal valley flanked by two ridges is oriented along the meridional or y direction of the domain. Thus, the slope-wind circulation is supposed to be bound to the x-z plane forming a cross-valley circulation. Both in zonal and meridional direction, periodic boundary conditions are imposed, imitating an infinitely long valley. The symmetry of this quasi-two-dimensional setup used in this study simplifies the decomposition of the flow.

First, the turbulent fluctuations are separated from the mean flow by a Reynolds decomposition of the turbulent flow variable $a(x, y, z, t)$. Note that z denotes the height above the valley floor. The required ensemble (Reynolds) average is approximated by an average in time and in the along-valley direction:

$$\overline{a}(x, z, t) = \frac{1}{TL_y} \int_{t-T}^{t} \int_{0}^{L_y} a(x, y', z, t') \, \mathrm{d}y' \, \mathrm{d}t' \,, \tag{3.1}$$

where x, y, and z are the eastward, northward, and vertical direction, respectively; and t is time. An averaging time step of 1 min is used. The time-averaging interval T is set to 40 min. The same averaging period has been used in previous idealized studies of the convective boundary layer over orography (Catalano and Moeng, 2010; Schmidli, 2013) as a compromise between accuracy and stationarity. L_y equals the meridional domain length. Thus, the flow is decomposed into an ensemble mean part $\overline{a}$ and a local turbulent part a':

$$a(x, y, z, t) = \overline{a}(x, z, t) + a'(x, y, z, t). \tag{3.2}$$

For the sake of clarity, subgrid-scale fluctuations not resolved in the LES are not written out here and are treated as being included in the turbulent part.

The mean flow can be further decomposed into a local cross-valley circulation component and a large-scale background flow. This is achieved by averaging $\overline{a}$ between two crests along the x axis on horizontal levels of constant height above the valley floor:

$$\langle \overline{a} \rangle (z, t) = \frac{1}{L_x} \int_{0}^{L_x} \overline{a}(x', z, t) \, \mathrm{d}x' \,, \tag{3.3}$$

where L_x represents the zonal domain length equal to the valley width. In case of terrain-following coordinates, this requires interpolation. The further decomposition

results in:

$$\overline{a}(x,z,t) = \langle \overline{a} \rangle (z,t) + \overline{a}_c(x,z,t), \tag{3.4}$$

where the $\langle\rangle$ operator denotes the horizontal domain averaging and $\overline{a}_c$ is the mean local circulation which is the deviation of the ensemble mean $\overline{a}$ from the large-scale background flow $\langle \overline{a} \rangle$. For simplicity, this large-scale area mean $\langle \overline{a} \rangle$ is abbreviated with a_B. The complete decomposition of the flow into the three components can be represented as:

$$a = \overline{a} + a' = a_B + \overline{a}_c + a'. \tag{3.5}$$

Following the Reynolds averaging rules, the ensemble mean of a product is given by:

$$\overline{ab} = \overline{(\overline{a} + a')(\overline{b} + b')} = \overline{a}\overline{b} + \overline{a'b'}. \tag{3.6}$$

The domain-averaged ensemble mean of a product is then:

$$\langle \overline{ab} \rangle = \langle (a_B + \overline{a}_c)(b_B + \overline{b}_c) \rangle + \langle \overline{a'b'} \rangle = a_B b_B + \langle \overline{a}_c \overline{b}_c \rangle + \langle \overline{a'b'} \rangle. \tag{3.7}$$

Therefore, the total vertical transport of a quantity c can be expressed as:

$$\underbrace{\langle \overline{wc} \rangle}_{\text{total flux}} = \underbrace{\underbrace{w_B c_B}_{\text{large-scale flow}} + \underbrace{\langle \overline{w}_c \overline{c}_c \rangle}_{\text{mean circulation}}}_{\text{mean advective flux}} + \underbrace{\langle \overline{w'c'} \rangle}_{\text{turbulent flux}}, \tag{3.8}$$

where w is the vertical velocity. In a periodic setup with no large-scale horizontal gradients and no large-scale advection, the turbulent and mean-circulation fluxes are the only contributions to the total (vertical) transport in the domain.

Note that the second-order turbulent fluxes consist of a resolved and a subgrid-scale part:

$$\overline{a'b'} = \overline{a'b'}|_{res} + \overline{a'b'}|_{sgs}. \tag{3.9}$$

For the analysis, the subgrid parts are computed via a K-gradient ansatz analogous to Wagner et al. (2014). This reads, e.g., for a vertical scalar flux:

$$\overline{w'c'}|_{sgs} = -K \frac{\partial c}{\partial z}, \tag{3.10}$$

where the vertical diffusion coefficient for scalars K is determined by the LES subgrid turbulence model.

Higher-order turbulent moments can be calculated in the same way with the help

of second-order moments:

$$\overline{a'b'c'} = \overline{abc} - \overline{a}\overline{b}\overline{c} - \overline{a}\,\overline{b'c'} - \overline{b}\,\overline{a'c'} - \overline{c}\,\overline{a'b'}. \tag{3.11}$$

3.2.2 Budgets for heat and mass

The aim of this study is to analyze the net vertical transport in the valley. For this, the evolution of temperature and tracer mass needs to be quantified with the help of their budget equations. Because the vertical transport over complex terrain involves different scales, we want to analyze transport contributions separated into turbulent motion, local circulation and large-scale flow. Thus, a decomposition of the variables needs to be used when deriving their budget equations. We start from the conservation equations for momentum, heat, and moisture written in the Boussinesq approximation (Wyngaard, 2010):

$$\frac{\partial u_i}{\partial t} + u_j \frac{\partial u_i}{\partial x_j} = -\delta_{i3} g \frac{\tilde{\theta}_v}{\theta_{v,0}} - \frac{1}{\rho_0}\frac{\partial \tilde{p}}{\partial x_i}, \tag{3.12}$$

$$\frac{\partial \theta}{\partial t} + u_j \frac{\partial \theta}{\partial x_j} = S_\theta, \tag{3.13}$$

$$\frac{\partial q}{\partial t} + u_j \frac{\partial q}{\partial x_j} = S_q, \tag{3.14}$$

where $u_i = \{u, v, w\}$ are the wind components in zonal, meridional, and vertical direction, θ is the potential temperature, and q is the specific humidity. $\tilde{\theta}_v$ and $\tilde{p}$ are the deviation of the virtual potential temperature and the deviation of the pressure from a constant reference state. $\theta_{v,0}$ is the constant reference virtual temperature and ρ_0 is the constant reference density. S stands for any kind of source or sink term, e.g., originating from microphysical processes. Einstein summation convention is used. The flow is assumed to be incompressible and we have neglected rotation, viscosity, and molecular diffusivity. Inserting (3.2) into (3.13) and (3.14) and applying the averaging operators from (3.1) and (3.3) leads to the domain averaged ensemble-mean tendencies:

$$\frac{\partial \langle\overline{\theta}\rangle}{\partial t} = -\left\langle \overline{u}_j \frac{\partial \overline{\theta}}{\partial x_j} \right\rangle - \left\langle \overline{u'_j \frac{\partial \theta'}{\partial x_j}} \right\rangle + \langle\overline{S_\theta}\rangle, \tag{3.15}$$

$$\frac{\partial \langle\overline{q}\rangle}{\partial t} = \underbrace{-\left\langle \overline{u}_j \frac{\partial \overline{q}}{\partial x_j} \right\rangle}_{\text{CIRC}} \underbrace{- \left\langle \overline{u'_j \frac{\partial q'}{\partial x_j}} \right\rangle}_{\text{TURB}} + \underbrace{\langle\overline{S_q}\rangle}_{\text{PHYSICS}}. \tag{3.16}$$

The first term on the RHS is the advective transport by the mean flow. In absence of large-scale gradients, it reduces to a local transport by the mean circulation (CIRC).

The second and third term are the turbulent transport term (TURB) and a source or sink term by the microphysics (MP), respectively. In the LES analysis, the ensemble means and the sum of the above transport terms are computed directly from the model's prognostic equations during the model run by a method described in section 3.3.2. The cross-valley averages are calculated during post-processing. No additional approximation is applied to the model equations.

3.2.3 Budgets for TKE and turbulent fluxes

Analogously, the budget equations for the turbulence kinetic energy (TKE) and both the turbulent sensible and latent heat flux can be derived from the conservation equations. In contrast to the traditional derivation (e.g., Stull, 2012), additional terms emerge due to the three-component decomposition. Some budget terms are zero after horizontal averaging, thanks to the symmetry of the setup. The resulting budget equations resemble those for the boundary layer over flat terrain, except of additional terms representing the inter-scale transfer between turbulence and local circulation:

$$\frac{1}{2}\frac{\partial\langle\overline{u_i'^2}\rangle}{\partial t} = \underbrace{\frac{g}{\theta_{v,0}}\langle\overline{w'\theta_v'}\rangle}_{\mathrm{I}} - \underbrace{\langle\overline{u_i'w'}\rangle\frac{\partial u_{B,i}}{\partial z}}_{\mathrm{II}} - \underbrace{\left\langle\overline{u_i'u_j'}\frac{\partial\overline{u}_{c,i}}{\partial x_j} + \overline{u}_{c,j}\frac{1}{2}\frac{\partial\overline{u_i'^2}}{\partial x_j}\right\rangle}_{\mathrm{III}} - \underbrace{\frac{1}{2}\frac{\partial\langle\overline{w'u_i'^2}\rangle}{\partial z}}_{\mathrm{IV}} - \underbrace{\frac{1}{\rho_0}\frac{\partial\langle\overline{w'p'}\rangle}{\partial z}}_{\mathrm{V}} - \underbrace{\langle\epsilon\rangle}_{\mathrm{VI}}, \quad (3.17)$$

$$\frac{\partial\langle\overline{w'\theta'}\rangle}{\partial t} = \underbrace{\frac{g}{\theta_{v,0}}\left\langle\overline{\theta'\theta_v'}\right\rangle}_{\mathrm{I}} - \underbrace{\left\langle\overline{w'w'}\right\rangle\frac{\partial\theta_B}{\partial z}}_{\mathrm{II}} - \underbrace{\left\langle\overline{u_j'\theta'}\frac{\partial\overline{w}_c}{\partial x_j} + \overline{w'u_j'}\frac{\partial\overline{\theta}_c}{\partial x_j} + \overline{u}_{c,j}\frac{\partial\overline{w'\theta'}}{\partial x_j}\right\rangle}_{\mathrm{III}} - \underbrace{\frac{\partial\left\langle\overline{w'w'\theta'}\right\rangle}{\partial z}}_{\mathrm{IV}} + \underbrace{\frac{1}{\rho_0}\left\langle\overline{p'\frac{\partial\theta'}{\partial z}}\right\rangle}_{\mathrm{V}} - \underbrace{2\langle\epsilon_{w\theta}\rangle}_{\mathrm{VI}}, \quad (3.18)$$

where $j = 1, 3$ and $\overline{u}_{c,2} = 0$, as there is no mean circulation in the along-valley direction. The scale-interaction terms in (3.17) are marked as III. The two components in III represent the gradient production and the advection by the local circulation. The remaining terms on the RHS of (3.17) are the traditional TKE terms: term I is the buoyant production/consumption term, II the mean-gradient production term, IV the vertical turbulent transport term, V the pressure correlation term, and VI the dissipation term. The situation in (3.18) is analogous with VI being the molecular destruction

term. A budget equation for the domain-averaged turbulent moisture flux $\langle\overline{w'q'}\rangle$ looks similar to (3.18).

Technically, the dissipation term consists of the dissipation rate given by the subgrid turbulence model and the implicit diffusion arising from an odd-ordered advection scheme (Brown et al., 2000). In our case, the implicit-diffusion term can be received from the model's diagnostics. While the total resolved transport term (TRT = II + III + IV) and the individual terms II and IV are calculated directly from the model data, the interaction term III is obtained as the difference: TRT − II − IV. It is not decomposed any further.

3.2.4 Boundary-layer structure

In order to study the boundary-layer structure, we start from the bulk perspective. Classically, the daytime atmospheric boundary layer over flat terrain is subdivided into a diabatic surface layer, followed by a nearly neutral, turbulent mixed layer (ML), topped by a stable entrainment zone representing the transition between the ML and the free atmosphere (Stull, 2012). The top of the entrainment zone equals the height of the atmospheric boundary layer (ABL). We adopt this classification for our complex-terrain experiments and, following Schmidli (2013), define the ML height as the height where the vertical gradient of the along-valley averaged potential temperature first reaches a critical value of $\gamma_c = 0.001\,\mathrm{K\,m^{-1}}$, marking the lower boundary of the capping inversion. The ABL height is diagnosed by a simple maximum-gradient method. It is computed from the local instantaneous height where the vertical θ gradient reaches its maximum. In order to obtain the x-dependent ABL height, the instantaneous local heights are averaged in time and along the valley axis according to (3.1).

3.3 Numerical model simulations

3.3.1 Experimental setup

To simplify our budget analysis, the flow is investigated over a two-dimensional sinusoidal valley (Schmidli, 2013). The orography corresponds to an infinitely long, periodic valley and is described by:

$$z_s(x) = \frac{h}{2}\left(1 - \cos\frac{2\pi x}{W}\right), \tag{3.19}$$

where z_s is the surface height, h the ridge height from valley floor to crest, and W the width of the valley from ridge to ridge. The height h is set to 1500 m and the width

W to 20.48 km which corresponds to a relatively narrow and moderately deep valley. The maximum inclination of the slope is 13.0°.

To study the influence of the upper-level wind on the flow within the valley, experiments with different upper-level wind velocities are performed. In the reference experiment (REF), the background atmosphere is at rest. The remaining setup of the experiments, unless stated otherwise, is as follows: the initial atmosphere is in hydrostatic balance, the pressure is 1000 hPa at $z = 0$, and a linear and stable potential-temperature profile is prescribed by $\theta(z) = \theta_s + \Gamma z$ with $\Gamma = 0.003\,\mathrm{K\,m^{-1}}$ and $\theta_s = 297\,\mathrm{K}$ at the valley floor. A constant relative humidity of 40 % is imposed leading to a water-vapor mixing ratio decreasing with height. The surface forcing is constant in space and time in order to come closer to a steady state during the simulation. The surface sensible heat and moisture flux is prescribed: $(\overline{w'\theta'})_s = 0.12\,\mathrm{K\,m\,s^{-1}}$, $(\overline{w'q'})_s = 0.05\,\mathrm{g\,kg^{-1}\,m\,s^{-1}}$. In the reference case, no clouds are formed before 4 h 40 min and the ensemble averaged cloud-water mixing ratio does not exceed $9 \times 10^{-6}\,\mathrm{g\,kg^{-1}}$ during the rest of the simulation. Thus, water vapor can be approximately regarded as a passive tracer. Additionally, a simulation with exactly the same setup, but without orography is carried out for comparison (FLAT).

In the sensitivity experiments, the large-scale flow is initialized according to:

$$\langle \overline{u} \rangle(z) = \begin{cases} 0, & z \leq h, \\ \frac{z-h}{\Delta h}\, u_{max}, & h < z \leq h + \Delta h, \\ u_{max}, & z > h + \Delta h, \end{cases} \tag{3.20}$$

where $\langle \overline{u} \rangle(z)$ is perpendicular to the valley axis, $\Delta h = 400\,\mathrm{m}$, and u_{max} is the value of the upper-level wind. The sensitivity experiments are named U2, U4, and U8, with $u_{max} = 2\,\mathrm{m\,s^{-1}}$, $4\,\mathrm{m\,s^{-1}}$, and $8\,\mathrm{m\,s^{-1}}$, respectively. The zero wind below crest height avoids an immediate excitement of gravity waves and can be justified by interpreting (3.20) as a geostrophic wind independent of ABL processes. In order to facilitate the onset of convective turbulence, the initial atmosphere is altered by a random temperature perturbation with a maximum amplitude of 0.5 K.

The domain sizes for the basic experiments are listed in Tab. 3.1. The total duration of the simulations is 6 h. We lay a special focus on the situation after 4 h assuming it to be representative for typical midday conditions (Schmidli, 2013). In section 3.6, the findings obtained with these idealized settings are compared against a case with spatially varying and time-dependent surface fluxes including radiation and an interactive land-surface model. This extended case is integrated over one diurnal cycle.

Table 3.1: List of basic experiments where u_{max} denotes the maximum background wind speed.

experiment	domain size	depth of sponge layer	u_{max}
FLAT/REF	$20.48 \times 10.24 \times 5\,\mathrm{km}$	1 km	0
U2	$20.48 \times 10.24 \times 8\,\mathrm{km}$	2 km	$2\,\mathrm{m\,s^{-1}}$
U4	$20.48 \times 10.24 \times 12\,\mathrm{km}$	3 km	$4\,\mathrm{m\,s^{-1}}$
U8	$20.48 \times 10.24 \times 12\,\mathrm{km}$	3 km	$8\,\mathrm{m\,s^{-1}}$

3.3.2 Numerical model

The numerical simulations were performed using CM1 (Cloud Model 1, Bryan and Fritsch, 2002; Bryan, 2016) in LES mode. CM1 is a nonhydrostatic, fully compressible numerical model with terrain-following σ_z coordinates. For this study, fifth order horizontal and vertical advection using a WENO scheme for scalars (Jiang and Shu, 1996) and the Klemp-Wilhelmson vertically implicit time splitting scheme is chosen. The subgrid-scale turbulence closure is a 1.5-order TKE scheme similar to Deardorff (1980). The horizontal grid resolution is set to 40 m. The lateral boundary conditions are periodic in both directions in order to mimic a vast mountainous terrain with a single terrain wave length. Grid stretching is applied in the vertical starting from 8 m vertical grid spacing near the surface. Increasing with height, it reaches 40 m at 2.8 km height and is kept constant above. The domain top is a rigid lid and its height is chosen depending on the initial upper-level wind speed (see Tab. 3.1). In order to suppress spurious gravity-wave reflections, a wave-damping sponge layer is employed in all cases. The setup of the wave-damping layer was adapted for each case accordingly because the vertical wavelength of the dominant gravity wave modes was found to be roughly proportional to the background wind speed. The damping time for the Rayleigh damping layer is 300 s for all cases. No radiation is included in the basic simulations. As sensible and latent heat fluxes are prescribed at the surface, no complex land-surface model is required. Only the momentum fluxes are computed from the exchange coefficient for momentum corresponding to a neutral surface layer and a roughness length of $z_0 = 0.16\,\mathrm{m}$. For the microphysics, a simple single-moment warm-rain scheme is selected (Kessler). The adaptive time step usually lies between 1 s and 2 s.

The starting time of the simulation for the diurnal-cycle case (section 3.6) is set to 21 March at 6 UTC. A longitude of 0°and a latitude of 55° is chosen for the NASA-Goddard radiation scheme. Thus, the 12 h integration time covers the daytime period. The land-use is set to grassland for the surface model (revised MM5 scheme, Jiménez et al., 2012). Although the surface characteristics do not change with the height of the orography, the surface heat fluxes are time and position dependent due to the

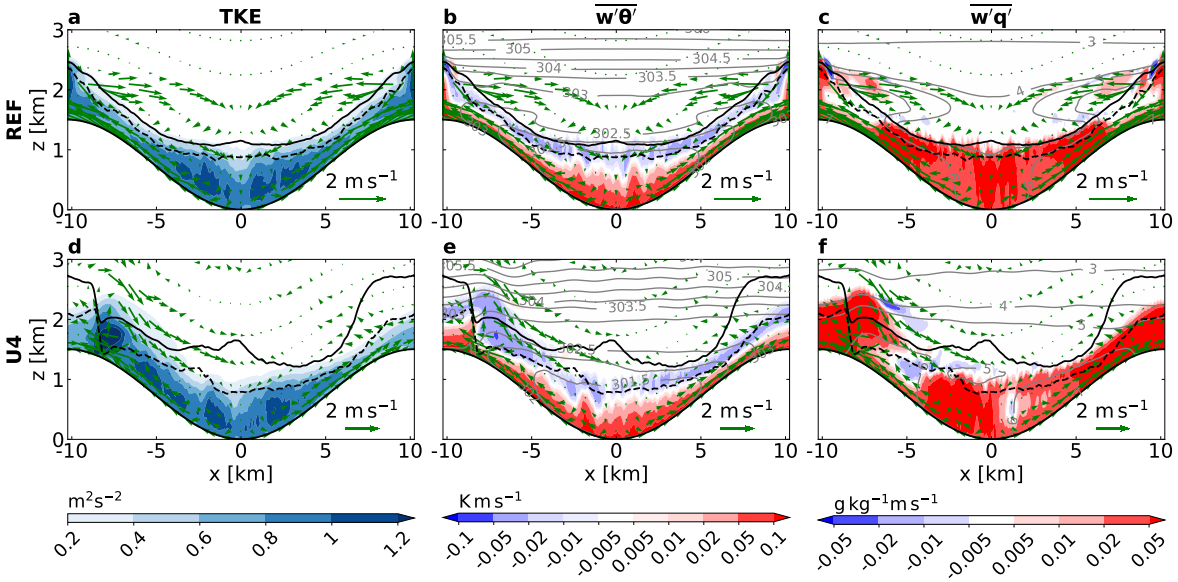

Figure 3.1: Valley cross sections of the mean flow at 4 h for (a)-(c) REF and (d)-(f) U4, showing the cross-valley wind vectors (at every tenth grid point in x and z direction) and in shading the TKE, the turbulent sensible heat flux, and the turbulent moisture flux (with all quantities including the subgrid contribution). Also shown is the potential temperature (center column, contour interval 0.5 K) and the specific humidity (right column, contour interval 1 g kg^{-1}). The dashed line marks the diagnosed ML height and the solid line the diagnosed ABL height.

movement of the sun. All other parameters are the same as for the simulations REF and U4.

An additional module has been implemented into CM1 allowing the online computation of time averages by recursion without the need to write any instant values to the disk (see Appendix). The mean values are updated recursively during runtime over an averaging period. These are then further averaged along the y axis before they are written out. This online calculation of the statistics reduces the required amount of disk space for the output files and replaces an otherwise expensive and time-intensive post-processing.

3.4 Analysis of the reference case

3.4.1 Flow structure

Figure 3.1a-c shows the local circulation and key turbulence quantities for the reference case after 4 h, together with the diagnosed ML and ABL heights. Note that the ML and ABL are deepest at the valley center and over the ridges. This is where the turbulence is most intense (largest TKE values). The turbulent sensible heat flux is positive near

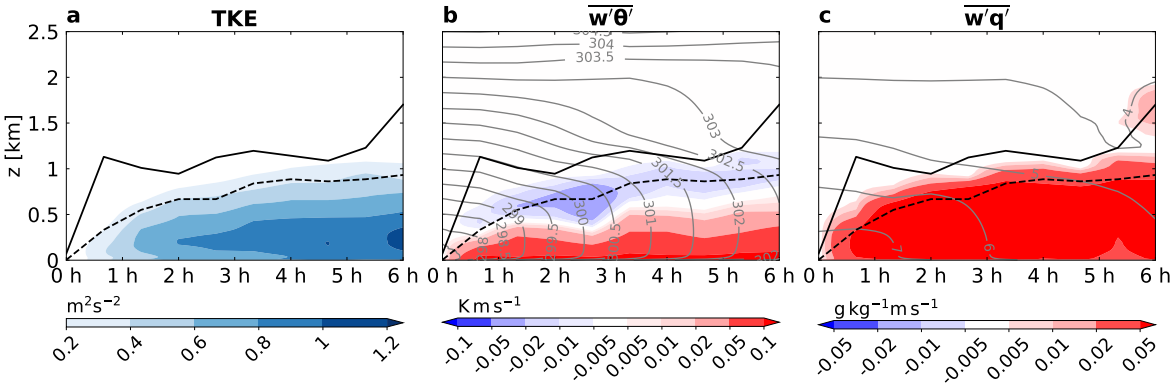

Figure 3.2: As in Fig. 1, but for the temporal evolution of the quantities at the valley center ($x = 0$).

the surface, decreases with height, and becomes negative in the upper part of the ML. The turbulent moisture flux is positive almost everywhere in the ABL, with the largest values inside the valley. The local circulation consists of a shallow upslope flow and an upper recirculation with subsidence over the valley center. Around halfway up the slope, an additional horizontal branch appears (horizontal intrusion, Leukauf et al., 2016).

The thermally-driven local circulation is partly induced by horizontal temperature gradients and consequently acts to weaken them. Cooling by ascent in the slope-wind layer and heating by subsidence in the valley core combined with overall turbulent heating leads to a rather homogeneous temperature distribution. The situation is different for moisture, since it does not have a significant impact on the flow dynamics. In the present context without cloud formation, the specific humidity is conserved under vertical motions and can thus be treated approximately as a passive tracer, except for its influence on the buoyancy term in the momentum equation (3.12). In addition to that, the initial specific humidity profile decreasing with height favors a net transport of moisture from the lower part of the valley to the ridges. This leads to a drying in the valley center and an accumulation of moisture above the ridges (see also Kuwagata and Kimura, 1997). This process increases the horizontal moisture gradient in and above the valley.

3.4.2 Temporal evolution

The temporal evolution of the TKE, the turbulent sensible heat flux, and the moisture flux at the valley center is shown in Fig. 3.2. Although the moisture-flux gradient leads to a moister valley ML compared to a rather dry free atmosphere, the valley center becomes gradually drier during the simulation. The ABL grows strongly and

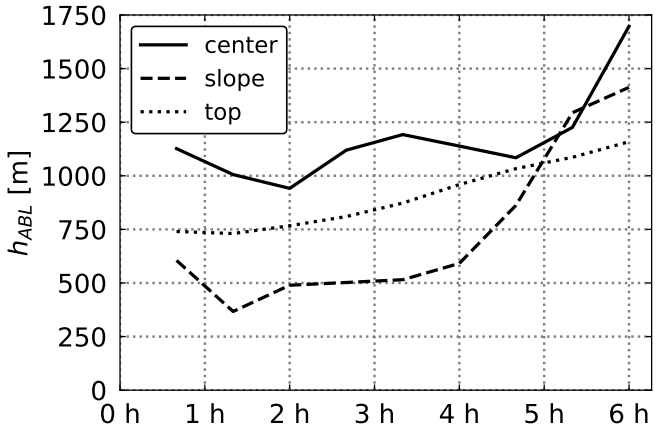

Figure 3.3: Temporal evolution of the ABL height above ground level at the valley center ($x = 0$), at the slope ($x = 5.12\,\mathrm{km}$), and at the ridge top ($x = 10.24\,\mathrm{km}$).

the temperature profile becomes nearly adiabatic near the end of the simulation. This corresponds to the break-up of the valley inversion.

Figure 3.3 shows the ABL height above ground level at the valley center, the ridge top, and over the slope midway between the valley center and the ridge top. Because of the constant surface fluxes, the ABL continuously grows over the ridges. In contrast, the ABL height at the valley center is only slowly increasing and remaining around 1000 m within the first 5 h. Over the slopes, the ABL height also stays almost constant at 500 m in the first 4 h indicating a nearly steady state. As the valley ABL continues to grow, we find a strong increase of the ABL height over the slope after 4 h of integration. With the breakdown of the valley inversion after around 5 h, the ABL height in the valley center also increases rapidly. At the end of the simulation, the ABL both over the valley center and over the slopes is deeper than over the ridge tops. The following analysis focuses on the situation after 4 h of integration, when the flow is in a quasi-steady state.

3.4.3 Area-mean profiles

Deep valley (1500 m)

To see the impact of the turbulent exchange and the local circulation on the large-scale quantities, the area-mean profiles of wind, potential temperature, and specific humidity are computed by horizontal averaging over the whole domain. These profiles are depicted in Fig. 3.4a-c.

The temperature and humidity profiles in all cases with orography are more structured compared to the FLAT case. This is caused by the cellular character of the flow

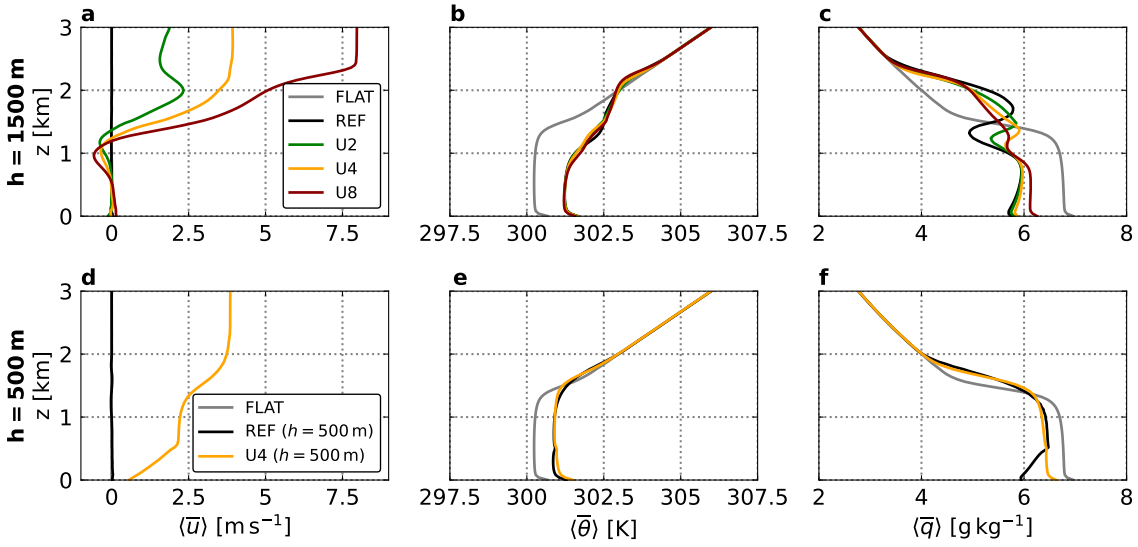

Figure 3.4: Area-mean profiles (height above valley floor) at 4 h of the zonal wind u, the potential temperature θ, and the specific humidity q for (a)-(c) the deep valley and (d)-(f) the shallow valley.

in the valley (cf. Schmidli, 2013). Due to the valley volume effect, the temperature profile is warmer for all cases with orography. The humidity profile is dryer in the ML and moister above the ML because moisture is transported out of the valley by the slope winds and accumulates over the mountain tops.

The difference in the transport of heat and moisture can also be seen from the decomposed vertical heat and moisture fluxes (Fig. 3.5g-i and j-l) and from the budgets of heat and moisture (see section 3.4.4). Heat is transported mainly by turbulent mixing. The local circulation has a smaller impact on the heat transport, since the temperature distribution evolves to be relatively horizontally homogeneous. In contrast, the local circulation dominates the transport of moisture, as it exports moisture from the valley center to the ridges. For the momentum flux (Fig. 3.5d-f), however, both the turbulent and the circulation part is zero in the REF case due to the symmetry of the flow in a symmetric valley.

The intensity of turbulent mixing represented by the TKE (Fig. 3.5a) shows an additional secondary maximum compared to the FLAT case caused by increased turbulence in strong convective updrafts over the mountain ridges (cf. Wagner et al., 2014). Secondary maxima can also be observed in the turbulent-heat and moisture-flux profiles.

Compared to the FLAT case, the kinetic energy in the valley is contained not only in the large-scale flow and in the turbulent motions, but also in the local circulation (CKE). The distribution of the kinetic energy between turbulence and local circulation explains the lower TKE values in the cases with orography. The CKE (Fig. 3.5b) is

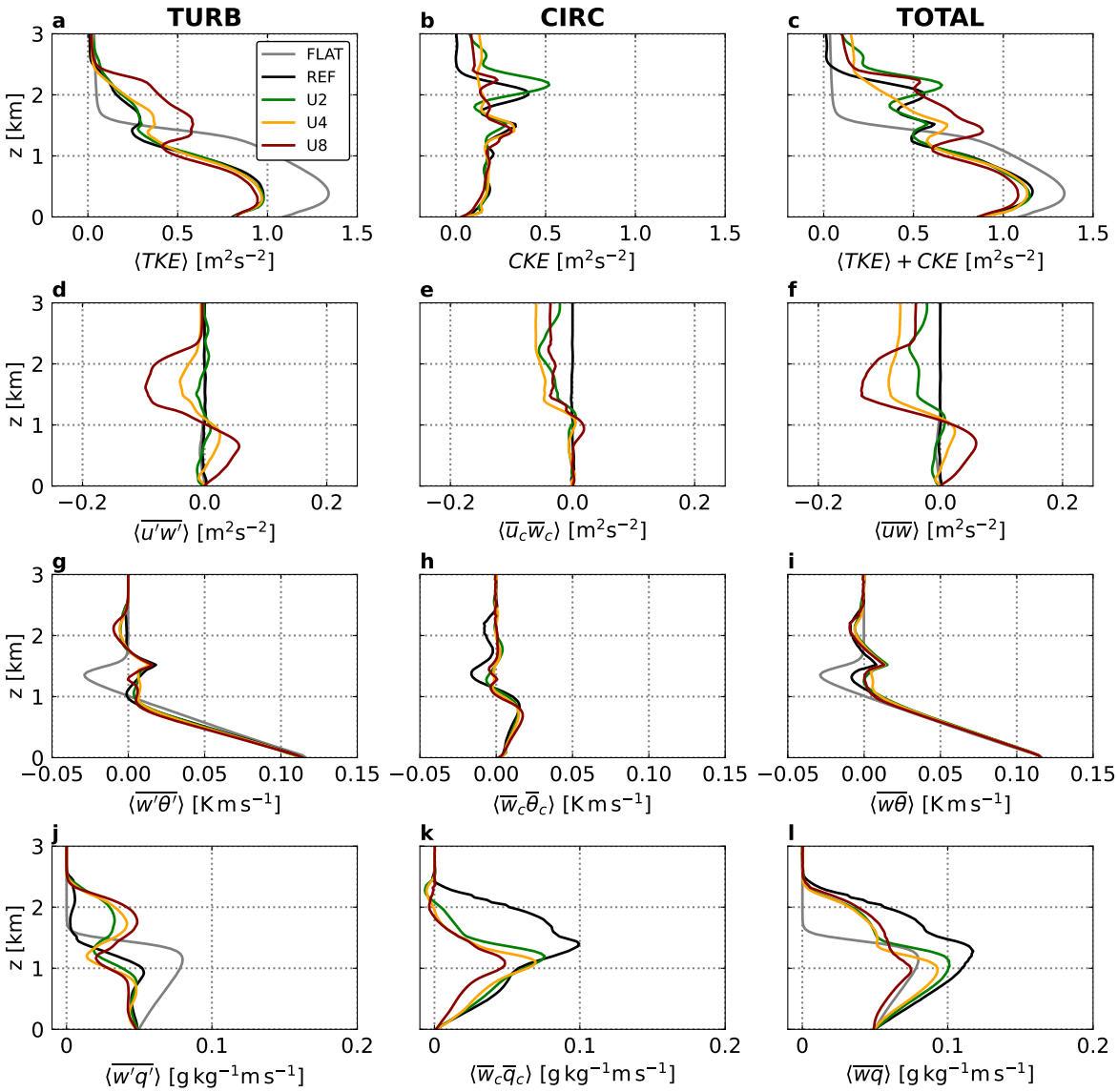

Figure 3.5: Area-mean profiles (height above valley floor) at 4 h of the turbulent components (left column), the local circulation components (center column) and their sum (right column) for (a)-(c) the kinetic energy, (d)-(f) the vertical momentum flux, (g)-(i) the sensible heat flux, and (j)-(l) the moisture flux. The turbulent part includes the subgrid contribution.

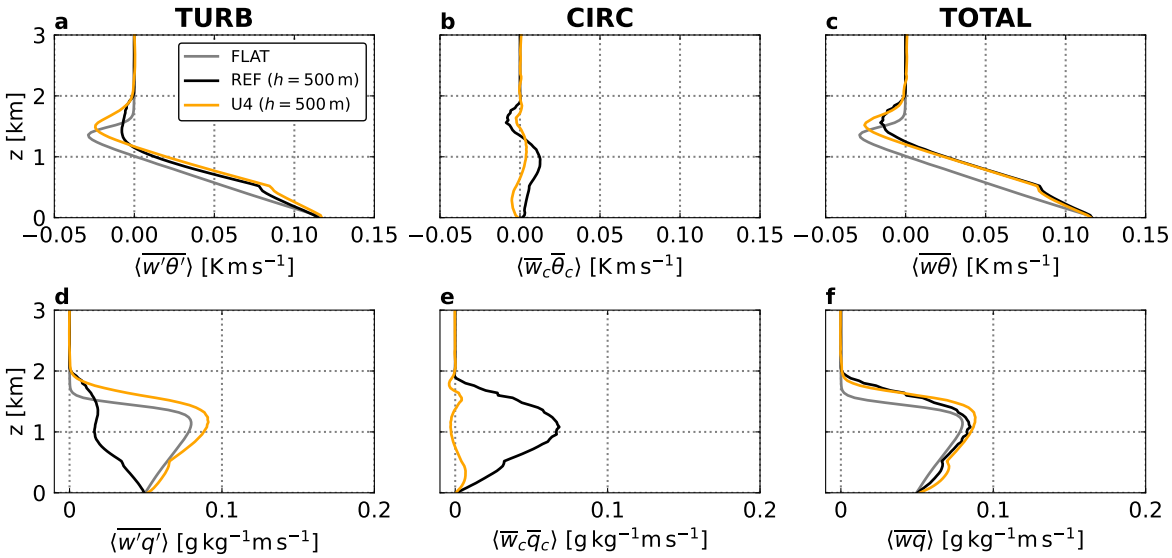

Figure 3.6: As in Fig. 3.5, but for the shallow-valley variants ($h = 500\,\mathrm{m}$) of the REF and the U4 case; without the kinetic-energy and vertical momentum-flux plots.

largest at altitudes where the circulation has mainly horizontal components. Thus, the two peaks in the CKE profile are related to the upper horizontal branches of the local circulation.

Shallow valley (500 m)

So far, we have only looked at the processes in a CBL over a deep valley where the ridge height is similar to or larger than the ABL height. However, shallow to moderately deep valleys can be expected to be even more frequent around the world. We repeat the REF and U4 simulations for a valley of only 500 m depth which is completely embedded in the ABL after a few hours of simulation. The result is shown in Fig. 3.4d-f and Fig. 3.6 after 4 h of simulation.

One can see in Fig. 3.4d-f that the heating and drying effect extends over the whole ML and is not limited to the valley atmosphere. Moistening occurs in a shallow zone above 1.5 km. Below crest height, the specific humidity decreases almost linearly down to the valley bottom. The profile of the turbulent sensible heat flux in Fig. 3.6a resembles that over flat terrain, but shows slightly higher values above the mountain tops. At 500 m, a second heat-flux maximum becomes evident. The circulation-induced heat flux in Fig. 3.6b is weak. All in all, the mean CBL structure over complex terrain with low ridge heights is qualitatively similar to that over flat terrain. Still, the impact of the valley-volume effect and the drying of the valley atmosphere by the thermal circulation is obvious even for shallow valleys.

3.4.4 Budget analysis

Budgets for heat and moisture

Next, we take a closer look at the heat and moisture budgets according to (3.15) and (3.16). Figure 3.7 shows valley cross sections of the local budget terms and Fig. 3.8 their horizontally averaged profiles, respectively. The contribution from the microphysics is zero, since cloud processes are negligible in our simulations at 4 h (not shown). For the FLAT case, Fig. 3.8 reveals homogeneous heating in the ML and cooling in the entrainment zone. At the same time, there is a slight drying of the ML, while the entrainment zone is strongly moistened. Over orography, the heating rates in the valley ML are approximately 1.5 times higher than in the FLAT case. Both from Fig. 3.7a-c and Fig. 3.8, it can be seen that the heating of the lower valley atmosphere is mainly caused by turbulence, while the slope winds mainly have a cooling effect. At higher levels, the air is recirculated to the center of the valley leading to a local warming. In contrast, Fig. 3.7g-i shows that the moisture is transported out of the lower part of the valley ($z \lesssim 0.5\,\mathrm{km}$) mainly by the slope winds to a height of 2 km where it accumulates and contributes to possible cloud formation over the ridges. The turbulent moistening in the entrainment zone and the drying effect of the subsiding air almost cancel out in the total tendency.

Budgets for TKE and turbulent fluxes

Next, the turbulence budgets are investigated, especially in terms of the impact of the local circulation on the turbulent processes. Budgets of TKE, $\langle\overline{w'\theta'}\rangle$, and $\langle\overline{w'q'}\rangle$ according to (3.17) and (3.18) are shown in Fig. 3.9 at 4 h. Only the resolved parts are presented because a subgrid contribution was not available for every single budget term. Tests with the TKE budgets have shown that the differences caused by the subgrid-scale terms are negligible above the surface layer (not shown). The net tendency of the budgets is close to zero almost everywhere, this means that the flow is close to a steady state.

Generally, the budgets for our FLAT case agree with the expectations from literature (e.g., Stull, 2012). For the TKE budget, the buoyancy and the dissipation term are the dominant source and sink terms. The turbulent transport term indicates an export of TKE out of the lower ABL to higher levels. For the turbulent fluxes of heat and moisture, the gradient production is non-zero due to significant vertical temperature and moisture gradients. Turbulent transport and molecular destruction are less important compared to the other terms. They reach their highest values near the surface and at inversion height.

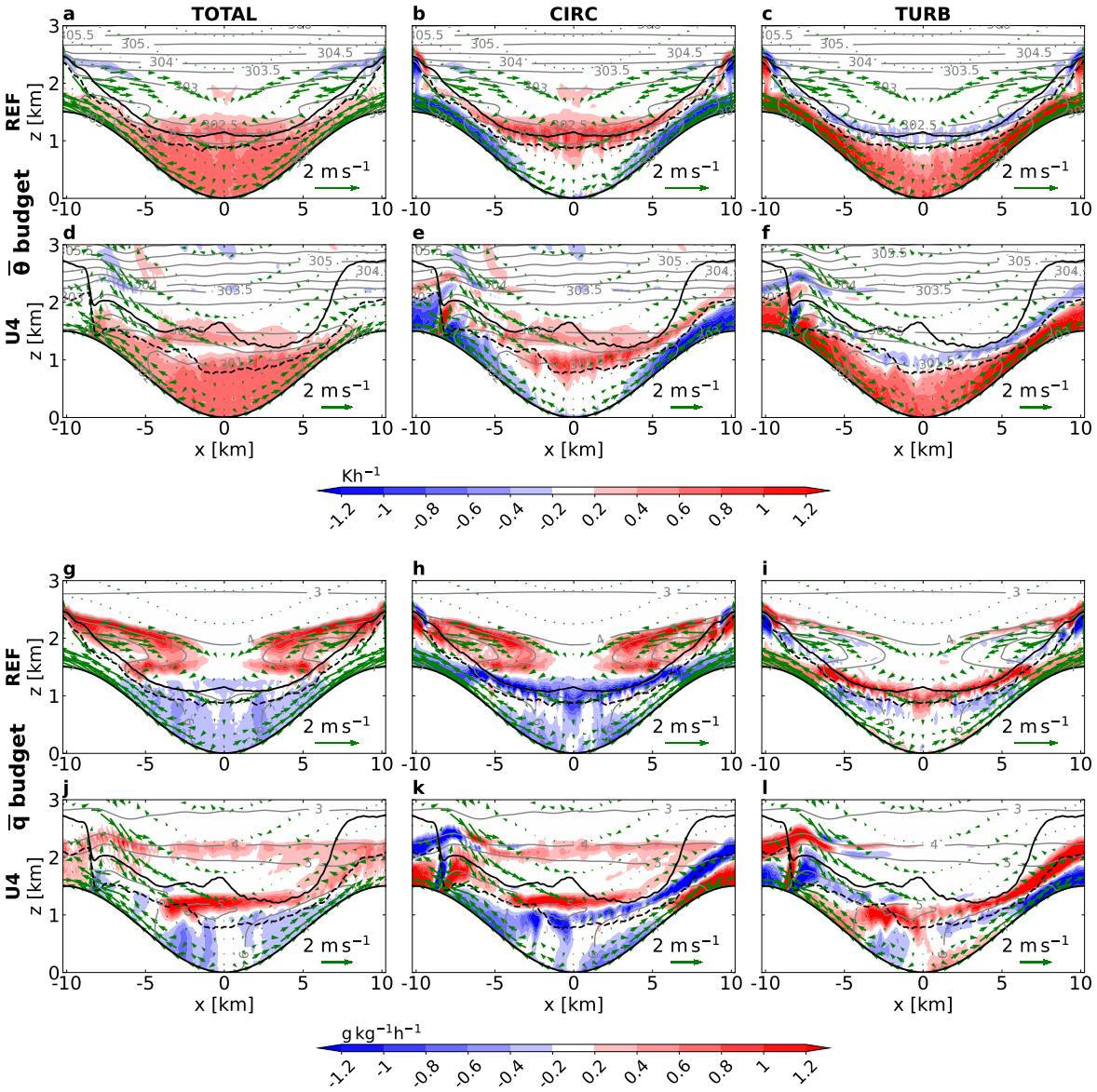

Figure 3.7: Valley cross sections as in Fig. 3.1, but showing the local budget terms for (a)-(f) heat and (g)-(l) moisture for REF and U4 at 4 h. The budgets terms include the total tendency (TOTAL), mean-flow advection (CIRC), and turbulence (TURB), corresponding to the terms in (3.15) and (3.16), respectively. The contribution from the microphysics (MP) is zero.

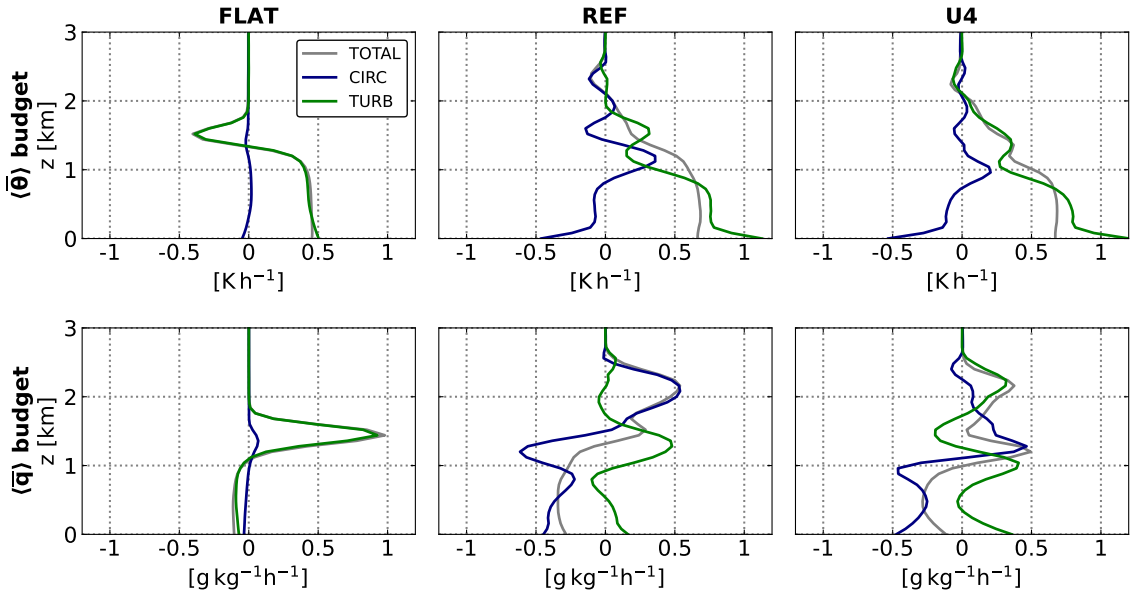

Figure 3.8: Vertical profiles of the heat and moisture budget for FLAT, REF, and U4 at 4 h ($h = 1500$ m). The budgets terms include turbulence (TURB) and mean-flow advection (CIRC) corresponding to the terms in (3.15) and (3.16) as well as the total tendency (TOTAL). The contribution from the microphysics (MP) is zero.

In the REF case, secondary maxima appear in the profiles of the buoyancy and the dissipation term in the TKE budget. In contrast to the FLAT case, the buoyancy term is positive throughout the ABL. The magnitude of the turbulent transport term is reduced compared to the FLAT case. Instead, the interaction term representing the advection and gradient production by the local circulation acts mainly as a consumption term inside the valley. This indicates that TKE is exported out of the valley by the slope winds resulting in generally lower TKE values inside the valley compared to the FLAT case.

For the turbulent fluxes, the interaction term is mainly positive and opposite to the gradient term, but they are not completely balanced. This means that the local circulation generally transports heat and moisture in the direction of the gradients. Turbulent transport is even less important than in the FLAT case. The turbulent sensible heat flux is essentially characterized by the balance between the buoyancy and the pressure term, the two dominant terms. For the turbulent moisture flux, the buoyancy and gradient terms are dominant, but the interaction term also reaches high values close to the surface and near the ridge height. The shapes of the curves are more complicated.

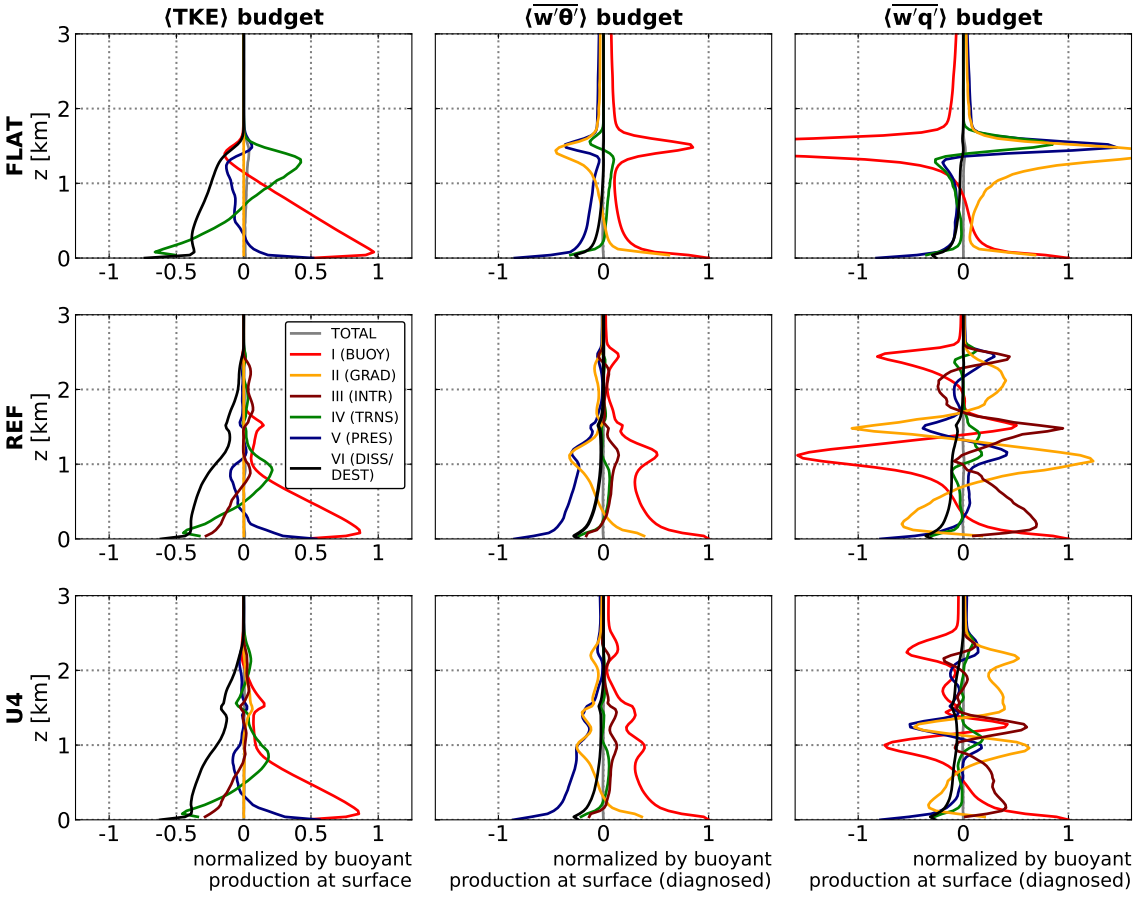

Figure 3.9: Vertical profiles of the area-mean budgets for TKE and the turbulent fluxes of heat and moisture according to (3.17) and (3.18) at 4 h for the three cases FLAT, REF, and U4. Note that subgrid contributions are not included.

3.5 Impact of an upper-level wind

3.5.1 Flow structure and gravity waves

In the following, we investigate the impact of an upper-level wind on the flow structure, the exchange processes, and the temperature and moisture distribution. The structure of the local flow is displayed for the reference case and two cases with an upper-level wind in Fig. 3.10. Two vertically stacked circulation cells can be found over each slope in the REF case. This structure is modified in the U2 and U4 cases by gravity waves which form distinct wave patterns over the valley. It is remarkable that gravity waves are generated even though the initial wind profile was chosen to avoid orographic waves. This means that the waves emerge from the deflection of the large-scale wind by the local circulation as a sort of convectively generated gravity waves (Clark et al., 1986). Thus, although not directly of orographic origin, the resulting wave pattern shows typical characteristics of a stationary mountain wave. As expected for mountain waves, the vertical wave length increases with the large-scale wind velocity.

Regarding the area-mean profiles in Fig. 3.4a, the large-scale wind profile $\langle\overline{u}\rangle$ is clearly influenced by the local processes in and above the valley. Below about 2 km, the wind speed has decelerated in the U4 and U8 case. In addition, $\langle\overline{u}\rangle$ is even negative at a height around 1 km due to the deformation of the cross-valley circulation by the large-scale wind. The profile of the turbulent vertical momentum flux $\langle\overline{u'w'}\rangle$ explains the deceleration, showing that momentum from around 1.5 km is transported into the valley via the turbulence. Turbulent mixing dominates the vertical momentum transport between the valley and the free atmosphere, while the circulation momentum flux $\langle\overline{u}_c\overline{w}_c\rangle$ is non-zero mainly in the free atmosphere. However, this is caused by gravity waves which are accounted for as local circulation, as they have the same spatial scales as the thermal circulation. For U8, that gravity waves' momentum flux is smaller than for U2 and U4 at 4 h, but exceeds them at later times (not shown). The lower vertical group speed of the gravity waves for higher ambient wind speeds could be the cause for this effect. The deceleration of the large-scale flow can also be observed over the shallow valley (Fig. 3.4d).

The CKE profiles in Fig. 3.5b are oscillating with height due to the occurrence of gravity waves, especially above crest height. Although the local circulation is modified in structure, Fig. 3.10 shows that the circulation wind velocities are not generally reduced by the upper-level wind. Thus, the impact of the upper-level wind on the vertical heat and mass transport can not be explained by a generally weaker thermal circulation.

Looking at the budgets for the second-order moments in Fig. 3.9, we find that the

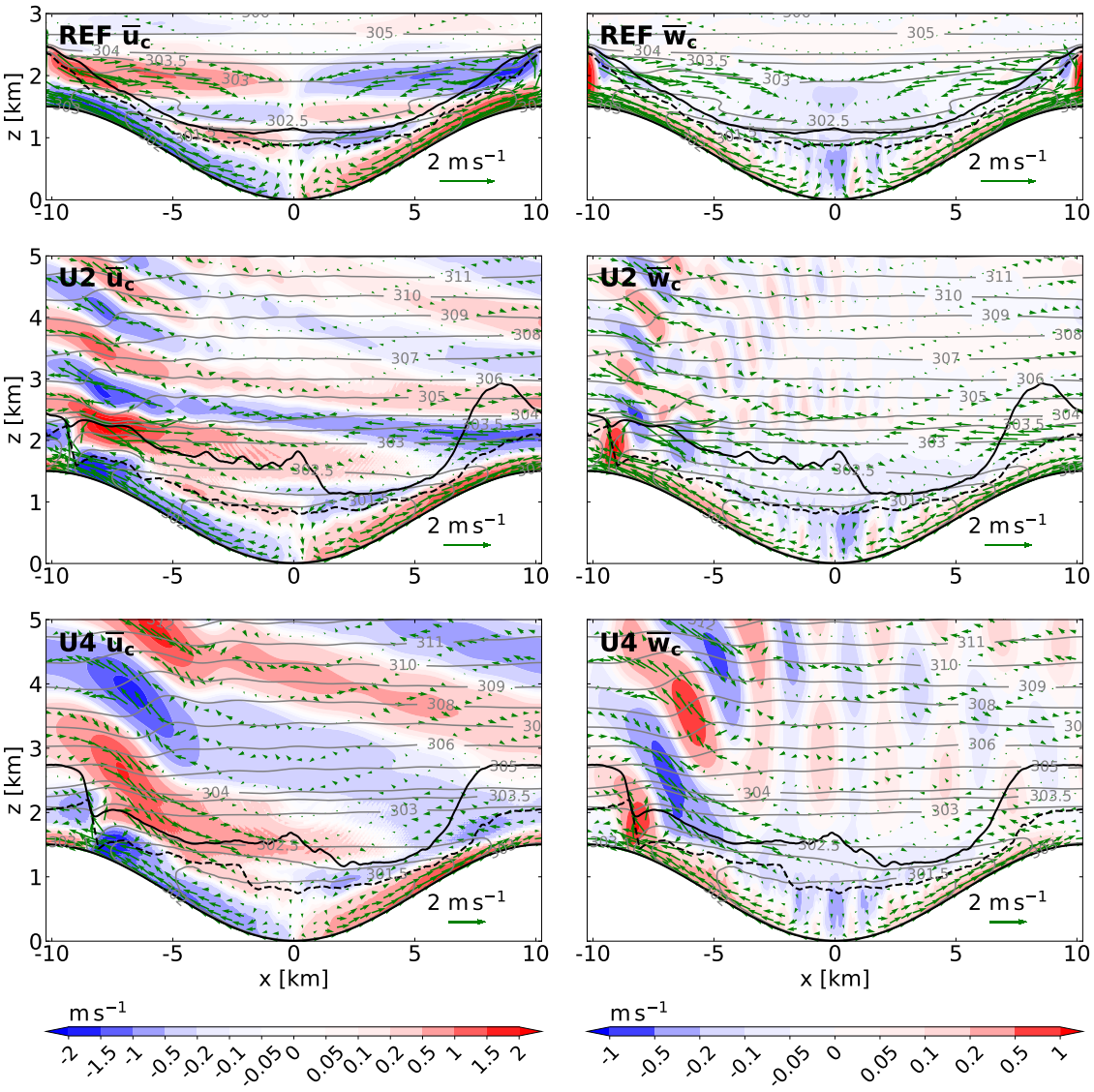

Figure 3.10: Valley cross sections showing the local circulation wind vectors as well as the zonal and vertical parts of the cross-valley circulation ($\overline{u}_c$ and $\overline{w}_c$, shading) at 4 h for REF, U2, and U4. Also showing the isolines of the potential temperature in K. The dashed line marks the diagnosed ML height and the solid line the diagnosed ABL height.

upper-level wind does not strongly change the character of the TKE budget. The gradient production by the large-scale flow contributes only little to the TKE budget.

3.5.2 Impact on temperature and moisture distribution

It is remarkable that the upper-level wind has only a minor influence on the $\langle\overline{\theta}\rangle$ profile (Fig. 3.4b and e). Although the local circulation is modified by the large-scale flow, the temperature distribution is largely unaffected by this change. In contrast, there is a significant impact of the upper-level wind on the area-mean profile of the specific humidity $\langle\overline{q}\rangle$. For stronger winds, less moisture seems to be exported out of the valley. The $\langle\overline{q}\rangle$ values near the valley bottom are slightly higher which is most obvious for U8. The cross sections in Fig. 3.1d-f reveal that the large moisture accumulations above the ridges disappear for the U4 case and the moisture distribution becomes more horizontally uniform, at least above crest level. The turbulent heat flux does not change strongly, while the turbulent moisture flux becomes asymmetric with respect to the valley center and reaches higher values around crest level compared to the REF case.

Correspondingly, the profiles for the sensible heat flux in Fig. 3.5g-i do not change strongly for different upper-level wind velocities, especially within the valley. In fact, the change in the total sensible heat flux is only visible around a height of 1.5 km. The circulation part of the heat flux $\langle\overline{w}_c\overline{\theta}_c\rangle$ shows slightly stronger deviations from the REF case, especially in its upper parts. However, due to its smaller magnitude, it has only a small impact on the resulting temperature profile. In contrast, the vertical moisture flux is very sensitive to the upper-level wind (Fig. 3.5j-l). For U8, the peak in $\langle\overline{w}_c\overline{q}_c\rangle$ is diminished almost to half of its REF value. Also the profile of the turbulent component is strongly altered. While $\langle\overline{w}_c\overline{q}_c\rangle$ plays the dominant role in the REF case, both parts attain similar importance for stronger background winds.

For the shallow valley, the impact of the upper-level wind on the mean humidity profile is limited to a reduced drying of the valley atmosphere (Fig. 3.4f). However, the turbulent and the circulation part of the moisture flux are almost interchanged between REF and U4 (Fig. 3.6d-f). Regardless, the total moisture flux remains relatively unchanged.

The relatively small impact of the upper-level wind on the heat transport can also be seen in the budgets (Fig. 3.7a-f) where the differences between REF and U4 are rather small. Also the total heating rate in the profiles of Fig. 3.8 remains almost unchanged. In contrast, the moisture tendencies in Fig. 3.7g-l change very distinctively with the upper-level wind. With a horizontally more uniform moisture distribution, the local circulation leads to positive moisture tendencies in the slope-wind layer around

crest height and negative tendencies above. Although the turbulent exchange counteracts the circulation tendencies, the total amount of exported moisture is significantly reduced, at least in case of the deep valley. This is also seen in Fig. 3.8 where there is no longer a negative peak between 1 and 1.5 km in the circulation term for moisture. The circulation term even becomes positive there. As a result, also the total moisture tendency in the upper part of the valley between 1 and 1.5 km is now positive. Compared to the REF case, the positive peak above 2 km is now mainly caused by turbulent transport. It is, however, significantly smaller.

For the second-order moments (Fig. 3.9), the biggest differences between REF and U4 are, as expected, in the moisture-flux budget, specifically at crest height where the gradient production becomes positive. Generally, the buoyancy and the gradient production term turn out to be smaller than in the REF case.

In summary, an upper-level wind affects mostly the vertical moisture transport, while the resulting temperature profile remains almost unchanged. In this setup, this is facilitated by the initial humidity profile decreasing with height. Moisture export out of the valley is mostly achieved by the upslope winds and the stationary updrafts above the ridge tops. The turbulent moisture flux leads to a moistening of the slope-wind layer below crest height. Consequently, the slope-wind layer remains rather moist compared to the relatively dry valley core. A horizontal upper-level wind changes the transport patterns by making the moisture distribution more horizontally uniform. In the end, this reduces the moisture export out of the valley. In contrast, the thermal circulation acts to weaken horizontal temperature gradients. The resulting, horizontally more homogeneous temperature distribution is much less affected by an upper-level wind.

3.6 Bulk heat and mass transport

In order to compare the impact of the upper-level wind on the vertical exchange of heat and mass with other factors, more simulations were performed. Specifically, sensitivity studies were conducted for the initial temperature lapse rate γ and the valley width W. The present comparison focuses on the total sensible heat and moisture fluxes out of the valley atmosphere, that is the time-integrated total flux across a horizontal surface at $z = 1.5\,\mathrm{km}$. The fluxes, normalized by the total time-integrated surface fluxes, are shown in Fig. 3.11. The intention is to depict the vertical net flux out of the valley (ratio of export). However, the accumulated fluxes are also influenced by a small amount of direct heating by the surface fluxes at the ridge tops. Generally, there is a much smaller net export of heat than of moisture. While the upslope winds have a local cooling effect and the valley is heated quite homogeneously, the moisture

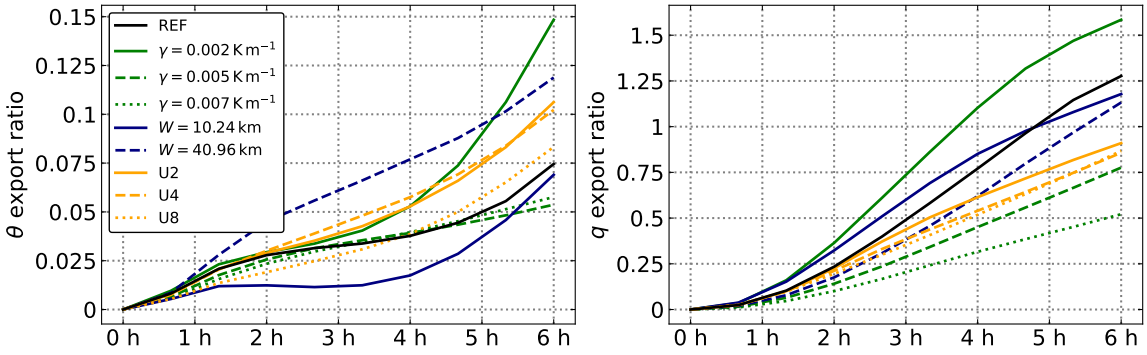

Figure 3.11: Time series of the time-integrated total sensible heat and moisture flux at crest height (1500 m, sum of turbulent and local-circulation part) normalized by the total time-integrated surface fluxes for the different cases where either the initial lapse rate γ (green), the valley width W (blue), or the upper-level wind (orange) was varied.

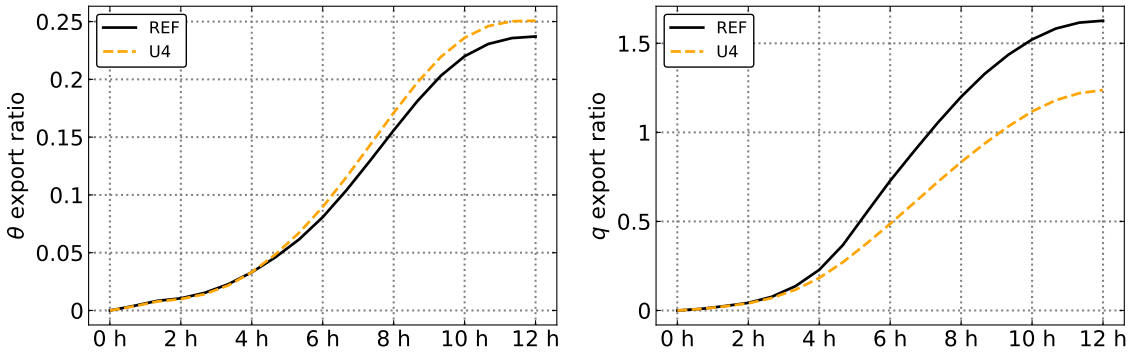

Figure 3.12: As in Fig. 3.11, but during a diurnal-cycle induced by a homogeneous radiative forcing.

is exported out of the valley by the slope-wind circulation. After 6 hours, the fraction of moisture exported is $50 - 150\%$, while for heat the fraction is only $5 - 15\%$.

For both the heat and the moisture flux, the background stratification seems to have the strongest impact, especially when the initial lapse rate is below the value of the REF simulation ($0.003\,\mathrm{K\,m^{-1}}$). Even a slight reduction to $0.002\,\mathrm{K\,m^{-1}}$ leads to the onset of cloud formation at 4 h and a considerable increase of the heat export related to an early break-up of the valley inversion (Leukauf et al., 2016). In contrast, when the initial lapse rate is larger than the REF value, there is almost no decrease of the heat export ratio before 5 h. For the moisture export, the effect of a weaker stratification is similar, while a stronger stratification results in a significant decrease of the export ratio.

As varying only the valley width does not affect the area-height distribution of the terrain, the valley atmosphere receives the same heat input per surface area. Thus, the heating of the valley should not be affected. However, wider valleys seem to facilitate the sensible-heat export, especially after the first hours of simulation. The result for moisture is contrary to that for sensible heat, although there seems to be a compensating effect at the end of the simulation. Here, it is difficult to go into more detail without more simulations and longer integration times.

In comparison to a variation of the background stratification, the upper-level wind has a smaller impact. Nevertheless, even a weak wind of $2\,\mathrm{m\,s^{-1}}$ leads to a 30% reduction in total moisture export. The export of sensible heat seems to be enhanced at least for the cases U2 and U4, questioning the nearly unmodified $\langle\overline{\theta}\rangle$ profiles (Fig. 3.4b). However, this observation, as well as the effect of varying the valley width, is put into perspective by the generally small magnitude of the heat export ratio. It has only a slight impact on the temperature profile.

Finally, the results concerning the upper-level wind are validated in a more realistic simulation forced by the diurnal cycle of solar radiation. The results for the accumulated fluxes at crest height shown in Fig. 3.12 agree with the above findings: An upper-level wind can lead to a significant reduction of the total moisture export, while the heat transport from valleys to the free atmosphere is less affected.

3.7 Conclusion

In this study, the impact of a large-scale upper-level wind on the daytime vertical heat and mass transfer over mountainous terrain was investigated using idealized large-eddy simulations. A key feature of this work is the decomposition of the flow into a small-scale turbulent part, a local mean circulation, and a large-scale background flow

as well as the distinction between turbulent and advective transport by means of heat and moisture budget analysis. The test cases include simulations over a periodic, quasi-two-dimensional valley of different heights and widths and with different upper-level wind velocities. The major findings are summarized as follows:

- The thermally driven upslope winds and the horizontal and subsiding recirculation form a mean cross-valley circulation which can be clearly separated from small-scale turbulence and large-scale flow. Its main effect is to export moisture out of the valley through the slope-wind layer and to accumulate it over the mountain tops. This builds up a horizontal moisture gradient between the slopes and the valley center. In contrast, the temperature distribution is more or less horizontally homogeneous, as the local circulation is directly driven by temperature gradients and acts to reduce them. The temperature distribution is characterized by enhanced heating rates inside the valley due to the valley-volume effect. Heating by the mean circulation is mainly located in the elevated branch of the circulation.

- From a horizontally averaged perspective, moisture is mainly transported by the slope flows and turbulent exchange plays a minor role for the vertical transfer of moisture. In contrast, turbulent mixing is the dominant process for the heating of the mixed layer. The thermal circulation is mainly balancing horizontal temperature gradients and contributes less to vertical heat exchange. A comparison of the turbulent-flux budgets between a flat and a mountainous-terrain boundary layer shows that the gradient-production terms are reduced because of additional advection terms arising due to the thermal circulation. In case of the turbulent kinetic energy budget, these additional terms act as a sink of TKE in the lower parts of the valley.

- An upper-level wind has a minor impact on the temperature profile, as the temperature distribution is already fairly horizontally homogeneous. The additional shear generated by the large-scale flow does not significantly increase turbulent mixing, at least in the current setup. Instead, it strongly affects the moisture distribution with its strong horizontal gradient between the rather dry valley center and the moister slope region. In consequence, an upper-level wind leads to a reduced vertical transfer of moisture even though the strength of the slope flow is not significantly diminished. Thus, it can strongly reduce the export of moisture out of a valley and into the free atmosphere. Similar results were found in a more realistic setup with variable surface fluxes determined by an interactive land-surface model driven by solar radiation.

In summary, this study contributes to an improved process understanding of heat and mass exchange over mountainous terrain. The situation is quite different from the widely described flat convective boundary layer where heat and mass are mainly transported by turbulent motions. Over mountainous terrain, thermally-induced winds interact with turbulence and the large-scale flow. This situation was studied by comparing the evolution and distribution of temperature and moisture under the influence of an upper-level wind. The strong impact of the upper-level wind on the vertical mass transport can be an important factor for cloud formation and tracer dispersion over mountains. The results may not only be relevant for a better insight into the physical processes, but also for future parameterization development. Although the simulations are fairly idealized, we expect that the main findings are relevant also in more complex situations.

It is clear that it would be more difficult to apply this analysis over a more complex three-dimensional orography. Without a symmetry axis of the terrain, the ensemble mean would have to be calculated either by temporal averaging only or by temporal averaging combined with box- or section-wise spatial averaging only over parts of the valley. It has to be kept in mind that other symmetry effects, like the disappearing turbulent momentum flux in the cross-valley average, will not arise with a more realistic orography. Furthermore, along-valley winds occurring in three-dimensional terrain would interact with the slope-wind circulation. Another factor would be cloud formation over the ridges which may result in precipitation. That would change the heat and moisture balance between the valley and the free atmosphere significantly. Additionally, three-dimensional radiative effects, like the shading of a valley by a ridge or a mountain peak and different land surface characteristics, would also have to be considered. The investigation of these more complex aspects of thermally driven flows over mountainous terrain is left for future research.

Acknowledgments

This research was funded by Hans Ertel Centre for Weather Research of DWD (3rd phase, The Atmospheric Boundary Layer in Numerical Weather Prediction), grant number 4818DWDP4. We thank the anonymous reviewers for their valuable suggestions which improved the manuscript considerably.

Chapter 4

Boundary-layer plumes over mountainous terrain in idealized large-eddy simulations

Jan Weinkaemmerer[1,2], Matthias Göbel[3,4], Stefano Serafin[5], Ivan Bašták Ďurán[6], Jürg Schmidli[1,2]

1 – Institute for Atmospheric and Environmental Sciences, Goethe University Frankfurt, Frankfurt/Main, Germany

2 – Hans Ertel Centre for Weather Research, Offenbach, Germany

3 – Department of Atmospheric and Cryospheric Sciences, University of Innsbruck, Innsbruck, Austria

4 – Regional Office Salzburg and Upper Austria, GeoSphere Austria, Salzburg, Austria

5 – Department of Meteorology and Geophysics, University of Vienna, Vienna, Austria

6 – European Centre for Medium-Range Weather Forecasts, Bonn, Germany

Abstract

Coherent plume structures in the convective boundary layer over non-flat terrain are investigated using large-eddy simulation. A conditional sampling method based on the concentration of a decaying passive tracer is implemented in order to identify the

boundary-layer plumes objectively. Conditional sampling allows to quantify the contribution of plume structures to the vertical transport of heat and moisture. A first set of simulations analyses the flow over an idealized valley, where the terrain elevation only varies along one horizontal coordinate axis. In this case, vertical transport by coherent structures is the dominant contribution to the turbulent components of both heat and moisture flux. It is comparable in magnitude to the advective transport by the mean slope-wind circulation, although it is more important for heat than for moisture transport. A second set of simulations considers flow over terrain with a complex texture, drawn from an actual digital elevation model. In this case, conditional sampling is carried out by using a simple domain-decomposition approach. We demonstrate that thermal updrafts are generally more frequent on hill tops than over the surroundings, but they are less persistent on the windward sides when large-scale winds are present in the free atmosphere. Large-scale, upper-level winds tend to reduce the vertical moisture transport by the slope winds.

4.1 Introduction

Updrafts of positively buoyant air known as thermals or plumes have been studied as a key component of the convective boundary layer (CBL) for several decades (Turner, 1962; Simpson and Wiggert, 1969). Such coherent turbulent structures have been shown to transport a major part of the heat and moisture between the surface and the free atmosphere. In numerical weather prediction and climate models, the advective and turbulent fluxes due to these flow structures are not explicitly resolved and need to be parameterized. Thereby, the interest in coherent convective structures was often driven from a cloud physics point of view (Simpson and Wiggert, 1969; Nicholls, 1989). Generally, in parameterizations of the convective boundary layer for weather and climate models, the traditional eddy-diffusivity formulation is only able to model local turbulent fluxes (Siebesma and Cuijpers, 1995). The properties of convective updrafts in the daytime boundary layer are often poorly correlated with local gradients, hence they need to be parameterized using non-local turbulence closures (Randall et al., 1992). To this end, the eddy-diffusivity approach can be combined with a mass-flux term to the so-called eddy-diffusivity mass-flux scheme providing a better physical basis for parameterizations (Siebesma et al., 2007; Angevine et al., 2010).

Unlike Numerical Weather Prediction models, Large Eddy Simulation (LES) can be used to explicitly resolve small-scale coherent motions down to the meter scale. They have been widely used to study both clear and cloudy boundary layers, often with the goal to improve parameterizations (Schumann and Moeng, 1991; Heus and Jonker,

2008). Statistics of LES output can reveal how the total turbulent flux is partitioned between local (diffusive) and non-local (related to coherent structures) components, provided that a method for the accurate identification of coherent structures is available (Raupach, 1981). Several updraft sampling methods relying on vertical velocity and thermodynamic variables have been introduced and applied in dry convective boundary-layer cases (Williams and Hacker, 1992; Berg and Stull, 2004). Due to the limitations of such approaches in the transition between sub-cloud and cloud layer, sampling methods based on passive tracers were introduced, with the aim to evaluate the entrainment and detrainment rates into the plumes from the surface to the top of the cumulus clouds (Couvreux et al., 2010). Other publications point out the importance of taking into account downdraft structures as well, e.g., in stratocumulus-topped marine cases (Brient et al., 2019). It has also been shown that coherent convective structures in simulation data can be analyzed with the help of joint probability density functions (PDFs, Chinita et al., 2018). The joint PDFs of the vertical velocity with temperature and humidity perturbations have often been used to study and to parameterize dry and especially moist convection (Wyngaard and Moeng, 1992; Larson and Golaz, 2005). Non-local, coherent turbulent fluctuations manifest in the non-Gaussian part of the joint PDF.

Most existing studies about boundary-layer plumes are limited to flat terrain. Over complex orography, the tendencies for heat and moisture and thus the boundary-layer height turn out to be horizontally inhomogeneous and the transport processes extend over a range of scales (Lehner and Rotach, 2018). The reconstruction of transport processes in a valley is possible after a spatial and temporal filtering of the flow allowing a decomposition into a large-scale wind, a local mean circulation, and a small-scale turbulent part. This approach has led to numerous insights related to the advective transport by local thermal wind systems such as slope and valley winds, in particular during daytime. In case of the slope-wind circulation, a buoyancy-driven upslope flow arises over the heated valley slope (Vergeiner and Dreiseitl, 1987). A subsiding branch running from the ridge top back to the valley center closes the circulation cell. Budget analyses show that the slope-wind circulation has a cooling effect over the slopes while it leads to local heating in the valley center (Schmidli, 2013). Together with the turbulent heat flux, this results in a rather homogeneous heating of the valley atmosphere. Moisture, approximated as a passive scalar quantity, is efficiently exported out of the valley by the slope winds and accumulated over the ridges (Kuwagata and Kimura, 1997; Weinkaemmerer et al., 2022a). In consequence, it is found that a large-scale, horizontal wind effectively reduces the export of moisture out of the valley by mixing dry air from above the valley center into the moist slope-wind layer. In contrast,

the temperature distribution remains nearly unaffected. Unlike a horizontally homogeneous CBL, where buoyant plumes are randomly distributed and feature a broad spectrum of scales (Griewank et al., 2022), the CBL over orography can be expected to show particularly intense plumes over the hilltops which constitute natural regions of horizontal convergence at daytime. Also, their spatial scales may be controlled by the properties of the underlying orography (Göbel et al., 2023). Several studies focus on the vertical transport induced by stationary updrafts over mountain crests, primarily because they are the most likely to evolve into precipitating moist convection (Demko and Geerts, 2010a,b; Nelson et al., 2022; Göbel et al., 2023). Due to an upper-level wind, they can be shifted horizontally (Panosetti et al., 2016). Aside from the hilltop updrafts, it is not yet clear how the boundary-layer plumes behave in the slope-wind layer and how the turbulent fluxes are partitioned between coherent-motion transport and unorganized turbulence at different locations along the valley cross section.

In this paper, we want to address these unclarities by studying boundary-layer plumes over idealized and semi-idealized complex orography. For this purpose, we run LES at about 40 m resolution and implement a conditional sampling method that relies on a transported passive tracer. Following Weinkaemmerer et al. (2022a), basic experiments are performed over a quasi-two-dimensional, periodic valley where the surface fluxes are prescribed and constant. This idealized-valley case simplifies the updraft sampling and the decomposition of the flow. The goal is to identify and characterize boundary-layer plumes over smooth complex terrain, to study the horizontal distribution of the turbulent flux contributions, and to gain insight into the structure of the slope-wind layer. Furthermore, the turbulence statistics in relation to the local mean circulation are evaluated by calculating the joint PDFs on different height levels. This is followed by two simulations over three-dimensional orography with a radiation-driven diurnal cycle. Thereby, a simple approach towards structure identification and flow decomposition over more realistic terrain is tested. With that, the effect of an upper-level wind on the coherent structures and on the bulk quantities is analyzed.

The paper is structured as follows: In the next section, the experimental setup and the numerical model is presented. The analysis methods with the conditional sampling and the flow decomposition are introduced in section 4.3. In section 4.4 to 4.5, the results of the simulations are discussed. Conclusions are given in section 4.6.

4.2 Numerical model simulations

4.2.1 Experimental setup

The idealized-valley case is set up as in Weinkaemmerer et al. (2022a). The orography is a periodic, infinitely long sinusoidal valley described by:

$$z_s(x) = \frac{h}{2}\left(1 - \cos\frac{2\pi x}{W}\right), \text{ for } -\frac{L_x}{2} < x < \frac{L_x}{2}, \tag{4.1}$$

where z_s is the surface height, $h = 1500\,\mathrm{m}$ the ridge height from valley floor to crest, and $W = 20.48\,\mathrm{km}$ the width of the valley from ridge to ridge which also equals the domain width L_x. The domain length L_y is 40.96 km. In the reference experiment (REF), the background atmosphere is at rest. The initial atmosphere is in hydrostatic balance with $p = 1000\,\mathrm{hPa}$ and $\theta = 297\,\mathrm{K}$ at $z = 0$, a linear potential-temperature increase with height of $\Gamma = 0.003\,\mathrm{K\,m^{-1}}$, and a constant relative humidity of 40 %. The surface sensible heat and moisture fluxes are prescribed as $(\overline{w'\theta'})_s = 0.12\,\mathrm{K\,m\,s^{-1}}$ and $(\overline{w'q'})_s = 0.05\,\mathrm{g\,kg^{-1}\,m\,s^{-1}}$ (corresponding to a Bowen ratio ≈ 1), and the roughness length is set to $z_0 = 0.16\,\mathrm{m}$. The total duration of the simulation is 6 h. An additional simulation is carried out over a flat surface (FLAT) with the same setup as it is used over the valley.

For the three-dimensional cases, the terrain is loosely derived from the area around the Chabre mountain near Laragne-Monteglin in Southern France standing exemplarily for a hilly terrain. The smoothed orography is damped towards a constant height at the lateral boundaries of the domain, where periodic boundary conditions are imposed. The dimensions of the domain are $L_x = 34.9\,\mathrm{km}$ and $L_y = 32.3\,\mathrm{km}$. The total duration of these simulations is 12 h. The initial sounding corresponds to 11 July 2003, 06 UTC, a summer day featuring a clear CBL. For the three-dimensional reference case (REF3D), the winds are set to zero. For the WIND3D case, the full initial sounding is adopted including zonal and meridional wind. The time and the location determine the surface fluxes given by a surface-layer model in combination with a radiation scheme.

4.2.2 Numerical model

The numerical simulations are performed with the CM1 model (Cloud Model 1, Bryan and Fritsch, 2002) in LES mode. It uses terrain-following σ_z coordinates. The model is integrated using third-order Runge-Kutta time differencing (Wicker and Skamarock, 2002) and a fifth-order WENO scheme both for the advection of scalars and momentum (Jiang and Shu, 1996). The Coriolis force is neglected. The horizontal resolution is

40 m (42 m for the three-dimensional cases). Grid stretching is applied in the vertical, reaching from 8 m vertical resolution at the surface to 40 m at a height of 2800 m and above. The model top at 5000 m is a rigid lid. This corresponds to 175 vertical levels. For the WIND3D case, the model top is raised to 8000 m (250 vertical levels) because of vertical gravity-wave propagation. In order to suppress spurious wave reflections, a sponge layer with Rayleigh damping is employed ($\tau = 300\,\mathrm{s}$). Its depth is 1000 m (2000 m for WIND3D). In order to facilitate the onset of convective turbulence, the initial atmosphere is altered by a random temperature perturbation with a maximum amplitude of 0.5 K. The model uses an adaptive time step with a typical value of 2 s. For subgrid-scale turbulence closure, a 1.5-order TKE scheme is chosen (Deardorff, 1980). Microphysical processes are parameterized using the Morrison double-moment scheme (Morrison et al., 2009). Atmospheric radiation is parameterized by the Goddard scheme (Chou and Suarez, 1999). For the surface-layer model (revised MM5 scheme, Jiménez et al., 2012), the grassland option is selected.

4.3 Analysis methods

4.3.1 Conditional sampling

The conditional sampling method has been implemented according to Couvreux et al. (2010). It uses a passive tracer emitted at the surface with a constant surface flux. The value of the surface flux is arbitrary. The tracer concentration decays exponentially with a time scale of $\tau_0 = 15\,\mathrm{min}$ to ensure that the tracer does not accumulate outside the updrafts above the surface. A grid point is characterized as belonging to a coherent structure if the local vertical velocity w is positive and the tracer concentration anomaly c' exceeds the standard deviation of the tracer concentration σ_c and a minimum threshold σ_{min}:

- $w > 0$,
- $c' > \max(\sigma_c, \sigma_{\mathrm{min}})$.

In Couvreux et al. (2010), c' is defined as the deviation from the domain average of the tracer concentration. This is only meaningful in a horizontally homogeneous setup, i.e. over flat terrain. In this study, for the idealized periodic valley, the spatial average is computed along the y axis of the domain, i.e. the symmetry axis of the terrain. Sensitivity tests have shown that a number of grid points of ≈ 1000 is sufficient for the spatial average to converge. With that, the conditional sampling is applied every 1 min of the simulation. The minimum threshold is defined as $\sigma_{\mathrm{min}} = (0.05/z) \int_0^z \sigma_c(z')\,\mathrm{d}z'$ so

that no point is selected in a non-turbulent environment. The effect of an additional condition, ensuring that only cloudy grid points are selected within the cloud layer, is negligible in this study as only sparse cumulus clouds are formed in the REF case after 4 h simulation time.

Over three-dimensional orography, the computation of a spatial average is not straightforward without a symmetry axis of the terrain. Thus, the domain needs to be divided into multiple subdomains. The spatial (horizontal) averaging is performed on the σ coordinate surfaces, over non-overlapping subdomains of the size $1.3\,\mathrm{km} \times 1.3\,\mathrm{km}$. This approach is a compromise between the competing needs of obtaining robust statistics of coherent structures (requiring large subdomains) and considering areas of relatively homogeneous orography (requiring small subdomains). It ensures that the averaging still extends over 1024 grid points. Each square subdomain can be considered as representative of a grid-element of an operational-scale numerical weather prediction model.

4.3.2 Flow decomposition

By means of spatial and temporal averaging, the flow is decomposed as shown in Weinkaemmerer et al. (2022a). With the aim to compute the turbulent fluxes, the turbulent fluctuation a' of a flow variable a is separated from the ensemble average $\overline{a}$ via Reynolds decomposition:

$$a = \overline{a} + a'. \tag{4.2}$$

Subgrid-scale fluctuations not resolved in the LES are treated as being included in the turbulent part. Following the Reynolds averaging rules, the ensemble average of a product is given by:

$$\overline{ab} = \overline{(\overline{a} + a')(\overline{b} + b')} = \overline{a}\overline{b} + \overline{a'b'}. \tag{4.3}$$

The second-order turbulent fluxes consist of a resolved and subgrid part:

$$\overline{a'b'} = \overline{a'b'}|_{res} + \overline{a'b'}|_{sgs}. \tag{4.4}$$

For the analysis, the subgrid parts are obtained from the LES subgrid turbulence model.

In order to study the thermally induced flow, the quantity's horizontal average over the whole domain $\langle\overline{a}\rangle$ can be removed from the ensemble average leaving a local average $\overline{a}_c$ describing the mean circulation:

$$\overline{a}_c = \overline{a} - \langle\overline{a}\rangle. \tag{4.5}$$

Over the sinusoidal valley, the required ensemble average is approximated by an average

in time and in the along-valley direction:

$$\overline{a}(x,z,t) = \frac{1}{TL_y}\int_{t-T}^{t}\int_{0}^{L_y} a(x,y,z,t')\,\mathrm{d}y\,\mathrm{d}t'\,, \tag{4.6}$$

where x, y, and z is the eastward, northward, and vertical direction, respectively; and t is time. Here, z denotes the absolute height above sea level. The time averaging is based on 1 min intervals. It is done online during the model run in order to reduce the data output. Each averaging period T extends over 40 min as a compromise between accuracy and stationarity (Schmidli, 2013). The domain mean is then achieved by averaging $\overline{a}$ additionally in x direction on constant height levels:

$$\langle\overline{a}\rangle(z,t) = \frac{1}{L_x}\int_{0}^{L_x}\overline{a}(x,z,t)\,\mathrm{d}x\,. \tag{4.7}$$

This requires interpolation in z direction. Over three-dimensional terrain, the flow components are calculated analogously. For the ensemble mean, the averaging is performed on the σ levels over each subdomain:

$$\overline{a}(x,y,z,t) = \frac{1}{TA_{\mathrm{sub}}}\int_{t-T}^{t}\iint_{A_{\mathrm{sub}}} a(x',y',z,t')\,\mathrm{d}x'\,\mathrm{d}y'\,\mathrm{d}t'\,, \tag{4.8}$$

where A_{sub} is the subdomain area. Then, the domain average over the total domain area A_{tot} gives a vertical profile again:

$$\langle\overline{a}\rangle(z,t) = \frac{1}{A_{\mathrm{tot}}}\iint_{A_{\mathrm{tot}}}\overline{a}(x,y,z,t)\,\mathrm{d}x\,\mathrm{d}y\,. \tag{4.9}$$

4.3.3 Joint probability density functions

The vertical turbulent flux of a variable ϕ is determined by the covariance of its turbulent part ϕ' with the perturbation of the vertical wind w'. Here, we refer to the turbulent flux averaged over the x-y plane at a given height z above sea level. In case of discrete model data, this can be expressed by the sum over all N data points at that height:

$$\langle\overline{w'\phi'}\rangle(z) = \frac{1}{N}\sum_{n=1}^{N} w'(z,n)\phi'(z,n) \tag{4.10}$$

The use of terrain-following coordinates implies that model levels are not horizontal, so vertical interpolation is required to obtain w' and ϕ' from the LES data. A continuous probability density function can be found to describe the two-dimensional histogram

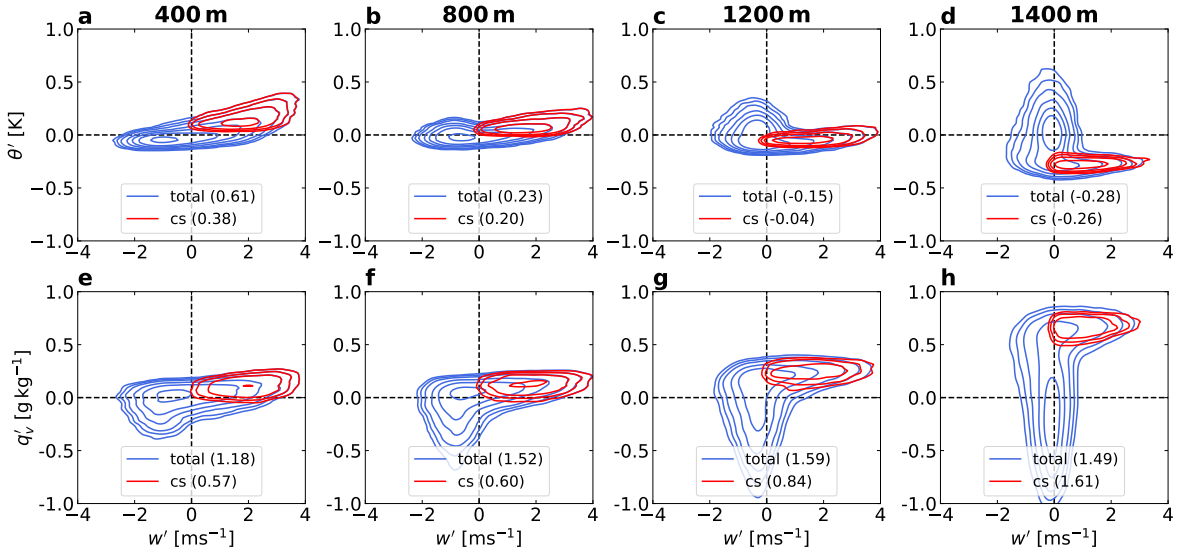

Figure 4.1: Joint probability density functions (JPDFs) of the turbulent vertical velocity fluctuation w' and (a)-(d) the turbulent potential temperature fluctuation θ' as well as (e)-(h) the turbulent specific humidity fluctuation q_v' for FLAT at 4 h on different height levels (boundary-layer depth $\approx$ 1500 m). Numbers in brackets in the legends represent the total vertical flux as well as the contribution of the coherent structures (cs), each normalized by the surface flux. Iso-probability contours are at 0.05×10^{-3}, 0.1×10^{-3}, 0.2×10^{-3}, 0.5×10^{-3}, 0.001, 0.002, 0.005, and 0.01.

of w' and ϕ' so that:

$$\langle \overline{w'\phi'} \rangle (z) = \iint w'\phi' f(z, w', \phi') \, \mathrm{d}w' \, \mathrm{d}\phi' \,, \tag{4.11}$$

where $f(z, w', \phi')$ is the so-called joint probability density function (JPDF) which is normalized to unity. In this study, the JPDFs are fitted to the model data via a gaussian kernel density estimation (KDE). With the help of the updraft sampling, a JPDF for the contribution of the plumes to the total turbulent flux can be specified as well. Figure 4.1 shows the turbulence statistics for the turbulent heat and moisture flux over flat terrain for demonstration. Per definition, the JPDF for the non-local mixing by the coherent structures (red) corresponds to positive vertical-wind components. The small but still positive densities for $w < 0$ are an artifact and a drawback of the gaussian KDE. At the selected time, the boundary-layer height is about 1500 m. Especially in the lower half of the boundary layer, the probability density is highly skewed towards the first quadrant. At 800 m, the coherent structures are responsible for almost 90 % of the turbulent heat flux. Up to this height, they solely feature positive potential-temperature perturbations. In higher altitudes, the overshooting thermals are cooler than their environment. For the turbulent moisture flux (Fig. 4.1e to h), the JPDF for the coherent transport is generally located in the first quadrant as moisture

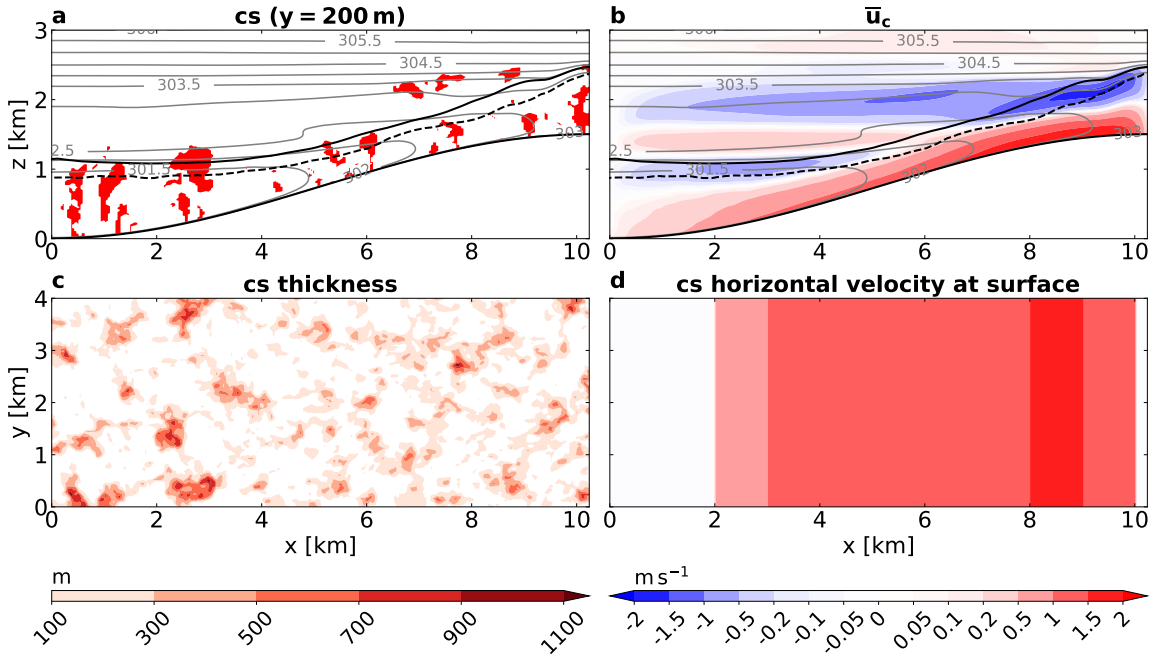

Figure 4.2: Slope cross-sections for REF at 4 h showing (a) the contours of the coherent structures (cs) obtained by conditional sampling and (b) the horizontal wind component of the slope-wind circulation as well as the isolines of the potential temperature in K. The mixed and the boundary-layer height, illustrated as a dashed and a solid line, respectively, are obtained from the temperature gradient as in Weinkaemmerer et al. (2022a). (c) vertical thickness of the structures in top view and (d) horizontal component of the structures' bulk velocity at 10 m above ground.

is transported away from the moist surface layer to the drier air above. Thus, the moisture-enriched coherent structures are more dominant at higher levels.

4.4 Analysis of the idealized-valley simulation

4.4.1 Boundary-layer plume characteristics

In this section, the results of the conditional sampling will be characterized for the idealized-valley case. As an example, Figure 4.2a shows a cross section of the valley at an arbitrary point in y direction. This is after a spin-up time of 4 h when the simulation is expected to represent typical midday conditions. It can be seen that plume structures have evolved all along the valley cross section whereby their size scales with the boundary-layer height. The tallest structures can be found in the valley center and over the ridges. As the boundary layer is a spatially averaged quantity, also overshooting plumes occur. To some degree, also elevated structures appear above the boundary-layer height which are decoupled from the surface. A comparison with

Fig. 4.2b shows that these structures are located in the recirculation zone above the ridges. Fig. 4.2b also reveals that the slope-wind circulation has formed two vertically stacked circulation cells as it is typical for deep valleys (Wagner et al., 2015). Roughly, the mixed-layer height coincides with the height of the upslope branch of the cross-valley circulation. The highest horizontal wind velocities prevail at higher altitudes in the slope-wind layer close to the ridge. In top view, Fig. 4.2c confirms that the deepest structures can in fact be found over the valley bottom, where the boundary layer is deepest and the slope winds are weak. Here, the boundary layer resembles most closely the horizontally homogeneous boundary layer over flat terrain.

It is a goal of this study to gain insight into the characteristics of the plumes in the slope-wind layer and how they interact with the slope wind. From one time step to the next, the plumes seem to move upslope while they are evolving and decaying. Instead of identifying individual convective objects, as in Griewank et al. (2022), and then tracking their motion, we estimate the bulk velocity of coherent structures with an image correlation analysis (Fig. 4.2d). Thereby, the sampled structures are shifted in slope direction until the spatial correlation with the structure pattern of the following sampling step (1 min ahead) reaches a maximum. This is only done in the lowest vertical model layer and in intervals of 1 km along the x axis. From the extent of this horizontal shift, a bulk velocity of the coherent structures can be calculated. The result shows that the horizontal velocity of the coherent structures over the valley slope is comparable to the surface wind speed. At higher altitudes, this technique does not produce reliable results because of the rapid changes in the shape of the structures due to turbulent motions. However, as the plumes between $x = 4\,\mathrm{km}$ and $x = 7\,\mathrm{km}$ are mostly limited to the slope-wind layer, it can be assumed that their bulk transfer velocity does not differ substantially from $\overline{u}_c$.

4.4.2 Heat and moisture flux decomposition

Based on the conditional sampling, the contribution of the coherent structures to the vertical turbulent flux of heat and moisture can be quantified. To this end, the turbulent flux is decomposed into a coherent-structure part (top-hat representation), a second term expressing the in-structure variability of the updrafts, and a third term representing the turbulence in the environment outside the plumes (Siebesma and Cuijpers, 1995; Couvreux et al., 2010):

$$\overline{a'b'} = \alpha(1-\alpha)(\overline{a}^i - \overline{a}^e)(\overline{b}^i - \overline{b}^e) + \alpha(\overline{a'b'})^i + (1-\alpha)(\overline{a'b'})^e, \tag{4.12}$$

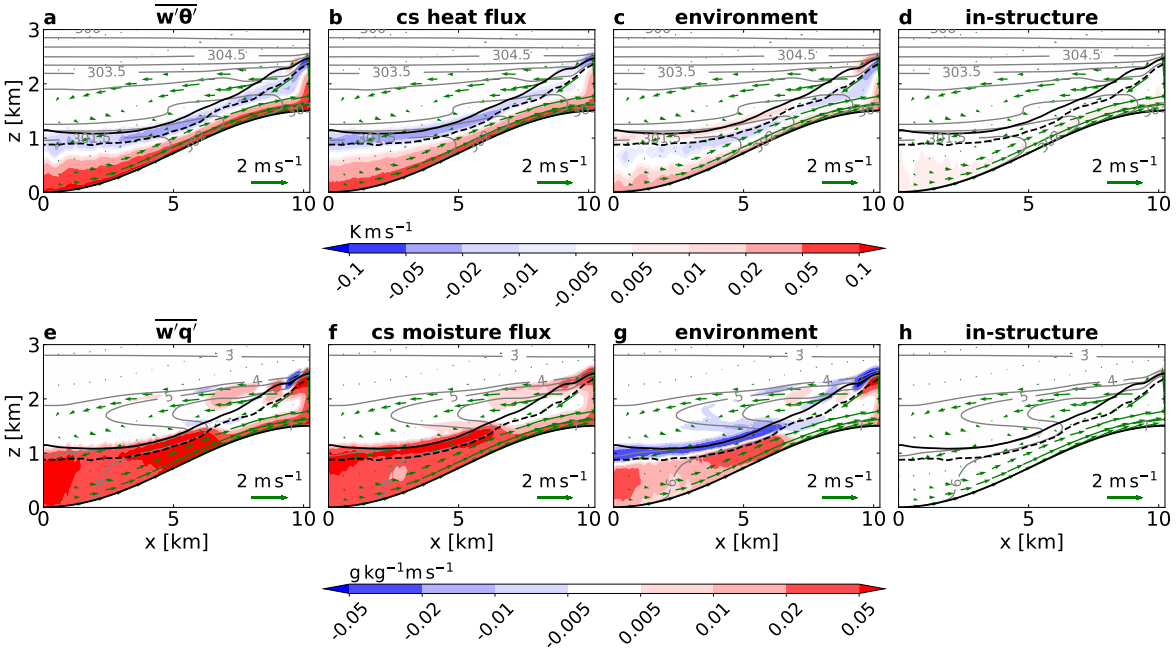

Figure 4.3: Slope cross-sections for REF at 4 h showing (a) the total turbulent heat flux, (b) the turbulent heat-flux contribution from the structures, (c) from the environment, (d) from the in-structure variability, and (e)-(h) for the turbulent moisture flux, respectively. Also shown are the slope-wind vectors as well as (a)-(d) the potential temperature in K and (e)-(h) the specific humidity in g kg^{-1}.

where α is the local coherent-structure coverage, the index i stands for in-structure, and e for environment. This means that the calculation of the ensemble mean according to Eq. (4.6) is carried out either over the grid points inside or outside the structures. The resulting cross-section plots are shown in Fig. 4.3. It is striking that the in-structure variability of the turbulent fluxes is almost negligible both for the heat and the moisture flux. This confirms the coherency of the sampled updrafts. Generally, the total turbulent flux (Fig. 4.3a and e) is dominated by the plumes. For the heat flux, Fig. 4.3b shows that the positively buoyant coherent structures generally cause a positive turbulent heat flux in the lower half of the boundary layer all along the valley cross-section. In the entrainment zone, the heat flux turns negative due to overshooting plumes which are cooler than their environment in terms of the potential temperature. The environmental turbulent heat flux counteracts the effect of the plumes to some extent, except in the lower boundary layer, where it has a positive contribution as well (Fig. 4.3c). At the boundary-layer top, for instance, this traces back to descending positive potential-temperature perturbations and ascending negative ones. A different picture is shown by the turbulent moisture flux, where the contribution from the plumes is overall positive. Negative contributions originate from the environmental turbulence in the entrainment zone. While the basic vertical structure of the flux contributions

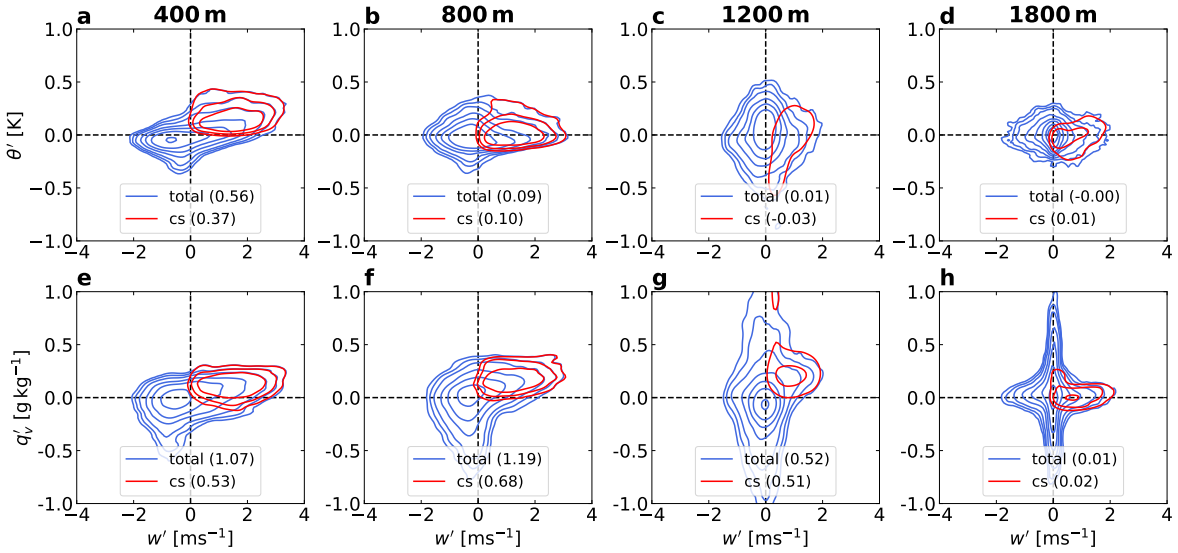

Figure 4.4: As in Figure 4.1, but for REF. The height level of (d) and (h) is raised to 1800 m in order to cover the elevated regions over the ridges.

can be observed similarly over flat terrain (not shown), a noticeable difference is the area between $x = 7\,\text{km}$ and $x = 9\,\text{km}$, where the moisture accumulations are reaching out from the ridges towards the valley center. Here, the turbulent moisture flux contributions are almost zero (Fig. 4.3f and g). From this, it can be concluded that the horizontal moisture transport in this area is mainly achieved by the slope-wind circulation (see the horizontal component of the upper circulation cell in Fig. 4.2b).

4.4.3 JPDFs over the idealized valley

Over the idealized valley, the JPDFs are calculated on horizontal levels of constant height (Fig. 4.4). This means that different flow regimes are intersected. For instance, the 800 m level crosses the entrainment zone in the valley center and the slope-wind layer. At 400 m height in the valley center, the JPDF still resembles the statistics over flat terrain. However, the range of the potential-temperature and specific-humidity fluctuations is clearly higher while the vertical-wind velocities are slightly smaller. At slope height (800 m), the total turbulent heat flux is considerably diminished compared to the same height level over flat terrain. At 1800 m, both the turbulent heat and the turbulent moisture flux are nearly disappearing (that is, the JPDFs are nearly centrally symmetric).

Turbulent heat flux

In order to represent the full vertical transport, the contributions from the slope-wind circulation can be included in the flux statistics (Fig. 4.5). With that, the density

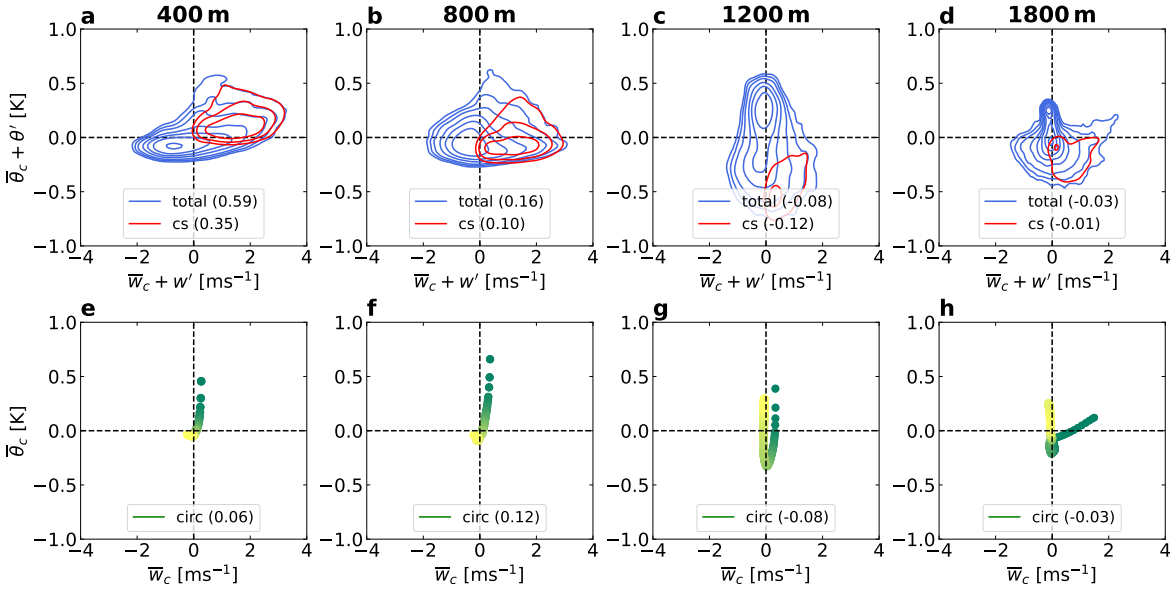

Figure 4.5: As in Figure 4.4a-d, but showing (a)-(d) the local-circulation components combined with the turbulent fluctuations and (e)-(h) only the local-circulation components of the total heat flux. In (e)-(h), one data point stands for one intersected grid cell. Green shadings are close to the slope, yellow ones close to the valley center.

function for the heat flux at 400 m is asymmetric towards positive temperature perturbations at low vertical wind velocities in contrast to Fig. 4.4, where a negative bulge was apparent. At 800 m, the total heat flux only has a slightly smaller value compared to flat terrain, although the influence of the coherent structures is considerably smaller. This leads to the conclusion that a large amount of heat is transported by the slope winds. Above, the JPDFs on higher altitudes are more difficult to interpret. This is because of the high horizontal inhomogeneity between the updraft regions over the ridges and the largely non-turbulent areas of subsidence over the valley center. Thus, the total vertical heat flux at these heights is generally small.

Turbulent moisture flux

The JPDFs of the vertical moisture flux including the contributions from the slope-wind circulation (Fig. 4.6) show a similar picture. Primarily, the total flux values are significantly higher than over flat terrain and reach about twice the surface flux at 800 m. Fig. 4.6e-h indicates that a large amount of moisture is transported by the slope-wind circulation. Different to FLAT, the coherent structures even include negative flux values in the valley (Fig. 4.6a and b, fourth quadrant). This is explained by plumes of drier air advected from the valley center to the moist slope wind layer by the horizontal mean flow. The drying of the valley center is a result of the subsiding branch of the cross-valley circulation (Weinkaemmerer et al., 2022a). A comparison

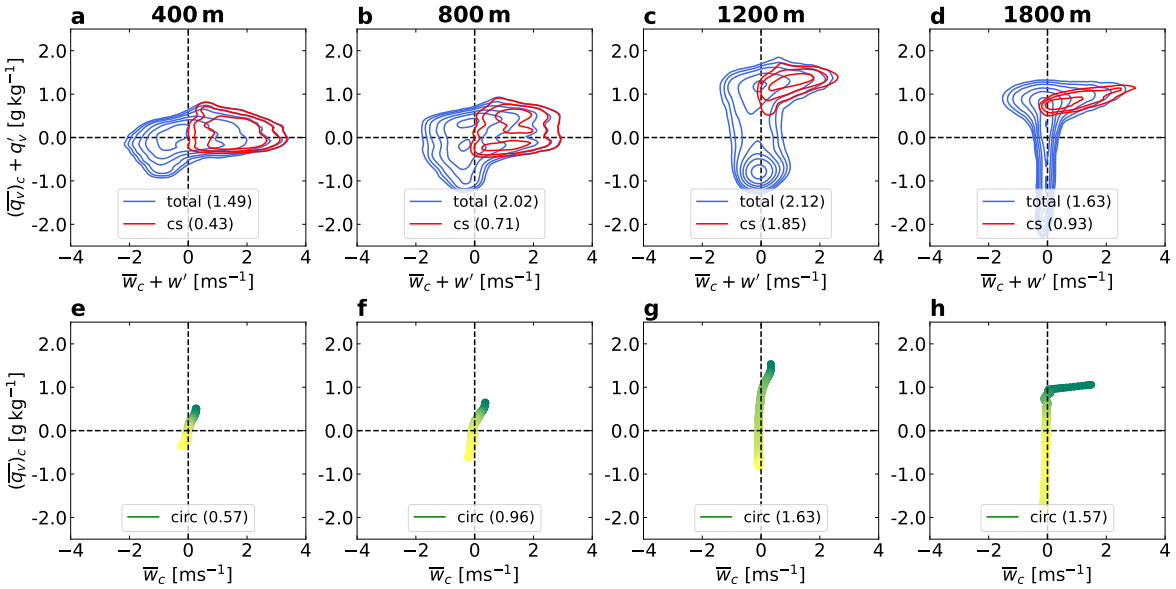

Figure 4.6: As in Figure 4.5, but for moisture.

of Fig. 4.4h and Fig. 4.6d shows that the moisture transport by turbulence is nearly negligible at upper levels.

4.4.4 Role of the slope-wind circulation

Fig. 4.5h and Fig. 4.6h show well how the thermal circulation determines the shape of the total JPDFs. As already mentioned, the slope-wind circulation takes on a significant amount of the vertical heat and moisture transport. For the heat flux, this applies especially to the slope-wind layer (Fig. 4.5f) while for the moisture flux, the contribution from the mean circulation clearly exceeds the coherent-structure part, especially in the slope-wind layer (Fig. 4.6f) and at the height of the hilltop plumes (Fig. 4.6h). Generally, the maximum vertical mean wind values in Fig. 4.5e-g and Fig. 4.6e-g can be assigned to the slope flow. Mostly, they also coincide with the highest $\overline{\theta}_c$ and $(\overline{q}_v)_c$ values. Conversely, data points with negative $\overline{w}_c$ belong to the recirculation (see Fig. 4.5g). In case of the heat flux, this downward movement together with the upward movement of negative temperature fluctuations leads to a negative contribution to the heat flux (Fig. 4.5g and h, second and fourth quadrant). For moisture, in contrast, the circulation part of the flux is dominated by the first and the third quadrant meaning that its total value is overall positive.

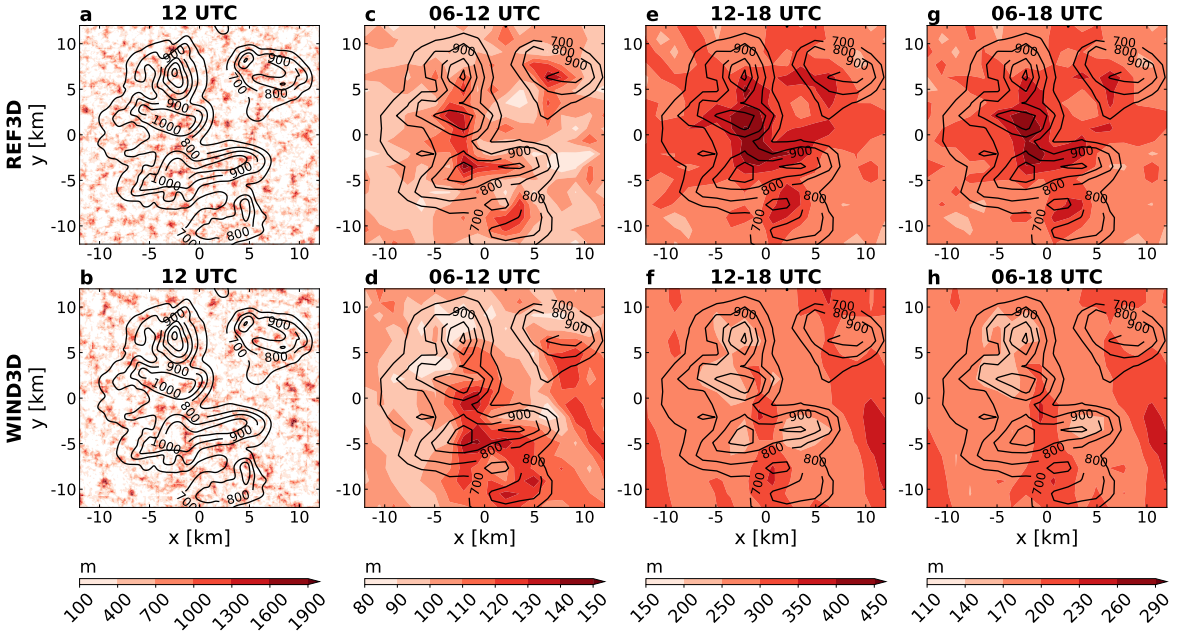

Figure 4.7: Vertical thickness of the coherent structures over three-dimensional orography (height of the isolines in m) at 12 UTC (after 6 h simulation time) for (a) REF3D, (b) WIND3D, and (c)-(h) the mean vertical thickness averaged over each subdomain at a 1 min interval over (c)-(d) the first 6 h of simulation, (e)-(f) the second 6 h of simulation, and (g)-(h) the whole simulation time.

4.5 Analysis of the three-dimensional simulations

4.5.1 Reference case

In this section, the simulations over three-dimensional terrain are analyzed. Figure 4.7a depicts the result of the conditional sampling for the REF3D case at midday (12 UTC) after 6 h of simulation. The terrain features a group of hills with heights of 500 m above a surrounding plain. The sampled plumes are evenly distributed over the domain and the orography does not seem to have a significant impact on their strength. The boundary layer is about 1.5 km deep at this time meaning that the hills are rather shallow compared to the boundary-layer depth. In Fig. 4.7a, also artifacts of the subdomain decomposition are visible showing up as edges in the data field aligning with the subdomain boundaries.

Again, the plumes can not be treated independently from the thermal circulation. The effect of the slope-wind circulation becomes apparent in Fig. 4.7c and e showing that the temporally averaged plume height is maximal on the ridges. This impression is strengthened by the 12 h average (Fig. 4.7g). It means that the plumes are more frequent on the mountain tops where they converge horizontally due to the upslope winds. This has a distinct effect on the time-averaged statistics and is in accordance

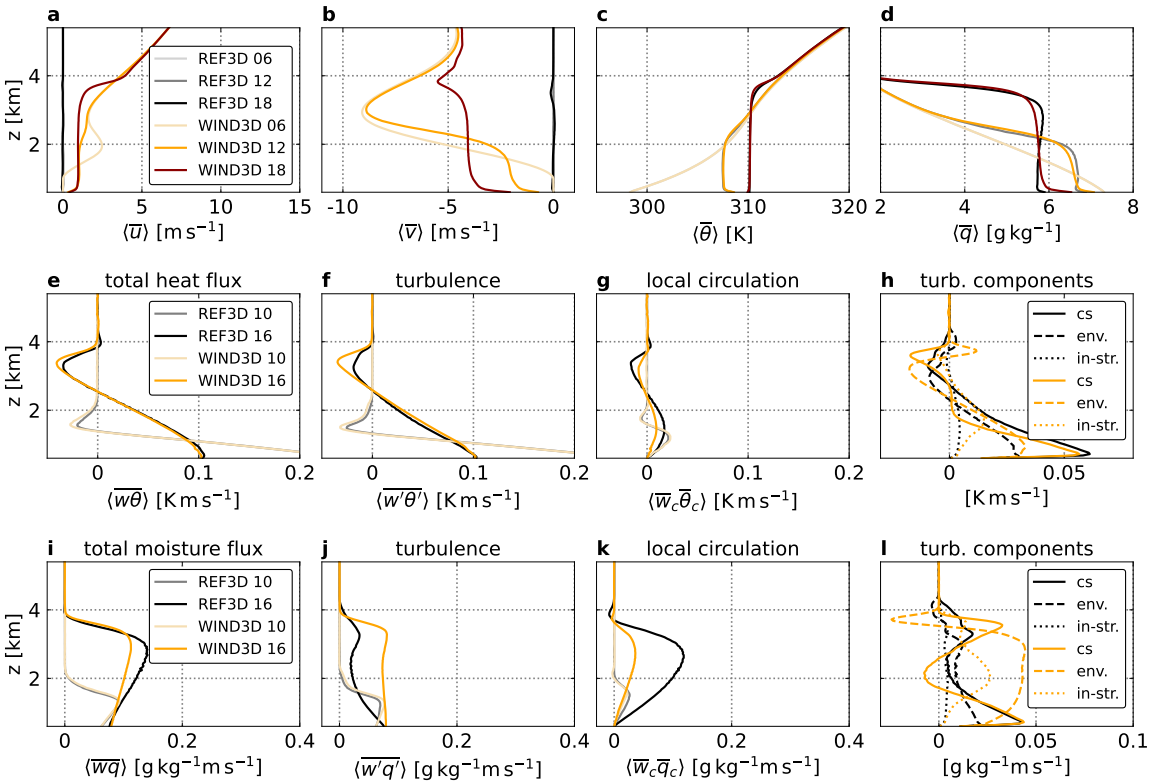

Figure 4.8: Domain-averaged profiles of (a)-(d) the zonal wind u, the meridional wind v, the potential temperature θ, and the specific humidity q_v for REF3D and WIND3D at initialization (06 UTC) and different later times. (e) the total heat flux, (f) the turbulent heat flux, and (g) the local-circulation component. The turbulent part includes the subgrid contribution. (h) the decomposition of the resolved turbulent heat flux according to Eq. (4.12) for REF3D and WIND3D. (i)-(l) analogously for the moisture flux.

with the positive vertical mean flow over the tops visible in Fig. 4.3. Without time averaging, as in Fig. 4.2c, no evident accumulation or intensification of the plumes over the hilltops was found. This is because the conditional sampling is based on the local tracer-concentration statistics (in particular, the standard deviation of the tracer concentration). Although seeming counter-intuitive at the first glance, this is consistent with the decomposition of the flow into a domain average, a local mean value, and a turbulent fluctuation. With that, it can be seen that the scale of the mean circulation is sufficiently separated from the scale of the coherent structures. At the same time, this shows that the subdomains are reasonably sized. In other words, a smooth orography has no big impact on the instantaneous characteristics of the individual boundary-layer plumes as the turbulent motions live on a smaller scale than the thermal circulation.

4.5.2 Impact of an upper-level wind

Similarly to the local mean flow, also a large-scale, upper-level wind can be expected to have an impact on the temporally-averaged plume density. In the WIND3D case, the direction of the prevailing background wind is northwesterly. As the comparison of Fig. 4.7c and d shows, the effect of the large-scale wind only becomes apparent in the temporal average. The average over the first 6 h of simulation shows that the frequency of the plumes on the windward, northwestern side of the ridges is diminished compared to REF3D. This is linked to an increase in the plume frequency on the leeward slopes. The differences intensify in the second half of the simulation (Fig. 4.7e and f) when the plumes are generally less persistent on the wind-exposed hills compared to the surrounding plain. Due to the generally taller plumes in the afternoon, this pattern also dominates the 12 h mean (Fig. 4.7g and h).

The upper-level wind also influences the vertical structure of the boundary layer. The domain-averaged profiles of the horizontal wind components at 18 UTC (and at 12 UTC for comparison) are presented in Fig. 4.8. The figure also shows the impact of the upper-level wind on the potential-temperature and specific-humidity profiles compared to REF3D. Although the effect is small, the outcome confirms the finding of Weinkaemmerer et al. (2022a) that the temperature profile stays almost unaffected while the export of moisture from a valley to the free atmosphere is reduced depending on the valley depth and the atmospheric stability. This seems to be true also over a three-dimensional orography of shallow hills without long, deep valleys. The 12 UTC curves show that the upper-level wind mainly takes effect in the second half of the day, at least in this case. This is when the mean distribution of the plumes differs most between REF3D and WIND3D (see Fig. 4.7). At 10 UTC, the domain-averaged flux profiles of REF3D and WIND3D still overlap (Fig. 4.8e-g and i-k). This time has been picked to be representative for the late morning conditions. Studying the contributions to the vertical moisture flux from turbulence and local circulation (Fig. 4.8i-k) at 16 UTC reveals that the moisture transport by the circulation is strongly reduced in the WIND3D case, which is partly counteracted by an increase in turbulent exchange, as described in Weinkaemmerer et al. (2022a). This increase of the turbulent moisture flux traces back to the environmental turbulence and, partly, to the coherent structures (Fig. 4.8l). Also, the in-structure variability plays a significant role in the WIND3D case. This indicates that the plumes are more irregular and inhomogeneous than in the reference case, where this contribution is almost negligible. The in-structure variability is also increased for the turbulent heat flux (Fig. 4.8h). All in all, there is a strong sensitivity of the turbulent components and the local circulation to the upper-level wind, especially for the moisture flux. This makes it difficult to draw a direct connection

from the spatial plume prevalence (Fig. 4.7) to the vertical moisture transport as other turbulence and the slope-wind circulation generally play a big role. The main impact of an upper-level wind on the vertical moisture transport is due to the reduced advective transport by the slope winds.

4.6 Conclusions

For this study, (semi-)idealized LES have been carried out over both a quasi-two-dimensional periodic valley and a three-dimensional, smoothed real orography featuring a group of hills. Driven by a prescribed, constant surface heat flux or by time-dependent solar radiation, respectively, an almost cloud-free convective boundary layer develops which is typical for daytime, fair-weather conditions. The convective boundary layer is characterized by thermal updrafts or plumes being part of the small-scale, turbulent motions. These plumes are often referred to as coherent structures or organized turbulence. In contrast to flat terrain, the boundary-layer structure over mountains and hills is horizontally inhomogeneous and thermally-induced slope winds emerge as a local mean flow. A conditional sampling method has been used to identify the coherent structures in order to analyze the simulations with a focus on the plume characteristics. The implementation of the conditional sampling is consistent with the flow decomposition presented in Weinkaemmerer et al. (2022a), where a local average is defined besides a background value and a turbulent part. The main findings can be summarized as follows:

- It is found that, in convective conditions, the coherent structures in the mountain boundary layer are influenced by both the thermally-induced winds and the background, upper-level wind. In the slope-wind layer, the plumes are moving upslope with about the speed of the slope wind. In consequence, the temporally averaged plume thickness is highest on the crests of the hills. The coherent structures make up the dominant contribution to the vertical heat flux.

- In analogy with the CBL over flat terrain, the non-local transport related to the boundary-layer plumes in the complex-terrain CBL is evident in the irregular shape of the joint PDFs of vertical velocity, potential-temperature and specific-humidity fluctuations. In the CBL over mountains, the features of the joint PDFs can be well explained by the properties of the thermally-driven mean circulation. The joint PDFs show that the advection of coherent turbulent structures by the thermally-driven flow is a dominant process in the CBL over orography. Generally, the coherent structures are less relevant here as the local circulation takes

on a greater weight. Also, the turbulent entrainment at the top of the CBL is partly replaced by the downward components of the mean circulation.

- An upper-level wind reduces the vertical moisture transport and, especially on the windward hillsides, the frequency of plumes. The partitioning of the vertical moisture flux between plumes and local circulation is very sensitive to the upper-level wind. Also, the non-organized turbulence outside of the plumes plays a more significant role if a large-scale wind is present.

For future research, the experimental setup should be extended to various atmospheric conditions and different Bowen ratios. Also, the possibility of cloud formation should be taken into account in order to investigate how the vertical transport of heat and moisture by (organized) turbulence and mean flows and its sensitivity to a background wind changes with the onset of clouds. So far, the results of this study are also applicable to tracers or pollutants in general.

Regarding parameterization development, no clear path can be given. Several authors suggest joint-Gaussian JPDFs to describe turbulent fluxes (Wyngaard and Moeng, 1992; Wang and Stevens, 2000; Chinita et al., 2018). However, the JPDFs over the idealized valley are far more asymmetric than over flat terrain. In fact, their shape is largely determined by the local circulation. This finding lends credibility to early attempts of parameterizing vertical heat transport over complex terrain on the basis of analytical models of the slope wind system, such as the Prandtl model (e.g., Noppel and Fiedler, 2002). However, although the idea of parameterizing the mass-flux component of subgrid-scale fluxes with a slope-wind model is conceptually attractive, practical implementations must consider the documented shortcomings of the underlying theory. For instance, recent studies (e.g., Zardi and Serafin, 2015) demonstrated that the steady-state Prandtl model is heavily inaccurate at representing upslope wind speed and temperature anomalies at shallow slope angles and weak stratification. Also, the sensitivity of the individual contributions from turbulence and mean circulation to a background wind, especially for the tracer/moisture transport, complicates parameterization design.

Acknowledgments

This research was funded by Hans Ertel Centre for Weather Research of DWD (3rd phase, The Atmospheric Boundary Layer in Numerical Weather Prediction), Grant Number 4818DWDP4 and by the Deutsche Forschungsgemeinschaft (DFG, German

Research Foundation), TRR 301, Project-ID 428312742. The contributions of Matthias Göbel and Stefano Serafin to this research were funded by the Austrian Science Fund (FWF), Grant P30808-N32; a CC BY or equivalent license is applied to the author accepted manuscript and the version of record arising from this submission, in accordance with the grant's open access conditions. The authors declare no conflict of interests.

Chapter 5

Stratus over rolling terrain: LES reference and sensitivity to grid spacing and numerics

Jan Weinkaemmerer[1,2], Ivan Bašták Ďurán[1,2], Stephanie Westerhuis[3,4], Jürg Schmidli[1,2]

1 – Institute for Atmospheric and Environmental Sciences, Goethe University Frankfurt, Frankfurt/Main, Germany

2 – Hans Ertel Centre for Weather Research, Offenbach, Germany

3 – Center for Climate Systems Modeling, ETH Zürich, Zürich, Switzerland

4 – Federal Office of Meteorology and Climatology, Zürich, Switzerland

Abstract

The formation of a low stratus cloud over idealized hills is investigated using numerical model simulations. The main driver for the cloud formation is radiative cooling due to outgoing longwave radiation. Despite a purely horizontal flow, the advection terms in the prognostic equations for heat and moisture produce vertical mixing across the upper cloud edge leading to a loss of cloud water content.

This behavior is depicted via a budget analysis. More precisely, this spurious mixing is caused by the diffusive error of the advection scheme in regions where the sloping surfaces of the terrain-following vertical coordinate intersect the cloud top. This study shows that the intensity of the (spurious) numerical diffusion strongly depends on the horizontal resolution, the order of the advection schemes, and the choice of the scalar advection scheme. A Large Eddy Simulation (LES) with 4 m horizontal resolution

serves as a reference. For horizontal resolutions of a few hundred meters, carried out with a model setup as it is used in Numerical Weather Prediction (NWP), a strong reduction of the simulated liquid-water path is observed. In order to keep the (spurious) numerical diffusion at coarser resolutions small, at least a fifth-order advection scheme should be used. In the present case, a WENO scalar advection scheme turns out to increase the numerical diffusion along a sharp cloud edge compared to an upwind scheme. Furthermore, the choice of the vertical coordinate has a strong impact on the simulated liquid-water path over orography. With a modified definition of the sigma coordinate, it is possible to produce cloud water where the classical sigma coordinate does not allow any cloud formation.

5.1 Introduction

The presence and the formation of fog affect the flow and the visibility within the atmospheric boundary layer. This influences transportation by air and land, solar power generation, and the dissipation of air pollution. Therefore, it is important to accurately forecast fog (Nemery et al., 2001; Forthun et al., 2006; Gultepe et al., 2007; Köhler et al., 2017; Gultepe et al., 2019). The different kinds of fog are named after the processes that lead to their formation, e.g., radiation fog, advection fog, or evaporation-mixing fog (Whiteman, 2000). Radiation fog develops when the near-surface air cools below its dew-point temperature due to outgoing longwave radiation during nighttime. Often this fog is lifted up and forms an elevated cloud layer referred to as a low stratus (Scherrer and Appenzeller, 2014). For Numerical Weather Prediction (NWP) models, the accurate simulation of fog and low stratus is challenging due to the variety of the involved physical processes occurring on differing spatial and temporal scales including radiation, local flow, small-scale turbulence, microphysics, and land-atmosphere interaction (e.g., Van der Velde et al., 2010; Steeneveld et al., 2015). These processes are not explicitly resolved on the numerical grid and thus need to be represented by parameterization. NWP studies for radiation fog over flat terrain (Steeneveld et al., 2015; Steeneveld and de Bode, 2018) show a high sensitivity to the land-surface physics and the parameterized turbulent mixing. Also, the choice of the microphysical scheme has been identified as a key element.

More detailed high-resolution studies require the use of Large-Eddy Simulation (LES) techniques with a very high spatial resolution of up to the 1 m-scale in order to resolve the energy-containing eddies in the stable boundary layer. This was first done by Nakanishi (2000), who describes the further development of radiation fog after its onset in calm conditions: When the foggy air mass has grown vertically, radiative cooling at

the top of the now optically thick fog causes turbulent mixing by negatively buoyant air leading to the formation of a stronger adiabatic lapse rate within the fog layer (see also Price, 2011, 2019). Also Bergot (2013) observed organized turbulent structures during the evolution of radiation fog, e.g., rolls at the top of the fog layer associated with high values of turbulent kinetic energy (TKE). The transition from shallow stably stratified fog to well-mixed radiation fog is also affected by aerosols (Boutle et al., 2018). LES model results are not always found to provide a consistent benchmark for fog prediction (Boutle et al., 2022). However, recent studies (e.g., Smith et al., 2021) show that fog simulation in NWP models profits from an increased resolution of up to 100 m. These sub-kilometer scale NWP models are becoming more and more common in operational use, at least for limited areas (Boutle et al., 2016).

Most existing fog studies are limited to flat terrain, even if surface inhomogeneities are accounted for (Bergot et al., 2015). Only a few LES studies focus on fog or low stratus over complex terrain (Bergot and Lestringant, 2019). However, the NWP representation of low stratus over complex terrain tends to suffer from inaccuracies. Mostly, some kind of terrain-following vertical coordinate system is used to represent orography in NWP models. Schär et al. (2002) show how such a coordinate transformation increases the error of advective transport. In this study, we want to address the issue of erroneously dissipating low stratus which was investigated by Westerhuis et al. (2020) in a NWP study focusing on the Swiss Plateau. The spurious mixing between adjacent levels of the terrain-following vertical coordinate (in this case, the Smooth LEvel VErtical coordinate, SLEVE, Schär et al., 2002; Leuenberger et al., 2010) was identified as the root cause (Westerhuis et al., 2021). Over mountainous terrain, sloping coordinate surfaces intersect the typically flat cloud top of fog and low stratus leading to an increased mixing between cloudy and cloud-free grid cells due to the numerical diffusion of the advection scheme. This phenomenon is also observed in other applications of terrain-following coordinates, e.g., as spurious diapycnal mixing in ocean models (Marchesiello et al., 2009). An alternative vertical coordinate formulation with a local smoothing of the model levels seems to mitigate the spurious diffusion considerably (Westerhuis and Fuhrer, 2021).

Apart from the vertical coordinate formulation, the impact of the model dynamics on the fog life cycle has received little attention in the literature. Mazoyer et al. (2017) analyzed the impact of the dynamics on the microphysics in a LES of a radiation-fog event with 5 m horizontal and 1 m vertical resolution over flat terrain including surface drag by canopy. They compared different momentum advection schemes: A fourth-order centered scheme and two third and fifth-order implicitly diffusive WENO (weighted essentially non-oscillatory, Shu, 1998) schemes. The different diffusivities

of the schemes significantly affected the fog life cycle. Especially the highly diffusive third-order scheme led to an unrealistic increase in the liquid water path due to the dissipation of small-scale turbulent structures at the top of the fog layer resulting in reduced entrainment of dry air.

Upwind advection schemes, being odd-ordered, are inherently diffusive (Hundsdorfer et al., 1995). A fifth-order upwind scheme, for instance, can be written as a combination of a sixth-order discretization and an additional sixth-order derivative term. This introduces dissipation as the sixth-order derivative term acts as an artificial diffusion term with a diffusivity proportional to the Courant number (Wicker and Skamarock, 2002). The dissipation is largest for short wavelengths (i.e. at strong gradients). Also even-ordered schemes, though non-dissipative, do produce numerical errors due to dispersive oscillations, e.g., at inversions or strong moisture gradients (Matheou and Teixeira, 2019). This can also augment the spurious dissipation (Pressel et al., 2017). The purpose of WENO schemes is to suppress oscillations and numerical artifacts in non-smooth regions with discontinuities or sharp gradients, while maintaining a high accuracy of the solution in smooth regions of the flow. In smooth regions, an arbitrarily high accuracy can be achieved. The main idea is to use a weighted combination of several local reconstructions based on different stencils in order to form the final reconstruction. By using nonlinear weights, several lower-order interpolation polynomials are either combined into a higher-order discretization in smooth parts or to a lower-order approximation in non-smooth parts of the solution. Similar to upwind schemes, also WENO schemes show diffusive properties (Pantano et al., 2007). In case of LES, the numerical dissipation of the advection scheme combines with the subgrid model to an effective subgrid model. This can affect the results as long as the simulation is not well resolved (Brown et al., 2000).

Knowing the effect of terrain-following vertical coordinates on fog dissipation over a hilly topography, it is still not clear how other numerical aspects like the type of the advection scheme and the order of advection influence fog and low cloud simulation over terrain. In this paper, we want to investigate this aspect systematically and compare between rolling and flat terrain at a range of different horizontal grid spacings from the meter scale up to 1 km. Another goal is to better understand the mechanisms behind the spurious cloud dissipation by performing a detailed budget analysis for heat and moisture and to quantify the possible improvement achieved by an alternative vertical coordinate formulation. In order to analyze the resolution dependence, multiple idealized simulations of a low stratus cloud are carried out over a simplified valley-ridge topography using regular upwind advection schemes and WENO schemes of different order.

This paper is structured as follows: In the next section, the budget analysis and the horizontal averaging method are introduced. The experimental setup and the numerical model is presented in section 5.3. In section 5.4 to 5.5, the results of the simulations are discussed. Conclusions are given in section 5.6.

5.2 Budget analysis

5.2.1 Flow averaging and decomposition

With the aim to compute statistical quantities like variances and covariances and to evaluate the local budgets of heat and water, the flow needs to be decomposed into turbulent fluctuations and a corresponding ensemble mean using averaging operators (Schmidli, 2013). In the simulations with orography, a sinusoidal valley is used which is oriented along the meridional or y direction of the domain (see the cross sections in Fig. 5.1). Both in zonal and meridional direction, periodic boundary conditions are imposed, imitating an infinitely long valley. The symmetry of this quasi-two-dimensional setup used in this study simplifies the decomposition of the flow (Weinkaemmerer et al., 2022a).

First, the turbulent fluctuations are separated from the mean flow by a Reynolds decomposition. For a quantity $a(x, y, z, t)$, the required ensemble (Reynolds) average is approximated by an average in time and in the along-valley direction:

$$\overline{a}(x, z, t) = \frac{1}{TL_y} \int_{t-T}^{t} \int_{0}^{L_y} a(x, y', z, t') \, \mathrm{d}y' \, \mathrm{d}t' \,, \tag{5.1}$$

where x, y, and z is the eastward, northward, and vertical direction, respectively; and t is time. Note that z denotes the height above the valley floor. We use a time-averaging period of $T = 20\,\mathrm{min}$ as a compromise between accuracy and stationarity. The sampling time is 1 min. L_y equals the meridional domain length. Thus, the flow is decomposed into an ensemble mean part $\overline{a}$ and a local turbulent part a':

$$a(x, y, z, t) = \overline{a}(x, z, t) + a'(x, y, z, t). \tag{5.2}$$

For the sake of clarity, subgrid-scale fluctuations not resolved in the LES are not written out here and are treated as being included in the turbulent part. Following the Reynolds averaging rules, the ensemble mean of a product is given by:

$$\overline{ab} = \overline{(\overline{a} + a')(\overline{b} + b')} = \overline{a}\,\overline{b} + \overline{a'b'}. \tag{5.3}$$

Note that the second-order turbulent fluxes consist of a resolved and subgrid part:

$$\overline{a'b'} = \overline{a'b'}|_{res} + \overline{a'b'}|_{sgs}. \tag{5.4}$$

For the analysis, the subgrid parts are obtained from the LES subgrid turbulence model.

5.2.2 Heat and water budgets

Each term of the conservation equations for heat and water is computed directly from the prognostic equations of the model and averaged as described in Weinkaemmerer et al. (2022a). This way, the budgets of potential temperature, water vapor mixing ratio, and cloud water content are obtained. The budgets are comprised of the total tendency (TOT), the advection term (ADV), the diffusive part of the advection (DIFF), the tendencies from the microphysical model (MP), and the tendencies from parameterized turbulence, either from the LES subgrid turbulence model or the boundary-layer scheme (PBL) in the NWP case. Additionally, the potential-temperature budget includes a radiation term (RAD).

5.3 Numerical model simulations

5.3.1 Experimental setup

The low stratus case is investigated over a periodic, infinitely long sinusoidal valley. Hence, the setup is quasi-twodimensional. The orography is described by:

$$z_s(x) = \frac{h}{2}\left(1 - \cos\frac{2\pi x}{W}\right), \tag{5.5}$$

where z_s is the surface height, h the ridge height from valley floor to crest, and W the width of the valley from ridge to ridge. The simulations presented in this study feature a relatively shallow valley with a height h of 200 m and a width W of 4.096 km which also equals the domain width and length. Rotation is neglected. The initial atmosphere is in hydrostatic balance and the cloud water content is zero everywhere. The initial profiles of temperature, specific humidity, and wind are loosely derived from a radiosonde sounding launched at Payerne, Switzerland (491 m ASL) on 25 December 2017, 00 UTC. An extensive low stratus cloud with a vertical extent of several hundred meters persisted over Payerne on that day, details are described in Westerhuis et al. (2020). The initial profiles of potential temperature, water vapor mixing ratio, and zonal wind are displayed in Fig. 5.2a. A nearly adiabatic residual layer with a moist

Table 5.1: List of model configurations depending on the horizontal resolution.

Horiz. res.	Domain height	Vertical resolution	Subgrid model
4 m	7 km (2 km sponge)	4 m (0-800 m) to 20 m (3.2-7 km)	TKE
8 m	8 km (2 km sponge)	4 m (0-40 m) to 20 m (2.8-8 km)	TKE
16 m	"	"	TKE
32 m	"	"	TKE
64 m	"	8 m (0-40 m) to 40 m (2.8-8 km)	PBL
128 m	"	"	PBL
256 m	"	"	PBL
512 m	"	"	PBL
1024 m	"	"	PBL

TKE, 1.5-order TKE scheme (Deardorff, 1980); PBL, Mellor-Yamada Level-3 model (Nakanishi and Niino, 2006).

ground level is capped by a distinct inversion at a height of 500 m. The zonal wind speed continuously increases with height up to $7\,\mathrm{m\,s^{-1}}$ as well as the meridional wind speed (not shown). The wind direction is approximately 45° to the valley axis at all height levels. There is no additional forcing of the flow during the simulation. Radiative forcing is used in combination with an interactive land-surface model. The total duration of the simulations is 6 h. We lay a special focus on the situation after 6 h assuming it to be representative for typical early morning conditions before sunrise. Thereby, a sufficient amount of time is left for model spin-up. The domain sizes for the experiments are listed in Tab. 5.1. In addition to the experiments with orography, several simulations are carried out over a flat surface (FLAT) with the same setup as it is used over the valley.

5.3.2 Numerical model

The numerical simulations are performed using the CM1 model (Cloud Model 1, Bryan and Fritsch, 2002). CM1 is a nonhydrostatic, fully compressible numerical model that can be run in both LES and NWP mode. It uses terrain-following σ coordinates. This means that the nominal height of a coordinate surface is given by

$$\sigma = \frac{z_t(z - z_s)}{z_t - z_s}, \tag{5.6}$$

depending on the height z, the surface height of the orography $z_s(x, y)$, and the height of the model top z_t. In general, metric terms (G_x, G_y, and G_z) are required to account for this coordinate transformation when calculating spatial gradients, e.g., in the advection operator. The model is integrated using third order Runge-Kutta time

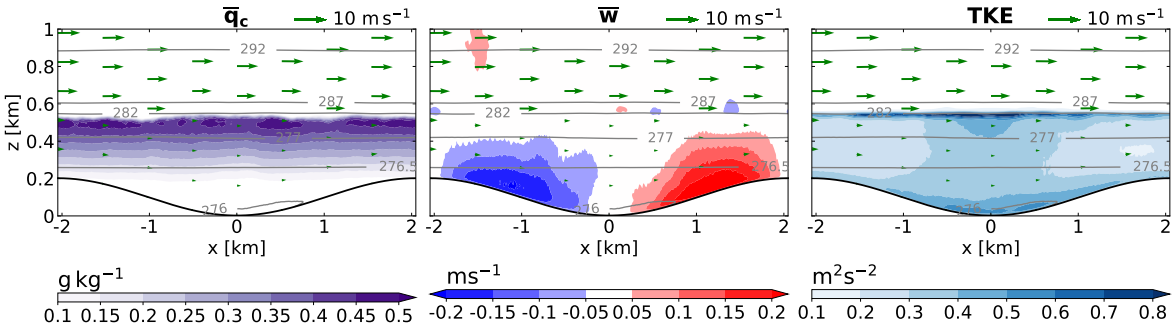

Figure 5.1: Valley cross sections showing the averaged cloud water content $\overline{q}_c$, the averaged vertical wind speed $\overline{w}$, and the turbulent kinetic energy (TKE) at $t = 6\,\mathrm{h}$ for the REF case. Also showing the cross-valley wind vectors and the isolines of the potential temperature in K.

differencing (Wicker and Skamarock, 2002). For the default setup, a fifth-order WENO scheme is used both for the advection of scalars and momentum (Jiang and Shu, 1996; Borges et al., 2008). Alternatively, a regular upwind scheme can be used (Wicker and Skamarock, 2002). Grid stretching is applied in the vertical above a certain minimum height. The level thickness gradually increases with altitude (see Tab. 5.1). The model top is a rigid lid. In order to suppress spurious gravity-wave reflections, a sponge layer with Rayleigh damping is employed ($\tau = 300\,\mathrm{s}$). The model uses an adaptive time step with a typical value of 0.5 s for the LES runs and several seconds for the NWP simulations. At a horizontal resolution of 32 m and below, the simulations are computed in LES mode using a 1.5-order TKE scheme (Deardorff, 1980) for the subgrid-scale turbulence closure. For the NWP simulations, a Mellor-Yamada Level-3 model is used for parameterizing the planetary boundary layer (Nakanishi and Niino, 2006). Microphysical processes are parameterized using the Thompson double-moment scheme (Thompson et al., 2008). Atmospheric radiation is parameterized by the RRTMG scheme (Iacono et al., 2008). For the land-surface model (revised MM5 scheme, Jiménez et al., 2012), the grassland option is selected.

5.4 Description of the LES reference

In this study, the highest-resolution LES simulation (4 m horizontal resolution) will serve as a reference case (REF) for the following sensitivity tests employing coarser grid spacings. Figure 5.1 shows cross-sections of the final model state after 6 h. This is still during nighttime, hence the simulations are not affected by solar radiation. An approximately 400 m thick low stratus layer has formed directly above the ridges. The cloud density increases gradually from the bottom to the top of the stratus layer

(a) With orography (REF), height above valley floor:

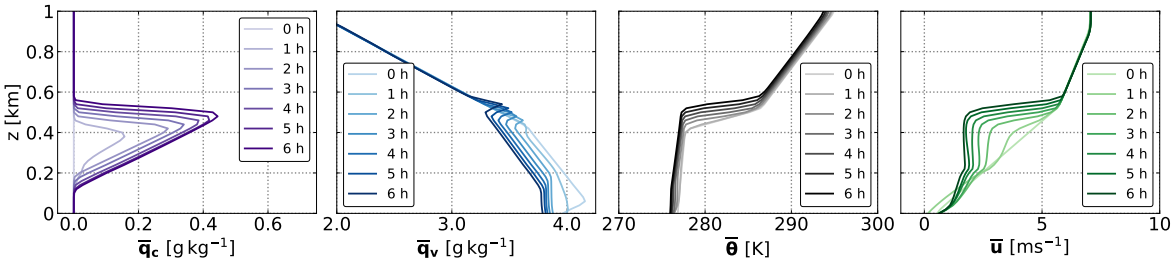

(b) Without orography (FLAT, 8 m horizontal resolution):

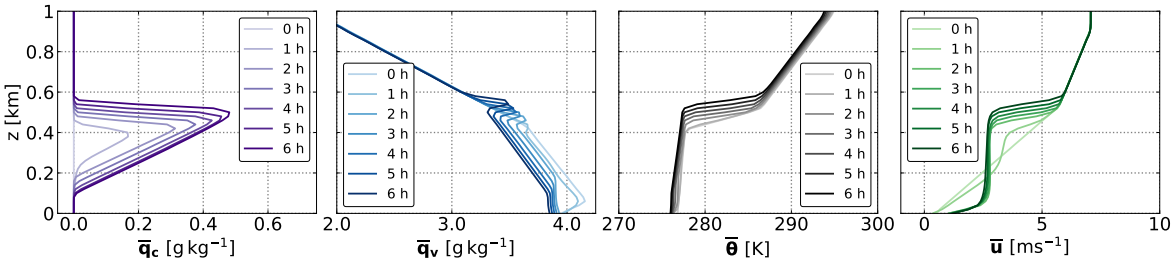

Figure 5.2: Domain-averaged profiles of the cloud water content q_c, the water vapor content q_v, the potential temperature θ, and the zonal wind u, shown every hour.

resulting in a fairly sharp upper cloud edge. The top coincides with a layer of strong wind shear. The mean vertical wind turns out to be negative over the western slope and positive over the eastern slope indicating that the wind is roughly following the orography. Significant TKE values occur within the stratus layer and in the cloud-free zone at the valley bottom. The TKE is highest along the cloud top where strong wind shear prevails. A budget analysis for the TKE (not shown) reveals that it is both shear driven (by the large-scale horizontal wind along the cloud top as well as by the local surface winds in the valley) and buoyancy driven (mainly in the center of the domain due to negatively buoyant air sinking from the cloud top). The averaged subgrid TKE is less than 4 % of the total TKE everywhere except in the lowest 50 m of the surface layer.

The temporal evolution of the REF case is displayed in Fig. 5.2a. The cloud water concentration gradually increases with time. Simultaneously, the water vapor concentration decreases within the stratus layer and also in the cloud-free zone below. Directly above the cloud top, a slight moistening can be observed. With the growth of the stratus layer, also the height of the nearly neutrally stratified boundary layer increases. Due to an overall cooling caused by longwave radiation, the average temperature of the boundary layer decreases over time. During the first hours of simulation, the zonal wind profile in the boundary layer adapts to the nearly adiabatic temperature profile resulting in an almost constant wind speed between 200 m and 500 m and

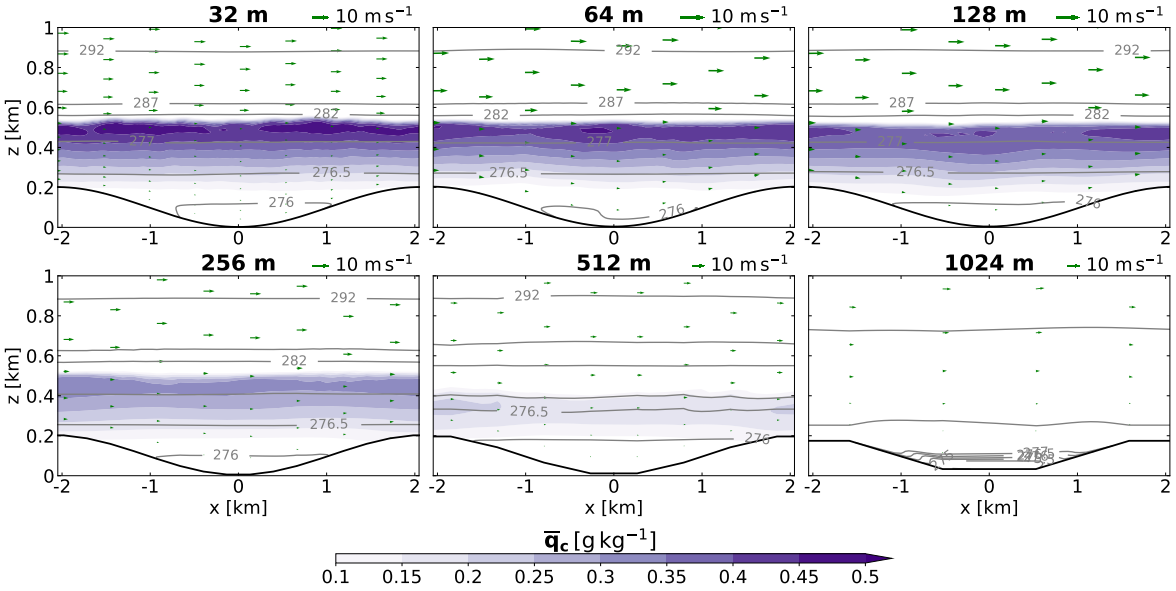

Figure 5.3: Valley cross sections showing the mean cloud water content for different horizontal resolutions: 32 m (default LES setup) and 64 m to 1024 m (default NWP setup) at $t = 6$ h. Also showing the cross-valley wind vectors and the isolines of the potential temperature in K.

a distinct velocity jump at the inversion height. This shows that the boundary layer is well mixed. For the meridional wind along the valley axis, the temporal evolution is fairly similar with slightly higher wind speeds inside the valley (not shown).

The evolution of the near-surface atmosphere over flat terrain is qualitatively very similar (Fig. 5.2b). The cloud water content in the stratus reaches slightly higher values. Furthermore, due to the lack of orographic drag, the wind velocities are higher below 500 m.

5.5 Sensitivity to resolution and advection scheme

5.5.1 Resolution dependence

Figure 5.3 shows valley cross sections together with the mean cloud water content at different resolutions. The 32 m simulation was conducted with the LES setup. The coarser the horizontal grid resolution, the thinner and shallower the stratus cloud becomes. At 1024 m only four grid points are left in x direction and the representation of the orography becomes highly non-smooth. In accordance with the cloud dilution, the temperature inversion below 600 m weakens for coarser resolutions and disappears completely at 1024 m.

Figure 5.4 shows the budget terms for the potential temperature, the water vapor

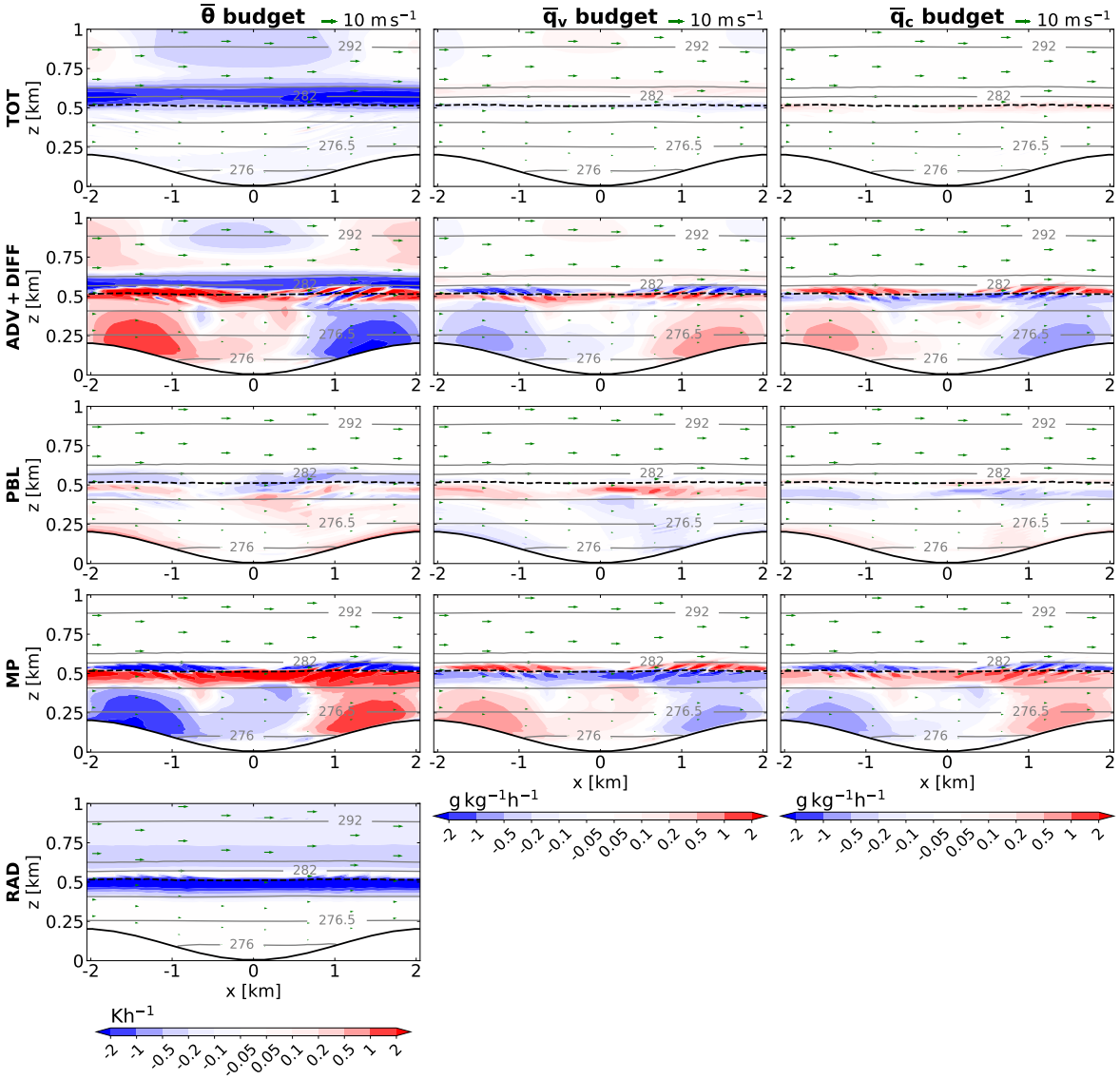

Figure 5.4: Valley cross sections as in Fig. 1, but showing the local budget terms for heat (left column), water vapor (center column), and cloud water (right column) for the default NWP setup with 256 m horizontal resolution at $t = 6$ h. The budget terms comprise the total tendency (TOT), the advection including implicit diffusion (ADV+DIFF), the tendencies from the boundary-layer scheme (PBL) as well as from the microphysical model (MP), and the radiative tendencies (RAD). The dashed black line marks the contour of the cloud top ($0.1\,\mathrm{g\,kg^{-1}}$).

content, and the cloud water content for the default NWP setup with 256 m horizontal resolution. At this resolution, the effect of the spurious diffusion becomes significant. The valley is represented by 16 grid points in cross-valley direction. Looking at the total tendencies (TOT, upper row), the horizontally homogeneous cooling above the top of the stratus layer is striking, while slightly positive q_c tendencies around 500 m show that the stratus is still growing vertically. The latter are associated with negative q_v tendencies in the same region (partly due to condensation, partly due to the growth of the cloud layer) and slightly positive q_v tendencies above. The total θ tendencies are composed of a vertical mixing of heat across the inversion by (implicit numerical) diffusion (ADV+DIFF) leading to a warming around the top of the cloud layer (see dashed line). This local warming is partly balanced by negative θ tendencies from the microphysics (MP) due to evaporation corresponding to negative microphysical tendencies for q_c. Beneath the cloud top (below 500 m), the positive θ tendencies from advection-diffusion as well as from the microphysics due to condensation are outweighed by strong radiative cooling (RAD). The PBL tendencies are small for all three quantities.

Areas of non-zero advection-diffusion tendencies in the budgets directly over the slopes and around 900 m height are related to local subsidence (western slope) and ascent (eastern slope, see also Fig. 5.1). Within the stratus, these tendencies are balanced by microphysical processes. Consequently, the vertical transport of θ, q_v, and q_c across the top of the stratus layer must be largely caused by numerical diffusion as there is no vertical wind present at this height and small-scale turbulent motions are not resolved at this resolution. In total, the temperature and moisture gradients at the top of the stratus cloud are still growing mainly because of strong radiative cooling leading to a gain in q_c due to condensation (see MP in the q_c budget). However, this growth is reduced by numerical diffusion across the cloud top (see ADV+DIFF in the q_c budget). In the q_v budget, the advection-diffusion tendencies are essentially opposite to q_c. Consequently, also the microphysical tendencies are mainly of opposite sign.

The spurious mixing explains why the stratus layer is thinner for coarser resolutions and the boundary layer is generally warmer. The advection-diffusion tendencies around the cloud top reach a maximum over the slopes where the vertical coordinate levels are steepest and the angle between the σ surfaces and the mostly horizontal q_c iso-surfaces is highest.

In order to study the impact of the order of advection and the type of the advection scheme used on the cloud evolution, the domain-averaged liquid-water path (LWP) is compared for a variety of sensitivity tests over a range of horizontal resolutions (Fig. 5.5a). Over orography, the LWP increases and converges for higher resolutions as

(a) With orography:

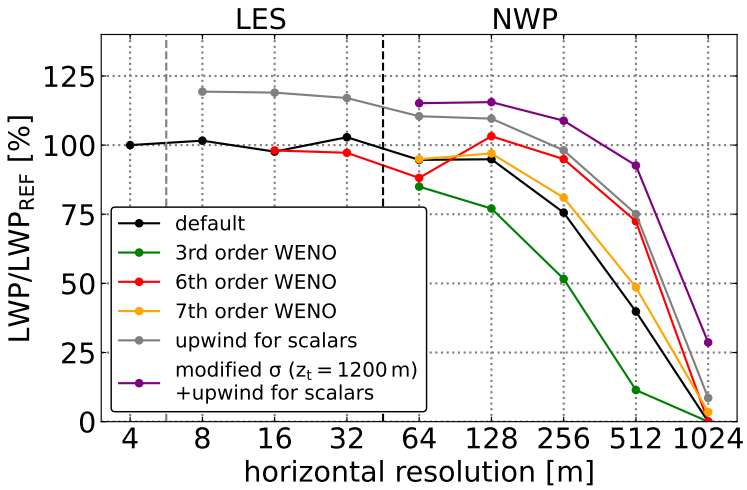

(b) Without orography (FLAT):

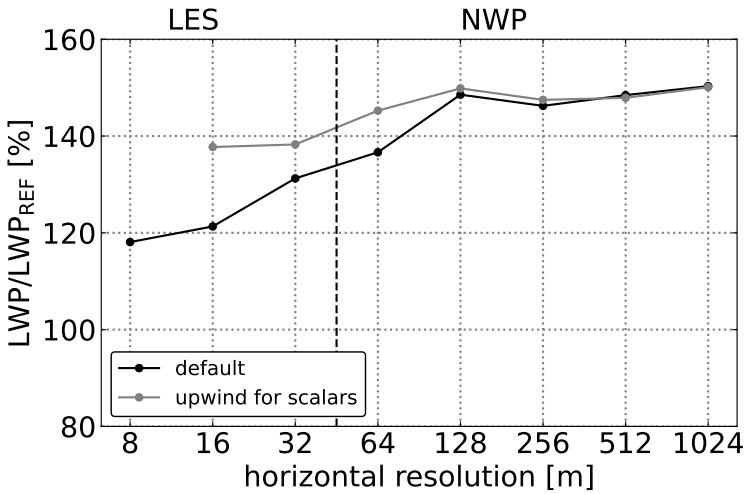

Figure 5.5: Domain-averaged liquid-water path (LWP) at $t = 6\,\mathrm{h}$ obtained from several sensitivity tests for resolution, order of advection, type of advection scheme, and vertical coordinates both normalized by the LWP of the REF simulation. The dashed black line marks the change from LES to NWP setup (see Tab. 5.1).

the effect of the numerical diffusion diminishes. The default simulations have also been carried out over flat terrain for comparison (Fig. 5.5b). Here, the LWP continuously decreases for resolutions higher than 128 m. This opposite behavior is probably due to another effect which dominates over flat terrain in absence of spurious mixing: Resolved small-scale turbulent processes enhance the entrainment of dry air at the top of the stratus layer and lead to cloud dissipation (Mazoyer et al., 2017). For the default FLAT simulations, the LWP does not converge at high resolutions.

5.5.2 Order of advection and WENO

The effective resolution of a model is determined by the smallest resolved wavelength and can be deduced from kinetic energy spectra (Skamarock, 2004). A lower-order advection scheme with increased numerical diffusion results in an overall lower effective resolution. Comparing a third-order scheme for momentum advection to higher-order or central schemes, Lunet et al. (2017) and Mazoyer et al. (2017) observed an overestimation of the LWP due to enhanced dissipation of TKE reducing the entrainment of dry air at the top of the stratus cloud. Analogously to the resolution dependence, the results are different over the idealized orography of this study as numerical diffusion is an important factor (Fig. 5.5a). A reduction of the horizontal and vertical advection order from fifth to third order leads to a significant decrease in LWP of partly more than 20 %. On the other hand, an increase from fifth to seventh order increases the LWP only by a small amount.

In contrast to that, using a fifth-order upwind instead of a fifth-order WENO scheme for scalar advection enhances the amount of cloud water by about 20 % on average (Fig. 5.5a). A comparison with a sixth-order centered scheme without implicit diffusion indicates that the fifth-order WENO scheme for scalars is in fact too diffusive, at least for the simulations with grid spacings coarser than 64 m. For the sixth-order simulations, a small amount of artificial sixth-order diffusion was added in order to ensure numerical stability. As a result, this shows that the use of a WENO scheme for scalar advection is not always beneficial around sharp gradients where it reduces the effective order of advection and thus increases implicit numerical diffusion. At higher resolutions, there is still a systematic discrepancy between the WENO and the upwind-scheme simulations, also over flat terrain where no spurious mixing occurs (Fig. 5.5b). Based on this idealized study, it cannot be finally assessed which results are more realistic. For the FLAT simulations, however, the upwind scheme shows a better convergence at high resolutions and is generally less resolution dependent.

5.5.3 Role of the vertical coordinate

According to Westerhuis and Fuhrer (2021), the effect of spurious numerical diffusion at coarser resolutions associated with the vertical coordinate can be partially mitigated by a stronger damping of the orographic signal with height. Principally, this leads to less steep coordinate surfaces intersecting the flat cloud top. While this can be achieved by a local smoothing of the model levels, this study uses a simpler approach. In Eq. (5.6), z_t is reduced significantly such that the transition to flat model levels occurs at a lower height. Above z_t, the coordinate levels are completely flat. This implies that the metric term G_z is not independent of height anymore. For $z > z_t$, the metric terms take the values $G_x = G_y = 0$ and $G_z = 1$. For $z_t = 1200\,\mathrm{m}$, the effect of this modification can be seen in Fig. 5.5a for the simulations with a fifth-order upwind scheme for scalar advection. The improvement is most significant for coarser resolutions. Even the 1024 m simulation is able to form a significant amount of cloud water. However, a further decrease of z_t did not lead to a significant further enhancement. This approach has also been tested by Westerhuis et al. (2020) running the COSMO model over a small, low-altitude region of the Swiss Plateau. The findings are similar but underline the challenging nature of this problem: Reducing z_t is only applicable in a domain without high mountains and steep slopes.

5.6 Conclusion

For this study, idealized simulations of a low stratus event have been carried out over both hilly and flat terrain. The low stratus forms during nighttime due to radiative cooling. The sensitivity of the cloud formation with respect to the grid spacing, the type of the advection scheme for scalars, the order of advection, and the vertical coordinate formulation has been investigated. The horizontal resolutions cover the full range from a few meters (LES range) to (sub-)kilometer NWP resolutions. In terms of the scalar advection, WENO schemes of different order have been compared to a regular upwind scheme. The upper cloud edge turns out to be relatively sharp as it is accompanied by a distinct temperature inversion and a jump in the wind velocity. Terrain-following coordinate levels intersecting the cloud top cause implicit diffusion across the cloud edge due to the diffusive part of the advection scheme. This leads to spurious mixing as illustrated with the help of the cloud water budget. In consequence, this results in an erroneous cloud dissipation and a reduction of the LWP. The main findings from the different sensitivity tests summarize as follows:

- Over orography, the numerical diffusion associated with the advection of heat and moisture is more resolution dependent than over flat terrain. While the

LWP shows a good convergence in the LES range, it is strongly reduced for coarser resolutions. This originates from the combination of a terrain-following sigma coordinate with a diffusive upwind or WENO advection scheme. For the accurate simulation of fog and low clouds over orography, it is recommended that the relevant orographic features are represented by $\mathcal{O}(30)$ grid points in order to minimize errors due to advection in a terrain-following coordinate system. This means that kilometer-scale NWP simulations are not able to produce accurate results over terrain with orographic features of several kilometers size, for cases comparable to the present one. With an optimized vertical coordinate and a higher-order advection scheme, however, reasonable results can be obtained if relevant orographic features are represented by $\mathcal{O}(10)$ grid points.

- The order of the scalar advection has a strong impact on the formation of fog and low stratus, especially at resolutions which are actually too coarse for the length scales of the terrain (see above). For the WENO scheme studied here, a order of five or six seems to be a good compromise. However, a seventh-order scheme does not show a strong improvement compared to a fifth-order scheme. For the presented case study, the WENO scheme turns out to be in fact more diffusive than the regular upwind scheme. Around strong gradients, WENO schemes tend to reduce the effective order of advection in order to avoid oscillations. Over orography, the fifth-order upwind-scheme simulations produce around 20 % more LWP than the WENO-scheme simulations over all horizontal resolutions. At low resolutions, the fifth-order upwind scheme is comparable with the sixth-order scheme which produces no diffusive but dispersive errors instead. Based on these findings, an upwind or centered scheme for scalar advection seems to be preferable for cloud simulations with strong gradients. It has to be mentioned that for the momentum advection, a WENO scheme has been used for all simulations in order to avoid numerical instabilities due to the strong wind shear.

- We can confirm that the choice of the vertical coordinate has a strong impact on the fog evolution (Westerhuis et al., 2021). Going to higher resolutions in the LES range, the influence of the vertical coordinate decreases. With our simple approach of reducing z_t, so that the model levels become horizontal at a lower height, a considerable increase in the LWP could be achieved for the NWP simulations even at the lowest resolution. However, this only works for a domain with a rather shallow orography.

- Over flat terrain, the cloud top is aligned with the vertical model levels. Thus, spurious mixing induced by the misalignment of the inversion and the coordinate

surfaces does not occur. In this case, the LWP depends on how well small-scale turbulent motions are resolved which lead to vertical mixing at the cloud top and consequent cloud dissipation. Strong wind shear produces a significant amount of TKE along the cloud top. For the coarser resolutions of the NWP simulations, the turbulent structures disappear in the simulations and the LWP increases. However, with an upwind scheme for scalar advection, the resolution dependence is generally weaker.

It has to be kept in mind that many operational NWP models use different kinds of advection schemes, e.g., in order to guarantee positive definite solutions for tracer transport. These have not been tested here which is a limitation of this study. More sophisticated vertical-coordinate definitions (Westerhuis and Fuhrer, 2021) are a promising approach to improve the simulation of fog and low stratus over orography. As the cloud top is principally aligned with the isentropes, a hybrid isentropic-sigma vertical coordinate (Toy, 2013) would possibly also help to mitigate the problem of numerical diffusion. The immersed boundary method, currently implemented in the Weather Research and Forecasting (WRF) model (Lundquist et al., 2010), presents another alternative which avoids sloping vertical coordinate levels. However, to our knowledge, WRF is currently the only major NWP model offering this option. Furthermore, concepts like anti-diffusive flux corrections for WENO schemes (Xu and Shu, 2005) leave room for future research on the topic of spurious diffusion.

Acknowledgments

This research was funded by Hans Ertel Centre for Weather Research of DWD (3rd phase, The Atmospheric Boundary Layer in Numerical Weather Prediction), Grant Number 4818DWDP4 and by the Deutsche Forschungsgemeinschaft (DFG, German Research Foundation), TRR 301, Project-ID 428312742. The authors declare no conflict of interests.

Chapter 6

Summary and conclusions

In this chapter, the main outcomes of this dissertation are summarized. All in all, Paper I and II have led to numerous insights related to the vertical transport of heat and moisture by convective turbulence and thermally-driven flows over complex terrain. Paper III has contributed to the understanding of diffusive errors due to the numerics in the simulation of fog and low stratus over rolling terrain. For all three studies, idealized LES were carried out over hilly terrain driven by prescribed, constant surface fluxes or time-dependent solar radiation. For Paper II, the constraint of quasi-two-dimensional terrain was relaxed towards three-dimensional, smooth orography.

6.1 Turbulent slope winds in the CBL over orography

A key feature of the two CBL studies is the decomposition of the flow into a small-scale turbulent part, a local mean circulation, and a large-scale background flow as well as the distinction between turbulent and advective transport. Coming back to the first research question, to improve the understanding of vertical heat and moisture exchange in the convective boundary layer over mountainous terrain, several new insights have been gained which are worth to be added to future discussions. They mainly refer to the fair-weather boundary layer in a terrain of low hills or moderate alpine valleys where the land surface is not too heterogeneous and the variety of flow regimes is limited to small-scale turbulence, local slope flows, and a large-scale background wind. The full variety of the mountain-wind system present in many real-world mountain regions with its mesoscale circulations over multiscale orographic features is not covered in this study. However, we were able to extract interesting findings even from rather idealized experimental setups and meteorological cases which we nevertheless assume to be generally applicable. Principally, they arise from the existence of an intermediate flow regime, the slope-wind circulation, between the turbulent and the synoptic scale.

The major findings are summarized as follows:

- The main effect of the thermally-induced circulation is to export moisture out of a valley through the slope-wind layer and to accumulate moisture over the mountain tops. This builds up a horizontal moisture gradient between the ridges and the valley center. In contrast, the temperature distribution is more or less horizontally homogeneous, as the local circulation is directly driven by temperature gradients and acts to reduce them. We have shown that this is not limited to deep, alpine valleys but also applies to low hilly terrain.

- Distinguishing between advective and turbulent transport, it was found that moisture is mainly transported by the slope flows while turbulent exchange plays a smaller role for its vertical transfer. In contrast, turbulent mixing plays the dominant role in the heating of the mixed layer. The thermally-driven circulation is mainly balancing horizontal temperature gradients and contributes less to the vertical heat exchange. Paper I also focused on the turbulence budgets of the turbulent fluxes and the turbulent kinetic energy (TKE). A comparison of the turbulent-flux budgets between flat and complex terrain shows that the gradient-production terms are reduced because of additional advection terms arising from the thermally-driven circulation. In case of the TKE budget, these additional transport terms act as a sink of TKE in the lower part of the valley. This, however, is probably depending on the actual case as it would also be possible by local flows such as along-valley winds to provide a source of TKE by increasing the shear production.

- A key result of this thesis found in Paper I and revisited in Paper II is the effect of an upper-level wind on the vertical heat and moisture transport in the CBL over complex terrain. An upper-level wind has a minor impact on the temperature profile, as the temperature distribution is already fairly horizontally homogeneous, but it strongly affects the moisture distribution by diminishing the strong horizontal moisture gradient between the rather dry valley center and the moist slope region, where the moisture is primarily transported to. In consequence, an upper-level wind leads to a reduced vertical transfer of moisture to levels above the ridge-top height so that more moisture remains within the valley even though the strength of the slope flows is not significantly diminished. Thus, it can strongly reduce the export of moisture out of a valley or, generally, from the mountain base height into the free atmosphere. Similar results were found in a more realistic setup with variable surface fluxes determined by an interactive land-surface model driven by solar radiation. This finding has also

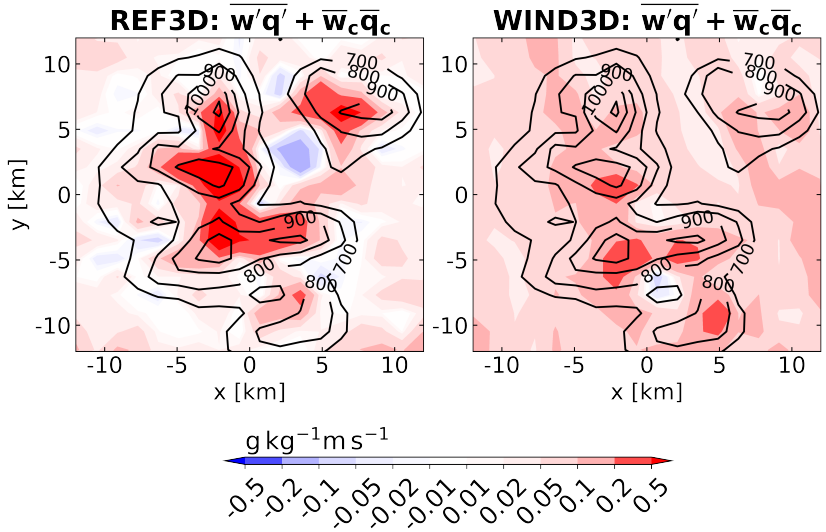

Figure 6.1: Comparison of the 12 h average (06-18 UTC) of the vertical moisture flux contributions from turbulence ($\overline{w'q'}$) and local circulation ($\overline{w}_c\overline{q}_c$) over 3D terrain between the reference case without large-scale wind (REF3D) and the WIND3D case with an upper-level wind from northwesterly directions at a height of 2000 m above sea level.

been corroborated over more realistic, three-dimensional terrain. Furthermore, an upper-level wind excites gravity waves by overflowing the hilltop updrafts as a form of convectively generated gravity waves which also show the typical characteristics of stationary mountain waves.

- In order to enhance the process understanding of convective turbulence over complex terrain, Paper II concentrated on the identification and the analysis of coherent plume structures over an idealized valley and three-dimensional hilly terrain. It was found that the boundary-layer plumes are influenced by both the thermal winds and the background, upper-level wind. In the slope-wind layer, the plumes are moving upslope with about the speed of the slope wind. As a consequence, the plume frequency is highest on the crests of the hills, where the mean vertical wind is also positive. In the temporal and spatial mean, an upper-level wind reduces the frequency of plumes especially on the windward hillsides. This corresponds to a reduced vertical moisture flux mainly because of reduced moisture content in the slope-wind layer which is in accordance with the finding stated above. Figure 6.1 illustrates this finding. Averaged over time, the upwardly transported amount of moisture remains smaller in the WIND3D case. This is not only the case over the hills, also the domain-averaged total moisture flux is smaller than in the REF3D case.

- In the CBL, it is usual to distinguish between local turbulent mixing of diffusive character and non-local transport by thermal updrafts and plumes. In a joint frequency distribution of the perturbations of vertical velocity and temperature or moisture, the diffusive turbulent components can be expected to be arranged symmetrically. The non-local components of the vertical transport related to boundary-layer plumes become evident in the asymmetrical shape of such distributions. Continuous joint probability density functions (joint PDFs) can be derived from the frequency distributions obtained from the model data. In the CBL over complex terrain, the shape of the joint PDFs can be well explained by the contributions from the thermally-driven mean circulation, in addition to the non-local transport by the plume structures. The joint PDFs show that the advection of coherent turbulent structures by the thermally-driven flow is a dominant process in the CBL over orography. Generally, the coherent structures are less relevant here as the local circulation takes on a greater weight. Also, the turbulent entrainment at the top of the CBL is partly replaced by the downward, subsiding components of the mean circulation.

From these studies, it becomes clear that the convective flow over complex terrain, even over shallow hills, is quite different from the widely described flat CBL where heat and mass are mainly transported by small-scale turbulence. Although the simulations are fairly idealized, we expect that the main findings can also be reproduced in more complex, real-case situations. In theory, these results are relevant even over relatively small orographic features, still unresolved in existing NWP models. The findings for the moisture transport are also applicable to tracers or pollutants in general.

Answering the second main research question, to give ideas for improvements of boundary-layer parameterizations and to identify key aspects for possible future parameterization developments, no clear path can be given. One possibility to account for subgrid orography, known from the existing ALPTHERM model, is using the area-height distribution of a given region, i.e. the amount of heated surface area per height level. However, the results of this work point out that it would not be advantageous to base the design of a parameterization on just one parameter, such as the topographic amplification factor. Especially for the moisture exchange, it was found that the vertical fluxes in the CBL over mountains are highly influenced by the advective, non-linear transport by the slope-wind circulation. Parameterizing the flux-component contributed by the slope winds would be very challenging, not only because analytical models of the slope-wind system are highly simplified in general. Furthermore, the strong sensitivity of the vertical mass transport to the large-scale winds above the mountain tops, which was one key finding of this work, is another serious complication.

Often, CBL models contain a bulk parameterization of clear-air or cloud-associated updrafts to account for non-local transport. This concept can not be simply taken over to complex terrain as we have shown how important the process of advection of turbulent structures is in presence of thermally-driven circulations. In summary, the lack of an applicable slope-flow model and the range of interactions reaching from the scale of the turbulent structures to the scale of the synoptic wind make it difficult to think of a practically usable parameterization concept. Even if it was possible, e.g., to fit the kinetic energy of the slope-wind circulation into one parameter, such as the circulation kinetic energy (CKE) determining the heat and mass exchange by the thermally-induced winds, these motions would be almost entirely located in the gray zone. Thus, it would be difficult to achieve results which are independent from the resolution.

As a first step towards improved CBL modeling in NWP, we propose to adapt an existing parameterization for kilometer-scale resolutions where the slope-winds are already reasonably resolved. A subgrid turbulence model could be extended by the advection of parameterized plume structures or subgrid turbulent quantities in general. (Horizontal) gradient terms could be included to account for the effect of the local circulation on the turbulence budgets. The aim is to facilitate the transport of internal energy so that the local boundary-layer height is not overestimated. However, this could also be achieved by other means of correction or by a more or less direct adjustment of the boundary-layer height. As our simulations have shown, the transfer of heat and moisture plays an important role in the relatively shallow slope-wind layer. Here, the surface sensible heat flux can not be directly translated into local growth of the boundary layer.

6.2 Fog simulation in the SBL: Impact of resolution and numerics

In Paper III, we switched to the SBL over rolling terrain. A condensed version of the main results is provided here, details can be found in the publication. In the SBL over orography, spurious dissipation of fog can arise from the interaction of the terrain-following coordinate intersecting the upper cloud edge with the diffusive properties of the advection scheme. The main results of the sensitivity tests comprising different horizontal resolutions and different settings for the advection scheme can be summarized as follow:

- Over orography, the numerical diffusion is more resolution dependent than over flat terrain. The liquid water path (LWP) is strongly reduced for coarser res-

olutions. For the accurate simulation of fog and low clouds over orography, it is recommended that the relevant orographic features are represented by $\mathcal{O}(30)$ grid points in order to minimize errors due to advection in a terrain-following coordinate system. This means that kilometer-scale NWP simulations are generally not able to produce accurate results over terrain with orographic features of several kilometers size. With an optimized vertical coordinate and a higher-order advection scheme, however, reasonable results can be obtained if the relevant orographic features are represented by $\mathcal{O}(10)$ grid points. This applies to this case of strong winds and wind shear. For weaker winds, the errors might be smaller.

- The order of the scalar advection has a strong impact on the formation of fog and low stratus. For the WENO scheme used in this study, an order of five or six seems to be a good compromise. In the studied case, the WENO scheme turns out to be in fact more diffusive than the regular upwind scheme. An upwind or centered scheme for scalar advection can be preferable for cloud simulations with strong gradients.

- The choice of the vertical coordinate has a strong impact on the fog evolution. A considerable increase in the LWP can already be achieved with a rather simple modification to the vertical-coordinate formulation.

- The LWP also depends on how well small-scale turbulent motions are resolved as they cause vertical mixing at the cloud top and consequent cloud dissipation. Thus, the disappearance of turbulent structures at coarser resolutions lets the LWP increase which partly compensates the shortcomings of the terrain-following coordinates.

It has to be mentioned that alternative types of advection schemes used in operational NWP models as well as different ways to define orography in a numerical model, such as immersed boundary conditions, or even anti-diffusive flux corrections, possibly depending on the slope of the coordinate surfaces, are not covered by this research.

6.3 General outlook

From the presented studies, we can see there is room for improvement not only in the description of boundary-layer processes by better parameterizations, but also in improved model dynamics and a more accurate representation of orography in models. In general, numerical errors such as from the advection scheme and the vertical-coordinate definition increase for low resolutions. Also, boundary-layer processes such

as thermally-induced circulations are only poorly represented if the model resolution is too low. Consequently, the vertical transport in the boundary layer might be simulated inaccurately. Although no definitive concept for parameterization development can be presented, we are confident that the results of this work will provide a good reference point for future research. One point that is important to the author of this thesis, is the applicability of the outcomes to less idealized meteorological scenarios. Apart from the strong sensitivity of the heat and mass transport over complex terrain to thermally-driven circulations and, consequently, to the large-scale flow, several more difficulties arise in more realistic mountainous terrain and more realistic setups. There are, e.g., radiative effects due to shading or different land surface characteristics as well as interactions within the mountain wind system over different scales, e.g., along-valley winds influencing the slope-wind circulation. Another important point is the formation of clouds and, consequently, of precipitation. Here, we would anticipate that the results of this study have a significant impact on the onset of cloud formation and the cloud development over complex terrain, especially due to the influence of the slope flows and of the upper-level wind on the vertical moisture transport. However, after clouds have formed over the ridges, this also leads to new feedbacks on the heat and moisture transport, e.g., due to diabatic processes and the feedback of the clouds on radiation. Also, it is possible for shallow convective processes to develop into deep convection and, after precipitation events, the state of the valley atmosphere can be strongly altered due to cold-pool formation. Generally, further experiments in this direction would require the use of the total water content and the liquid-water potential temperature as conserved variables instead of the water vapor content and the potential temperature. In the first place, an interesting next step for future projects would be to reproduce the results of this work in a real-case study, preferably on a larger domain and with more significant orography. This way, it would be possible to assess the significance of the outcomes in more realistic meteorological situations.

Chapter 7

Zusammenfassung

In diesem Kapitel werden die Hauptergebnisse dieser Dissertation zusammengefasst. Insgesamt haben die Arbeiten Weinkaemmerer et al. (2022a) und Weinkaemmerer et al. (2023) zu zahlreichen Erkenntnissen über den vertikalen Energie- und Massentransport durch konvektive Turbulenz und thermisch angetriebene Strömungen über komplexem Gelände geführt. Weinkaemmerer et al. (2022b) hat zum Verständnis von Diffusionsfehlern beigetragen, die aufgrund der Numerik bei der Simulation von Nebel und tiefer Stratusbewölkung über hügeligem Gelände entstehen. In allen drei Studien wurden idealisierte LES über hügeligem Gelände durchgeführt, die durch vorgegebene, konstante Oberflächenflüsse oder die tageszeitabhängige Sonneneinstrahlung angetrieben wurden. In Weinkaemmerer et al. (2023) wurde die Beschränkung auf quasi-zweidimensionales Gelände zugunsten einer dreidimensionalen Orographie aufgehoben.

7.1 Turbulente Hangwinde in der konvektiven Grenzschicht über Orographie

Ein wesentliches Merkmal der vorliegenden Arbeit ist die Zerlegung der Strömung in einen kleinräumigen turbulenten Teil, eine lokale mittlere Zirkulation und eine großräumige Hintergrundströmung sowie die Unterscheidung zwischen turbulentem und advektivem Transport. Auf die primäre Fragestellung hin, das Verständnis des vertikalen Wärme- und Feuchteaustauschs in der konvektiven Grenzschicht über Gebirge zu verbessern, wurden zahlreiche neue Erkenntnisse gewonnen, die in zukünftige Diskussionen einbezogen werden sollten. Sie beziehen sich hauptsächlich auf die wolkenlose Grenzschicht in einem Gelände mit niedrigen Hügeln oder gemäßigten alpinen Tälern, wobei die Landoberfläche nicht allzu heterogen und die Bandbreite der Strömungsskalen auf kleinräumige Turbulenz, lokale Hangwinde und einen großräumigen Hintergrund-

wind beschränkt ist. Die ganze Vielfalt des Gebirgswindsystems in Hochgebirgsregionen mit seinen mesoskaligen Zirkulationen über orografischen Gegebenheiten unterschiedlichster Ausdehnung wird in dieser Studie nicht erfasst. Dennoch konnten wir selbst aus eher idealisierten numerischen Experimenten und meteorologischen Szenarien interessante Erkenntnisse gewinnen, denen wir ihre Allgemeingültigkeit nicht absprechen. Sie ergeben sich im Wesentlichen aus der Existenz eines zwischengeordneten Strömungsregimes, der Hangwindzirkulation, zwischen der turbulenten und der synoptischen Skala. Die wichtigsten Ergebnisse lassen sich wie folgt zusammenfassen:

- Die Hauptauswirkung der thermisch angetriebenen Hangwindzirkulation besteht darin, dass die Feuchte durch die Hangwindschicht aus dem Tal exportiert wird und sich über den Berggipfeln ansammelt. Dadurch entsteht ein horizontales Feuchtegefälle zwischen den Berghängen und der Talmitte. Im Gegensatz dazu ist die Temperaturverteilung mehr oder weniger horizontal homogen, da die Hangwindzirkulation direkt von den Temperaturgradienten angetrieben wird und auf deren Abbau hinwirkt. Wir haben gezeigt, dass dies auch für eine flachwellige Landschaft mit niedrigen Hügeln gilt und nicht auf tiefe, alpine Täler beschränkt ist.

- Im Zuge der Unterscheidung zwischen advektivem und turbulentem Transport wurde festgestellt, dass Feuchte hauptsächlich durch die Hangwinde transportiert wird, während turbulenter Austausch eine geringere Rolle für deren vertikalen Transfer spielt. Im Gegensatz dazu spielt die turbulente Durchmischung die Hauptrolle bei der Erwärmung der Grenzschicht. Die thermische Zirkulation dient hauptsächlich dem Ausgleich horizontaler Temperaturgradienten und trägt weniger zum vertikalen Wärmeaustausch bei. Weinkaemmerer et al. (2022a) behandelt auch die Turbulenzbudgets der turbulenten Flüsse und der turbulenten kinetischen Energie (TKE). Ein Vergleich der Budgets der turbulenten Flüsse zwischen Ebene und Gelände zeigt, dass die Gradient-Terme aufgrund zusätzlicher Advektion durch die Hangwinde reduziert sind. Im Falle des TKE-Budgets wirken diese zusätzlichen Transportterme als TKE-Senke im unteren Teil des Tals. Dies hängt jedoch wahrscheinlich vom konkreten Fall ab. Es ist ebenfalls vorstellbar, dass lokale Strömungen, wie z.B. Talwinde, eine Quelle für TKE darstellen, indem sie die turbulente Scherproduktion erhöhen.

- Ein zentrales Ergebnis dieser Arbeit, das in Weinkaemmerer et al. (2022a) beschrieben und in Weinkaemmerer et al. (2023) wieder aufgegriffen wurde, ist die Auswirkung eines Höhenwindes auf den vertikalen Wärme- und Feuchtetransport in der konvektiven Grenzschicht über komplexem Terrain. Ein Höhenwind

wirkt sich nur geringfügig auf das Temperaturprofil aus, da die Temperaturverteilung bereits relativ homogen ist. Dagegen hat er einen starken Einfluss auf die Feuchteverteilung, indem er den horizontalen Feuchtegradienten zwischen dem eher trockenen Talzentrum und der feuchten Hangregion durch Vermischung reduziert. Folglich führt ein Höhenwind zu einem verringerten vertikalen Feuchtetransfer durch die Hangwindschicht bis oberhalb der Kammhöhe, sodass mehr Feuchte im Tal verbleibt, auch wenn die Stärke der Hangwinde nicht wesentlich verringert wird. Somit kann er den Feuchteexport aus einem Tal in die freie Atmosphäre stark reduzieren. Ähnliche Ergebnisse wurden in einem realistischeren Experiment mit variablen Oberflächenflüssen erzielt, die durch ein interaktives, von der Sonneneinstrahlung abhängiges Landoberflächenmodell bestimmt wurden. Dies wurde auch über dreidimensionalem Terrain bestätigt. Darüber hinaus erzeugt ein Höhenwind eine Form von konvektiven Schwerewellen, indem er die Aufwinde auf den Bergkuppen überströmt. Dadurch weisen sie ebenfalls typische Merkmale stationärer orographischer Schwerewellen auf.

- Um das Prozessverständnis konvektiver Turbulenz über komplexem Gelände zu verbessern, konzentrierte sich Weinkaemmerer et al. (2023) auf die Identifizierung und Analyse kohärenter Plume-Strukturen über einem idealisierten Tal und über dreidimensionalem hügeligem Gelände. Es wurde festgestellt, dass kohärente Plume-Strukturen sowohl durch die thermischen Winde als auch durch den Hintergrundwind in der Höhe beeinflusst werden. In der Hangwindschicht bewegen sich die Plumes etwa mit der Geschwindigkeit des Hangwindes bergauf. Infolgedessen ist ihre Häufigkeit auf den Bergkämmen am höchsten, wo auch der mittlere Vertikalwind positiv ist. Im zeitlichen und räumlichen Mittel reduziert ein Höhenwind die Häufigkeit der Plumes vor allem auf den windzugewandten Hängen. Dies geht einher mit einem verringerten vertikalen Feuchtefluss, der hauptsächlich auf einen geringeren Feuchtegehalt in der Hangwindschicht zurückzuführen ist, was sich mit der oben genannten Feststellung deckt. Abbildung 6.1 veranschaulicht dieses Ergebnis. Im zeitlichen Mittel bleibt die aufwärts transportierte Feuchtigkeitsmenge im WIND3D-Fall geringer. Dies ist nicht nur über den Hügeln der Fall, auch der über das ganze Gebiet gemittelte Gesamtfeuchtefluss ist geringer als im REF3D-Fall.

- In der konvektiven Grenzschicht ist es üblich, zwischen lokaler turbulenter Vermischung mit diffusivem Charakter und nichtlokalem Transport durch Thermikblasen und Plumes zu unterscheiden. In einer gemeinsamen Häufigkeitsverteilung von turbulenten Vertikalwind- und Temperatur- oder Feuchtefluktuationen ist

zu erwarten, dass die diffusiven Beiträge symmetrisch angeordnet sind. Die nichtlokalen Komponenten des Vertikaltransports im Zusammenhang mit Plumes zeigen sich im asymmetrischen Anteil solcher Verteilungen. Mithilfe der aus den Modelldaten gewonnenen Häufigkeitsverteilungen lassen sich kontinuierliche gemeinsame Wahrscheinlichkeitsdichtefunktionen (Joint PDFs) ableiten. In der konvektiven Grenzschicht über komplexem Terrain kann die Form der Joint PDFs gut durch die thermische Zirkulation erklärt werden. Die Joint PDFs zeigen, dass die Advektion kohärenter turbulenter Strukturen durch die thermisch angetriebene Strömung ein wichtiger Prozess in der konvektiven Grenzschicht über Orographie ist. Im Allgemeinen sind die Plume-Strukturen hier weniger relevant, da die Hangwindzirkulation ein großes Gewicht hat. Außerdem wird das turbulente Entrainment am Oberrand der Grenzschicht teilweise durch die abwärts gerichteten Komponenten der Hangwindzirkulation ersetzt.

Aus diesen Ergebnissen wird deutlich, dass sich die konvektive Strömung über komplexem Gelände, selbst über niedrigen Hügeln, deutlich von der weithin beschriebenen flachen konvektiven Grenzschicht unterscheidet, bei der Energie und Masse hauptsächlich durch kleinskalige Turbulenz transportiert werden. Obwohl die Simulationen großteils idealisiert sind, gehen wir davon aus, dass die wichtigsten Ergebnisse auch in komplexeren, realen Situationen reproduziert werden können. Theoretisch sind diese Ergebnisse sogar über relativ kleinskaliger Orographie relevant, die in bestehenden Modellen zur numerischen Wettervorhersage (NWP) noch nicht aufgelöst ist. Die Ergebnisse für den Feuchtetransport sind auch auf Tracer oder Luftschadstoffe im Allgemeinen anwendbar.

Bei der Beantwortung der zweiten Hauptforschungsfrage, die darin bestand, Anregungen für Verbesserungen von Grenzschichtparametrisierungen zu geben und Kernpunkte für zukünftige Entwicklungen zu identifizieren, kann kein klarer Weg vorgezeichnet werden. Eine Möglichkeit, subgitterskalige Orographie zu berücksichtigen, die aus dem bestehenden ALPTHERM-Modell bekannt ist, besteht darin, die Flächen-Höhen-Verteilung einer bestimmten Region zu verwenden, d.h. die Landfläche pro Höhenstufe. Die Ergebnisse dieser Arbeit weisen jedoch darauf hin, dass es nicht vorteilhaft wäre, das Design einer Parametrisierung auf nur einen Parameter, wie den Topographic Amplification Factor, zu stützen. Insbesondere für den Feuchteaustausch wurde festgestellt, dass die vertikalen Flüsse in der konvektiven Grenzschicht über Gebirgen stark durch den advektiven, nicht-linearen Transport durch die Hangwindzirkulation beeinflusst werden. Die Parametrisierung der Flusskomponente, die von den Hangwinden beigetragen wird, wäre eine große Herausforderung, nicht nur weil analytische Modelle des Hangwindsystems im Allgemeinen stark vereinfacht sind. Darüber hinaus stellt die

starke Empfindlichkeit des vertikalen Massentransports gegenüber dem großräumigen Wind über den Berggipfeln, die eine wichtige Erkenntnis dieser Arbeit ist, eine weitere ernsthafte Komplikation dar. Häufig enthalten Modelle für die konvektive Grenzschicht Bulk-Parametrisierungen von Grenzschicht-Plumes, um den nichtlokalen Transport zu berücksichtigen. Dieses Konzept kann nicht einfach auf komplexes Gelände übertragen werden, wenn man bedenkt, wie wichtig der Prozess der Advektion turbulenter Strukturen in Gegenwart thermisch angetriebener Zirkulationen ist. Zusammenfassend lässt sich sagen, dass das Fehlen eines nutzbaren analytischen Hangwindmodells und die Bandbreite der Wechselwirkungen, ausgehend von den Turbulenzstrukturen bis hin zur synoptischen Größenordnung, es erschweren, sich ein praktisch verwendbares Parametrisierungskonzept vorzustellen. Selbst wenn es möglich wäre, beispielsweise die kinetische Energie der Hangwindzirkulation in einen Parameter zu fassen, wie etwa die kinetische Energie der Zirkulation (CKE), die den Wärme- und Masseaustausch durch die thermisch induzierte Strömung bestimmt, würden diese Prozesse fast vollständig in der sogenannten Gray Zone liegen, d.h. teilweise aufgelöst und teilweise subgitterskalig sein. Daher wäre es schwierig, Ergebnisse zu erzielen, die von der Modellauflösung unabhängig sind.

Als ersten Schritt hin zu einer verbesserten Modellierung der konvektiven Grenzschicht in der numerischen Wettervorhersage schlagen wir vor, eine bestehende Parametrisierung für Simulationen auf der Kilometerskala anzupassen, in denen die Hangwinde bereits einigermaßen aufgelöst sind. Ein Turbulenzmodell könnte um die Advektion von parametrisierten Plume-Strukturen oder subgitterskaligen turbulenten Größen im Allgemeinen erweitert werden. Durch die Implementierung (horizontaler) Gradient-Terme könnte der Einfluss der Hangwindzirkulation auf die Turbulenz berücksichtigt werden. Ziel ist es, den Wärmetransport zu erleichtern, damit die lokale Grenzschichthöhe nicht überschätzt wird. Dies könnte genauso durch eine andere Art von Anpassung oder durch eine mehr oder weniger direkte Korrektur der Grenzschichthöhe erreicht werden. Wie unsere Simulationen gezeigt haben, spielt der Wärme- und Feuchtetransport in der relativ flachen Hangwindschicht eine wichtige Rolle. Hier kann der Wärmestrom von der Landoberfläche nicht direkt in lokales Grenzschichtwachstum umgesetzt werden.

7.2 Nebel-Simulation in der stabilen Grenzschicht: Einfluss von Auflösung und Numerik

In Weinkaemmerer et al. (2022b) sind wir zur stabilen Grenzschicht über hügeligem Gelände übergegangen. Eine Kurzfassung der wichtigsten Ergebnisse wird hier wiedergegeben, Einzelheiten sind in der Veröffentlichung zu finden. In der stabilen Grenz-

schicht über Orographie kann es durch die Wechselwirkung der geländefolgenden Vertikalkoordinate, deren Koordinatenflächen den oberen Wolkenrand schneiden, mit den diffusiven Eigenschaften des Advektionsschemas zu unerwünschter Nebelauflösung kommen. Die wichtigsten Ergebnisse der Sensitivitätstests mit verschiedenen horizontalen Auflösungen und verschiedenen Parametern für die Advektion lassen sich wie folgt zusammenfassen:

- Über Orographie ist die numerische Diffusion stärker auflösungsabhängig als über flachem Gelände. Der Liquid Water Path (LWP) ist bei gröberen Auflösungen stark reduziert. Für die realistische Simulation von Nebel und tiefen Wolken über Orographie wird empfohlen, die relevanten orographischen Strukturen durch $\mathcal{O}(30)$ Gitterpunkte darzustellen, um Fehler im Zusammenhang mit geländefolgenden Vertikalkoordinaten zu minimieren. Dies bedeutet, dass NWP-Simulationen auf der Kilometerskala im Allgemeinen nicht in der Lage sind, genaue Ergebnisse über einem Gelände mit Strukturen von mehreren Kilometern Ausdehnung zu liefern. Mit einer optimierten Vertikalkoordinate und einem Advektionsschema höherer Ordnung können jedoch akzeptable Ergebnisse erzielt werden, wenn relevante Geländestrukturen durch $\mathcal{O}(10)$ Gitterpunkte dargestellt werden. Dies gilt für unseren Fall starker Windscherung. Bei schwächeren Winden könnte der Fehler geringer sein.

- Die Ordnung der skalaren Advektion hat einen starken Einfluss auf die Bildung von Nebel und tiefem Stratus. Für das in dieser Studie verwendete WENO-Schema scheint eine Ordnung von fünf oder sechs ein guter Kompromiss zu sein. Im untersuchten Fall erweist sich das WENO-Schema in der Tat als diffusiver als das reguläre Upwind-Schema. Ein Upwind- oder zentriertes Schema für die skalare Advektion kann für Wolkensimulationen mit starken Gradienten vorzuziehen sein.

- Die Wahl der geländefolgenden Vertikalkoordinate hat einen starken Einfluss auf die Entwicklung des Nebels. Eine beträchtliche Erhöhung des LWP kann bereits mit einer relativ einfachen Änderung der Koordinatendefinition erreicht werden.

- Der LWP hängt auch davon ab, wie gut kleinskalige turbulente Bewegungen aufgelöst werden, da sie eine vertikale Durchmischung an der Wolkenoberseite und folglich teilweise Wolkenauflösung verursachen. Das Verschwinden turbulenter Strukturen bei gröberen Auflösungen lässt also den LWP ansteigen, was die Nachteile der geländefolgenden Vertikalkoordinate teilweise kompensiert.

Es bleibt zu erwähnen, dass weitere Advektionsschemata, wie sie in operationellen NWP-Modellen verwendet werden, sowie alternative Möglichkeiten, Orographie in einem numerischen Modell zu definieren, wie z.B. Immersed-Boundary-Methoden, in dieser Untersuchung nicht berücksichtigt wurden.

7.3 Allgemeiner Ausblick

Aus den vorgestellten Studien geht hervor, dass nicht nur die Beschreibung von Grenzschichtprozessen durch bessere Parametrisierungen, sondern auch die Modelldynamik und die Darstellung der Orographie in den Modellen verbessert werden können. Im Allgemeinen nehmen die numerischen Fehler, z.B. durch das Advektionsschema und die Vertikalkoordinate, bei niedrigen Auflösungen zu. Auch Grenzschichtprozesse wie thermisch induzierte Zirkulationen werden bei einer zu geringen Modellauflösung nur unzureichend dargestellt. Folglich kann der vertikale Transport in der Grenzschicht nur ungenau simuliert werden. Obwohl kein konkretes Konzept für die Entwicklung einer Parametrisierung vorgestellt werden kann, sind wir zuversichtlich, dass die Ergebnisse dieser Arbeit eine gute Referenz für zukünftige Forschungen darstellen. Ein Punkt, der dem Autor dieser Dissertation wichtig ist, ist die Anwendbarkeit der Ergebnisse auf weniger idealisierte meteorologische Szenarien. Abgesehen von der starken Empfindlichkeit des Wärme- und Stofftransports über komplexem Gelände gegenüber thermisch angetriebenen Zirkulationen und gegenüber der großräumigen Strömung, ergeben sich in realistischer Umgebung weitere Schwierigkeiten. So gibt es z.B. Strahlungseffekte aufgrund von Abschattung oder unterschiedlichen Eigenschaften der Landoberfläche sowie Wechselwirkungen innerhalb des Gebirgswindsystems über mehrere Größenordnungen, z.B. Talwinde, die die Hangwindzirkulation beeinflussen. Ein weiterer wichtiger Punkt ist die Bildung von Wolken und damit von Niederschlag. Hier würden wir erwarten, dass die Ergebnisse dieser Dissertation einen bedeutenden Einfluss auf das Einsetzen von Wolkenbildung und die weitere Wolkenentwicklung über komplexem Gelände haben, insbesondere aufgrund des Einflusses der Hangwinde und des Höhenwindes auf den vertikalen Feuchtetransport. Nachdem sich Wolken über den Bergrücken gebildet haben, führt dies jedoch wiederum zu Rückwirkungen auf den Wärme- und Feuchtetransport, z.B. durch diabatische Prozesse und die Rückkopplung von Wolken auf den Strahlungshaushalt. Außerdem kann aus flacher Konvektion hochreichende Konvektion entstehen und nach Niederschlagsereignissen kann der Zustand der Talatmosphäre durch Cold-Pool-Bildung stark verändert sein. Ein interessanter nächster Schritt für künftige Projekte wäre es, die Ergebnisse dieser Arbeit in einer realen Fallstudie zu reproduzieren, vorzugsweise über einem größeren Gebiet

und mit höherer Orographie. Auf diese Weise wäre es möglich, die Bedeutung der Ergebnisse in realistischeren meteorologischen Situationen zu einzuschätzen.

Appendix A

CM1 implementations I: Budget computation

A.1 Online calculation of LES statistics

To compute the LES statistics in a post-processing step, it would be necessary to write out the complete data fields in 1 min intervals. In order to reduce the demand of disk space for model output, an additional module for online time averaging (`tmea.F`) has been implemented into CM1, meaning that the time averaging is done during the model run. The temporal average a_{tav} is calculated by recursion as follows:

$$a_{tav}^{n} = a_{tav}^{n-1} + \frac{1}{n}(a - a_{tav}^{n-1}). \tag{A.1}$$

Here, n is the current summation step. The responsible subroutine is called every 1 min. An output is only necessary at the end of every time period T. Before the output, additional spatial averaging of a_{tav} has to be carried out giving the ensemble average $\overline{a}$. If the ensemble averages $\overline{a}$, $\overline{b}$, and $\overline{ab}$ of the variables a and b are known, second-order moments can be calculated via:

$$\overline{a'b'} = \overline{ab} - \overline{a}\,\overline{b}, \tag{A.2}$$

which follows from Reynolds decomposition and averaging. For a third-order moment, the analogous expression reads:

$$\overline{a'b'c'} = \overline{abc} - \overline{a}\,\overline{b}\,\overline{c} - \overline{a}\,\overline{b'c'} - \overline{b}\,\overline{a'c'} - \overline{c}\,\overline{a'b'}. \tag{A.3}$$

The CM1 version used in this study is release 19.10 (CM1r19.10). Apart from `tmea.F`, the most important modules for the online time averaging, where changes had to be made, are

- `cm1.F`, the main program, containing the big time loop, from which all relevant routines for the initialization and the program run are called, and
- `writeout.F`, the output module, where the output data from the multiple MPI processes are gathered and written to the output file.

Within the next section, the relevant steps for the implementation of the online time-averaging module are introduced.

1. Several new **global variables** had to be defined. The most important are
   - the namelist parameters `dotmea` and `tmeafrq` defined in `input.F` representing the main switch for the online time averaging and the calling frequency, respectively. The total averaging period is given by the existing namelist parameter `tapfrq`, the frequency of the three-dimensional model output. Additional namelist parameters have to be broadcast to every MPI process via `MPI_BCAST` in `param.F`. Furthermore
   - `ntmea2d` and `ntmea`, the total number of two and three-dimensional `tmea` variables, respectively, defined in `input.F`, and
   - `ncalctm`, the number of the current summation step, `tmeatim`, the calling time of the coming `tmea` call, `desc_tmea`, `name_tmea`, and `unit_tmea`, string-like lists of short descriptions on every `tmea` variable, `dotmcalc`, an internal switch used within every time step, and `tmea`, the actual three-dimensional array of `tmea` variables. All defined in `cm1.F`.
2. In the **model-initialization** section of `cm1.F`, the routine `setup_tmea`, one of two routines out of `tmea.F`, is called. It initializes the `tmea` variables according to the following pattern:

   ```
   ntmea = ntmea + 1
   name_tmea(ntmea+ntmea2d) = 'tha_TM '
   desc_tmea(ntmea+ntmea2d) = 'TM potential temperature'
   unit_tmea(ntmea+ntmea2d) = 'K'
   ```

   Here, exemplarily, for the potential temperature without background. After that, the `tmea` array can be allocated to its required length given by `ntmea` and `ntmea2d`. In a similar way, the `tmea` variables are added to the model output variables in the existing routine `setup_output` in the module `writeout.F`. With

that, the additional variables are automatically part of the model output and can be seen just as standard model variables. The spatial averaging takes place after the complete three-dimensional data fields are gathered from all MPI processes.

3. During the **model run**, when the model time reaches `tmeatim` so that the switch `dotmcalc` is activated, the routine `calc_tmea` out of `tmea.F` is called. Basically, it consists of a big loop going through all the `tmea` variables in the form of a long list of `(else)if`-statements in which the next summation step is carried out:

```
elseif (trim(name_tmea(n)).eq.'tha_TM') then
  do k=1,maxk
  do j=1,nj
  do i=1,ni
    tmea(i,j,k,n)=tmea(i,j,k,n)+(tha(i,j,k)-tmea(i,j,k,n))/dble(ncalctm)
  enddo
  enddo
  enddo
```

Here, `n` is the loop index of the loop over the `tmea` variables and `i`, `j`, `k` are the indices in zonal, meridional, and vertical direction, respectively. After each output, the `tmea` array is set to zero again.

A.2 Budgets for heat and moisture

The evolution of temperature and humidity needs to be quantified with the help of their budget equations. Because the vertical transport over complex terrain involves different scales, we want to analyze transport contributions separated into turbulent motion, local circulation and large-scale flow. We insert the flow decomposition $a = \langle\overline{a}\rangle + \overline{a}_c + a'$ into a simplified Boussinesq set-of-equations neglecting rotation, viscous effects, and molecular diffusion, and subsequently apply the operators for ensemble and domain averaging ($\overline{a}$ and $\langle\overline{a}\rangle$). This leads to the domain-averaged budget equations for potential temperature and specific humidity:

$$\frac{\partial\langle\overline{\theta}\rangle}{\partial t} = -\left\langle \overline{u}_j \frac{\partial\overline{\theta}}{\partial x_j} \right\rangle - \left\langle \overline{u'_j \frac{\partial\theta'}{\partial x_j}} \right\rangle + \langle\overline{S_\theta}\rangle, \tag{A.4}$$

$$\frac{\partial\langle\overline{q}\rangle}{\partial t} = \underbrace{-\left\langle \overline{u}_j \frac{\partial\overline{q}}{\partial x_j} \right\rangle}_{\text{CIRC}} \underbrace{- \left\langle \overline{u'_j \frac{\partial q'}{\partial x_j}} \right\rangle}_{\text{TURB}} + \underbrace{\langle\overline{S_q}\rangle}_{\text{PHYSICS}} . \tag{A.5}$$

The first term on the rhs is the advective transport by the mean flow. In absence of large-scale gradients (or in a periodic setup, as in this study), it reduces to a local

transport by the mean circulation (CIRC). The second and the third expression are the turbulent transport term (TURB) and remaining source or sink terms from the model physics, respectively. In CM1, the above terms are obtained internally from the fully compressible model equations. No additional approximation is applied. It has to be paid attention that all dynamics and physics contributions are taken from the same point in time in order to guarantee that the budgets are closed.

A.3 Second-order turbulent moments

Analogously, budget equations for higher-order moments can be derived. In the following, the TKE equation for the idealized-valley case is presented as an example for a second-order turbulent moment. Unlike its canonical form (e.g., Stull, 2012), additional terms arise due to the separation of the local-circulation components $\overline{a}_c$:

$$\frac{1}{2}\frac{\partial\langle\overline{u_i'^2}\rangle}{\partial t} = \underbrace{\frac{g}{\theta_{v,0}}\langle\overline{w'\theta_v'}\rangle}_{\mathrm{I}} - \underbrace{\langle\overline{u_i'w'}\rangle\frac{\partial u_{B,i}}{\partial z}}_{\mathrm{II}} - \underbrace{\left\langle\overline{u_i'u_j'}\frac{\partial\overline{u}_{c,i}}{\partial x_j} + \overline{u}_{c,j}\frac{1}{2}\frac{\partial\overline{u_i'^2}}{\partial x_j}\right\rangle}_{\mathrm{III}} - \underbrace{\frac{1}{2}\frac{\partial\langle\overline{w'u_i'^2}\rangle}{\partial z}}_{\mathrm{IV}} - \underbrace{\frac{1}{\rho_0}\frac{\partial\langle\overline{w'p'}\rangle}{\partial z}}_{\mathrm{V}} - \underbrace{\langle\epsilon\rangle}_{\mathrm{VI}}, \quad \text{(A.6)}$$

where $j = 1, 3$ and $\overline{u}_{c,2} = 0$, as there is no mean circulation in the along-valley direction. The scale-transfer terms are grouped in III describing the interaction between turbulence and local circulation. The two components of III represent the shear production and the advective transport of TKE by the slope-wind circulation. The other terms are the canonical terms: I, buoyant production/consumption, II, large-scale gradient production, IV, vertical turbulent transport, V, pressure correlation, and VI, dissipation.

As a part of the online time-averaging module, most of the budget terms are calculated during the model run. This is possible as the different terms of the prognostic equations are available internally in the model. For instance, the budget terms of the vertical velocity are grouped in the variable `wdiag`, the buoyant term is accessible via `wdiag(i,j,k,wd_buoy)` (buoyancy only has a non-zero contribution in the vertical direction). With that, the buoyant production/consumption term of Eq. (A.6) can be obtained from `wa(i,j,k)` and `wdiag(i,j,k,wd_buoy)` inserted into Eq. (A.2) as a and b leading to the buoyancy flux. Here, `wa` is the corresponding value for the vertical wind available in the module `solve.F`. This way of computing the TKE budget terms only allows the calculation of a general transport term TRT = II + III + IV

based on the horizontal and vertical advection terms `wdiag(i,j,k,wd_hadv)` and `wdiag(i,j,k,wd_vadv)`, respectively (as well as the contributions from `udiag` and `vdiag`). In order to decompose it any further, single terms have to be computed in the post-processing.

Appendix B

CM1 implementations II: Conditional sampling of plumes

For the identification of the plume structures, a conditional sampling method has been implemented into CM1. This was done according to Couvreux et al. (2010). It uses a passive tracer emitted at the surface. The tracer decays over time in order to ensure that it does not accumulate outside the updrafts. During the sampling, spatial averaging is necessary which is carried out along the symmetry axis of the valley in case of the periodic-valley setup or on 1.3 km wide square subdomains in case of the three-dimensional terrain. A grid point is sampled if the local vertical velocity w is positive and the tracer concentration anomaly c' exceeds the standard deviation of the tracer concentration σ_c along the valley axis (or on the subdomain, depending on the setup) and a minimum threshold $\sigma_{\min}$:

- $w > 0$,
- $c' > \max(\sigma_c, \sigma_{\min})$,

where c' is the deviation from the local spatial average. The minimum threshold is implemented as $\sigma_{\min} = (0.05/z) \int_0^z \sigma_c(z')\,\mathrm{d}z'$ (Couvreux et al., 2010). An example of the identified plume structures over the slope of a valley is shown in Fig. B.1.

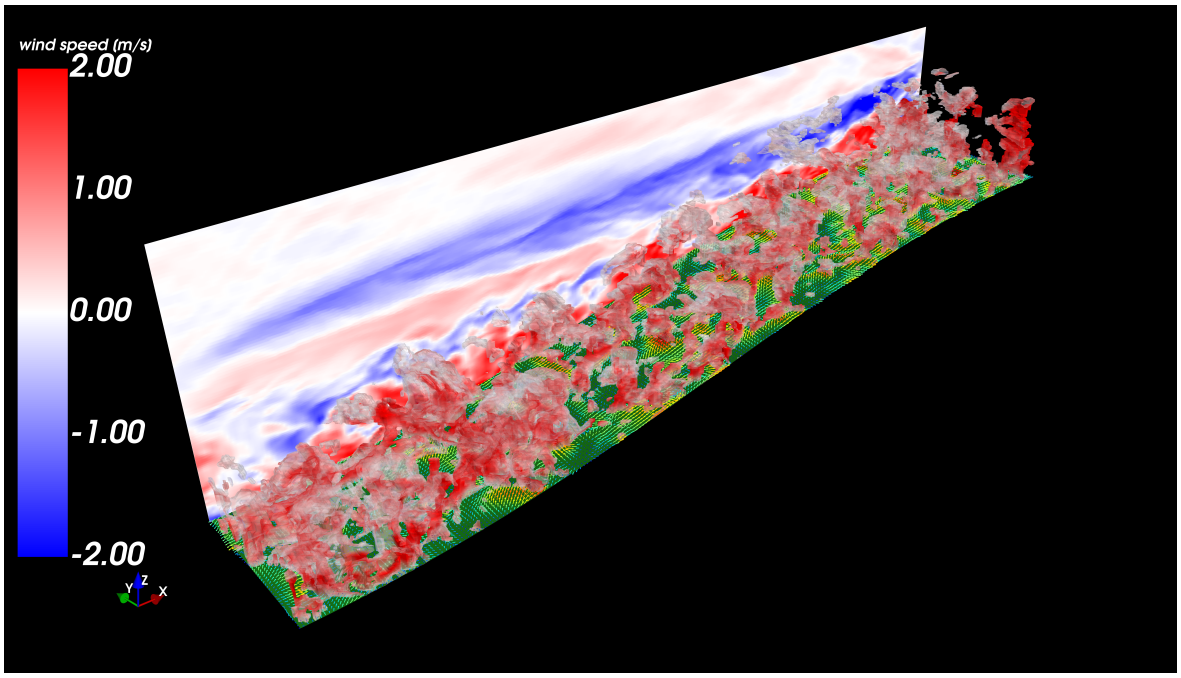

Figure B.1: Contours of the sampled plumes over one valley slope after 4 h simulation time (10 km in x, 2 km in y direction). The shading of the plumes correspond to the vertical wind speed. The backward plane shows the horizontal wind in x direction up to 3 km height, the arrows represent the 10 m wind.

Bibliography

Angevine, W. M., Jiang, H., and Mauritsen, T. (2010). Performance of an eddy diffusivity–mass flux scheme for shallow cumulus boundary layers. *Monthly Weather Review*, 138(7):2895–2912.

Banta, R. M. (1990). The role of mountain flows in making clouds. In *Atmospheric processes over complex terrain*, pages 229–283. Springer.

Berg, L. K. and Stull, R. B. (2004). Parameterization of joint frequency distributions of potential temperature and water vapor mixing ratio in the daytime convective boundary layer. *Journal of the atmospheric sciences*, 61(7):813–828.

Bergot, T. (2013). Small-scale structure of radiation fog: a large-eddy simulation study. *Quarterly Journal of the Royal Meteorological Society*, 139(673):1099–1112.

Bergot, T., Escobar, J., and Masson, V. (2015). Effect of small-scale surface heterogeneities and buildings on radiation fog: Large-eddy simulation study at paris–charles de gaulle airport. *Quarterly Journal of the Royal Meteorological Society*, 141(686):285–298.

Bergot, T. and Lestringant, R. (2019). On the predictability of radiation fog formation in a mesoscale model: a case study in heterogeneous terrain. *Atmosphere*, 10(4):165.

Borges, R., Carmona, M., Costa, B., and Don, W. S. (2008). An improved weighted essentially non-oscillatory scheme for hyperbolic conservation laws. *Journal of Computational Physics*, 227(6):3191–3211.

Boutle, I., Angevine, W., Bao, J.-W., Bergot, T., Bhattacharya, R., Bott, A., Ducongé, L., Forbes, R., Goecke, T., Grell, E., et al. (2022). Demistify: a large-eddy simulation (les) and single-column model (scm) intercomparison of radiation fog. *Atmospheric Chemistry and Physics*, 22(1):319–333.

Boutle, I., Finnenkoetter, A., Lock, A., and Wells, H. (2016). The london model: forecasting fog at 333 m resolution. *Quarterly Journal of the Royal Meteorological Society*, 142(694):360–371.

Boutle, I., Price, J., Kudzotsa, I., Kokkola, H., and Romakkaniemi, S. (2018). Aerosol–fog interaction and the transition to well-mixed radiation fog. *Atmospheric Chemistry and Physics*, 18(11):7827–7840.

Brient, F., Couvreux, F., Villefranque, N., Rio, C., and Honnert, R. (2019). Object-oriented identification of coherent structures in large eddy simulations: Importance of downdrafts in stratocumulus. *Geophysical Research Letters*, 46(5):2854–2864.

Brown, A. R., MacVean, M. K., and Mason, P. J. (2000). The effects of numerical dissipation in large eddy simulations. *Journal of the atmospheric sciences*, 57(19):3337–3348.

Bryan, G. H. (2016). The governing equations for cm1. *Technical Note. UCAR, Boulder, CO*.

Bryan, G. H. and Fritsch, J. M. (2002). A benchmark simulation for moist nonhydrostatic numerical models. *Monthly Weather Review*, 130(12):2917–2928.

Calaf, M., Vercauteren, N., Katul, G. G., Giometto, M. G., Morrison, T. J., Margairaz, F., Boyko, V., and Pardyjak, E. R. (2022). Boundary-layer processes hindering contemporary numerical weather prediction models. *Boundary-Layer Meteorology*, pages 1–26.

Catalano, F. and Moeng, C.-H. (2010). Large-eddy simulation of the daytime boundary layer in an idealized valley using the weather research and forecasting numerical model. *Boundary-layer meteorology*, 137(1):49–75.

Chinita, M. J., Matheou, G., and Teixeira, J. (2018). A joint probability density-based decomposition of turbulence in the atmospheric boundary layer. *Monthly Weather Review*, 146(2):503–523.

Chou, M.-D. and Suarez, M. J. (1999). A solar radiation parameterization for atmospheric studies. Technical report.

Chow, F. K., Schär, C., Ban, N., Lundquist, K. A., Schlemmer, L., and Shi, X. (2019). Crossing multiple gray zones in the transition from mesoscale to microscale simulation over complex terrain. *Atmosphere*, 10(5):274.

Clark, T. L., Hauf, T., and Kuettner, J. P. (1986). Convectively forced internal gravity waves: Results from two-dimensional numerical experiments. *Quarterly Journal of the Royal Meteorological Society*, 112(474):899–925.

Couvreux, F., Hourdin, F., and Rio, C. (2010). Resolved versus parametrized boundary-layer plumes. part i: A parametrization-oriented conditional sampling in large-eddy simulations. *Boundary-layer meteorology*, 134(3):441–458.

Deardorff, J. W. (1980). Stratocumulus-capped mixed layers derived from a three-dimensional model. *Boundary-layer meteorology*, 18(4):495–527.

Demko, J. C. and Geerts, B. (2010a). A numerical study of the evolving convective boundary layer and orographic circulation around the santa catalina mountains in arizona. part i: Circulation without deep convection. *Monthly weather review*, 138:1902–1922.

Demko, J. C. and Geerts, B. (2010b). A numerical study of the evolving convective boundary layer and orographic circulation around the santa catalina mountains in arizona. part ii: Interaction with deep convection. *Monthly weather review*, 138(9):3603–3622.

Demko, J. C., Geerts, B., Miao, Q., and Zehnder, J. A. (2009). Boundary layer energy transport and cumulus development over a heated mountain: An observational study. *Monthly weather review*, 137(1):447–468.

Forthun, G. M., Johnson, M. B., Schmitz, W. G., Blume, J., and Caldwell, R. J. (2006). Trends in fog frequency and duration in the southeast united states. *Physical Geography*, 27(3):206–222.

Geerts, B., Miao, Q., and Demko, J. C. (2008). Pressure perturbations and upslope flow over a heated, isolated mountain. *Monthly weather review*, 136(11):4272–4288.

Giovannini, L., Ferrero, E., Karl, T., Rotach, M. W., Staquet, C., Trini Castelli, S., and Zardi, D. (2020). Atmospheric pollutant dispersion over complex terrain: Challenges and needs for improving air quality measurements and modeling. *Atmosphere*, 11(6):646.

Göbel, M., Serafin, S., and Rotach, M. (2023). Adverse impact of terrain steepness on thermally-driven initiation of orographic convection. *In preparation*.

Gohm, A., Harnisch, F., Vergeiner, J., Obleitner, F., Schnitzhofer, R., Hansel, A., Fix, A., Neininger, B., Emeis, S., and Schäfer, K. (2009). Air pollution transport in an alpine valley: Results from airborne and ground-based observations. *Boundary-layer meteorology*, 131(3):441–463.

Griewank, P. J., Heus, T., and Neggers, R. A. (2022). Size-dependent characteristics of surface-rooted three-dimensional convective objects in continental shallow cumulus simulations. *Journal of Advances in Modeling Earth Systems*, 14(3):e2021MS002612.

Gultepe, I., Sharman, R., Williams, P. D., Zhou, B., Ellrod, G., Minnis, P., Trier, S., Griffin, S., Yum, S. S., Gharabaghi, B., et al. (2019). A review of high impact weather for aviation meteorology. *Pure and applied geophysics*, 176(5):1869–1921.

Gultepe, I., Tardif, R., Michaelides, S., Cermak, J., Bott, A., Bendix, J., Müller, M. D., Pagowski, M., Hansen, B., Ellrod, G., et al. (2007). Fog research: A review of past achievements and future perspectives. *Pure and applied geophysics*, 164(6):1121–1159.

Henne, S., Furger, M., Nyeki, S., Steinbacher, M., Neininger, B., De Wekker, S., Dommen, J., Spichtinger, N., Stohl, A., and Prévôt, A. S. (2004). Quantification of topographic venting of boundary layer air to the free troposphere. *Atmospheric Chemistry and Physics*, 4(2):497–509.

Henne, S., Furger, M., and Prévôt, A. H. (2005). Climatology of mountain venting–induced elevated moisture layers in the lee of the alps. *Journal of Applied Meteorology and Climatology*, 44(5):620–633.

Heus, T. and Jonker, H. J. (2008). Subsiding shells around shallow cumulus clouds. *Journal of the Atmospheric Sciences*, 65(3):1003–1018.

Hundsdorfer, W., Koren, B., Verwer, J., et al. (1995). A positive finite-difference advection scheme. *Journal of computational physics*, 117(1):35–46.

Iacono, M. J., Delamere, J. S., Mlawer, E. J., Shephard, M. W., Clough, S. A., and Collins, W. D. (2008). Radiative forcing by long-lived greenhouse gases: Calculations with the aer radiative transfer models. *Journal of Geophysical Research: Atmospheres*, 113(D13).

Jiang, G.-S. and Shu, C.-W. (1996). Efficient implementation of weighted eno schemes. *Journal of computational physics*, 126(1):202–228.

Jiménez, P. A., Dudhia, J., González-Rouco, J. F., Navarro, J., Montávez, J. P., and García-Bustamante, E. (2012). A revised scheme for the wrf surface layer formulation. *Monthly weather review*, 140(3):898–918.

Kirshbaum, D. J., Adler, B., Kalthoff, N., Barthlott, C., and Serafin, S. (2018). Moist orographic convection: Physical mechanisms and links to surface-exchange processes. *Atmosphere*, 9(3):80.

Köhler, C., Steiner, A., Saint-Drenan, Y.-M., Ernst, D., Bergmann-Dick, A., Zirkelbach, M., Bouallègue, Z. B., Metzinger, I., and Ritter, B. (2017). Critical weather situations for renewable energies–part b: Low stratus risk for solar power. *Renewable Energy*, 101:794–803.

Kuwagata, T. and Kimura, F. (1997). Daytime boundary layer evolution in a deep valley. part ii: Numerical simulation of the cross-valley circulation. *Journal of Applied Meteorology*, 36(7):883–895.

Larson, V. E. and Golaz, J.-C. (2005). Using probability density functions to derive consistent closure relationships among higher-order moments. *Monthly Weather Review*, 133(4):1023–1042.

Lehner, M. and Gohm, A. (2010). Idealised simulations of daytime pollution transport in a steep valley and its sensitivity to thermal stratification and surface albedo. *Boundary-layer meteorology*, 134(2):327–351.

Lehner, M. and Rotach, M. W. (2018). Current challenges in understanding and predicting transport and exchange in the atmosphere over mountainous terrain. *Atmosphere*, 9(7):276.

Leuenberger, D., Koller, M., Fuhrer, O., and Schär, C. (2010). A generalization of the SLEVE vertical coordinate. *Monthly Weather Review*, 138(9):3683–3689.

Leukauf, D., Gohm, A., and Rotach, M. W. (2016). Quantifying horizontal and vertical tracer mass fluxes in an idealized valley during daytime. *Atmospheric Chemistry and Physics*, 16(20):13049.

Liechti, O. and Neininger, B. (1994). Alptherm-a pc based model for atmospheric convection over complex topography. *Technical Soaring*, 18(3):73–78.

Lundquist, K. A., Chow, F. K., and Lundquist, J. K. (2010). An immersed boundary method for the weather research and forecasting model. *Monthly Weather Review*, 138(3):796–817.

Lunet, T., Lac, C., Auguste, F., Visentin, F., Masson, V., and Escobar, J. (2017). Combination of weno and explicit runge–kutta methods for wind transport in the meso-nh model. *Monthly Weather Review*, 145(9):3817–3838.

Marchesiello, P., Debreu, L., and Couvelard, X. (2009). Spurious diapycnal mixing in terrain-following coordinate models: The problem and a solution. *Ocean Modelling*, 26(3-4):156–169.

Matheou, G. and Teixeira, J. (2019). Sensitivity to physical and numerical aspects of large-eddy simulation of stratocumulus. *Monthly Weather Review*, 147(7):2621–2639.

Mazoyer, M., Lac, C., Thouron, O., Bergot, T., Masson, V., and Musson-Genon, L. (2017). Large eddy simulation of radiation fog: impact of dynamics on the fog life cycle. *Atmospheric Chemistry and Physics*, 17(21):13017–13035.

Morrison, H., Thompson, G., and Tatarskii, V. (2009). Impact of cloud microphysics on the development of trailing stratiform precipitation in a simulated squall line: Comparison of one-and two-moment schemes. *Monthly weather review*, 137(3):991–1007.

Nakanishi, M. (2000). Large-eddy simulation of radiation fog. *Boundary-layer meteorology*, 94(3):461–493.

Nakanishi, M. and Niino, H. (2006). An improved mellor–yamada level-3 model: Its numerical stability and application to a regional prediction of advection fog. *Boundary-Layer Meteorology*, 119(2):397–407.

Nappo, C. J. (2013). *An introduction to atmospheric gravity waves*. Academic press.

Neininger, B. (1982). *Mesoklimatische Messungen im Oberwallis*.

Neininger, B. and Liechti, O. (1984). Local winds in the upper rhone valley. *GeoJournal*, 8(2):265–270.

Nelson, T. C., Marquis, J., Peters, J. M., and Friedrich, K. (2022). Environmental controls on simulated deep moist convection initiation occurring during relampago-cacti. *Journal of the Atmospheric Sciences*.

Nemery, B., Hoet, P. H., and Nemmar, A. (2001). The meuse valley fog of 1930: an air pollution disaster. *The lancet*, 357(9257):704–708.

Nicholls, S. (1989). The structure of radiatively driven convection in stratocumulus. *Quarterly Journal of the Royal Meteorological Society*, 115(487):487–511.

Noppel, H. and Fiedler, F. (2002). Mesoscale heat transport over complex terrain by slope winds–a conceptual model and numerical simulations. *Boundary-layer meteorology*, 104(1):73–97.

Panosetti, D., Böing, S., Schlemmer, L., and Schmidli, J. (2016). Idealized large-eddy and convection-resolving simulations of moist convection over mountainous terrain. *Journal of the Atmospheric Sciences*, 73(10):4021–4041.

Pantano, C., Deiterding, R., Hill, D. J., and Pullin, D. I. (2007). A low numerical dissipation patch-based adaptive mesh refinement method for large-eddy simulation of compressible flows. *Journal of Computational Physics*, 221(1):63–87.

Pressel, K. G., Mishra, S., Schneider, T., Kaul, C. M., and Tan, Z. (2017). Numerics and subgrid-scale modeling in large eddy simulations of stratocumulus clouds. *Journal of advances in modeling earth systems*, 9(2):1342–1365.

Price, J. (2011). Radiation fog. part i: observations of stability and drop size distributions. *Boundary-layer meteorology*, 139(2):167–191.

Price, J. (2019). On the formation and development of radiation fog: an observational study. *Boundary-Layer Meteorology*, 172(2):167–197.

Randall, D. A., Shao, Q., and Moeng, C.-H. (1992). A second-order bulk boundary-layer model. *Journal of Atmospheric Sciences*, 49(20):1903–1923.

Raupach, M. (1981). Conditional statistics of reynolds stress in rough-wall and smooth-wall turbulent boundary layers. *Journal of Fluid Mechanics*, 108:363–382.

Rotach, M. W., Calanca, P., Graziani, G., Gurtz, J., Steyn, D. G., Vogt, R., Andretta, M., Christen, A., Cieslik, S., Connolly, R., et al. (2004). Turbulence structure and exchange processes in an alpine valley: The riviera project. *Bulletin of the American Meteorological Society*, 85(9):1367–1386.

Rotach, M. W., Wohlfahrt, G., Hansel, A., Reif, M., Wagner, J., and Gohm, A. (2014). The world is not flat: Implications for the global carbon balance. *Bulletin of the American Meteorological Society*, 95(7):1021–1028.

Schär, C., Leuenberger, D., Fuhrer, O., Lüthi, D., and Girard, C. (2002). A new terrain-following vertical coordinate formulation for atmospheric prediction models. *Monthly Weather Review*, 130(10):2459–2480.

Scherrer, S. C. and Appenzeller, C. (2014). Fog and low stratus over the swiss plateau-a climatological study. *International journal of climatology*, 34(3):678–686.

Schmidli, J. (2013). Daytime heat transfer processes over mountainous terrain. *Journal of the atmospheric sciences*, 70(12):4041–4066.

Schmidli, J., Poulos, G. S., Daniels, M. H., and Chow, F. K. (2009). External influences on nocturnal thermally driven flows in a deep valley. *Journal of applied meteorology and climatology*, 48(1):3–23.

Schmidli, J. and Rotunno, R. (2010). Mechanisms of along-valley winds and heat exchange over mountainous terrain. *Journal of the atmospheric sciences*, 67(9):3033–3047.

Schumann, U. and Moeng, C.-H. (1991). Plume fluxes in clear and cloudy convective boundary layers. *Journal of Atmospheric Sciences*, 48(15):1746–1757.

Serafin, S., Adler, B., Cuxart, J., De Wekker, S. F., Gohm, A., Grisogono, B., Kalthoff, N., Kirshbaum, D. J., Rotach, M. W., Schmidli, J., et al. (2018). Exchange processes in the atmospheric boundary layer over mountainous terrain. *Atmosphere*, 9(3):102.

Serafin, S. and Zardi, D. (2010). Daytime heat transfer processes related to slope flows and turbulent convection in an idealized mountain valley. *Journal of the Atmospheric Sciences*, 67(11):3739–3756.

Shu, C.-W. (1998). Essentially non-oscillatory and weighted essentially non-oscillatory schemes for hyperbolic conservation laws. In *Advanced numerical approximation of nonlinear hyperbolic equations*, pages 325–432. Springer.

Siebesma, A. and Cuijpers, J. (1995). Evaluation of parametric assumptions for shallow cumulus convection. *Journal of Atmospheric Sciences*, 52(6):650–666.

Siebesma, A. P., Soares, P. M., and Teixeira, J. (2007). A combined eddy-diffusivity mass-flux approach for the convective boundary layer. *Journal of the atmospheric sciences*, 64(4):1230–1248.

Simpson, J. and Wiggert, V. (1969). Models of precipitating cumulus towers. *Monthly Weather Review*, 97(7):471–489.

Skamarock, W. C. (2004). Evaluating mesoscale nwp models using kinetic energy spectra. *Monthly weather review*, 132(12):3019–3032.

Smith, D. K., Renfrew, I. A., Dorling, S. R., Price, J. D., and Boutle, I. A. (2021). Sub-km scale numerical weather prediction model simulations of radiation fog. *Quarterly Journal of the Royal Meteorological Society*, 147(735):746–763.

Steeneveld, G., Ronda, R., and Holtslag, A. (2015). The challenge of forecasting the onset and development of radiation fog using mesoscale atmospheric models. *Boundary-Layer Meteorology*, 154(2):265–289.

Steeneveld, G.-J. and de Bode, M. (2018). Unravelling the relative roles of physical processes in modelling the life cycle of a warm radiation fog. *Quarterly Journal of the Royal Meteorological Society*, 144(714):1539–1554.

Steinacker, R. (1984). Area-height distribution of a valley and its relation to the valley wind. *Beiträge zur Physik der Atmosphäre*, 57(1):64–71.

Stull, R. B. (2012). *An introduction to boundary layer meteorology*, volume 13. Springer Science & Business Media.

Teixeira, M. A., Kirshbaum, D. J., Ólafsson, H., Sheridan, P. F., and Stiperski, I. (2016). The atmosphere over mountainous regions.

Thompson, G., Field, P. R., Rasmussen, R. M., and Hall, W. D. (2008). Explicit forecasts of winter precipitation using an improved bulk microphysics scheme. part ii: Implementation of a new snow parameterization. *Monthly Weather Review*, 136(12):5095–5115.

Toy, M. D. (2013). A supercell storm simulation using a nonhydrostatic cloud-resolving model based on a hybrid isentropic-sigma vertical coordinate. *Monthly weather review*, 141(4):1204–1215.

Turner, J. (1962). The 'starting plume' in neutral surroundings. *Journal of Fluid Mechanics*, 13(3):356–368.

Van der Velde, I., Steeneveld, G., Schreur, B. W., and Holtslag, A. (2010). Modeling and forecasting the onset and duration of severe radiation fog under frost conditions. *Monthly weather review*, 138(11):4237–4253.

Vergeiner, I. and Dreiseitl, E. (1987). Valley winds and slope winds - observations and elementary thoughts. *Meteorology and Atmospheric Physics*, 36(1):264–286.

Wagner, J., Gohm, A., and Rotach, M. (2015). The impact of valley geometry on daytime thermally driven flows and vertical transport processes. *Quarterly Journal of the Royal Meteorological Society*, 141(690):1780–1794.

Wagner, J. S., Gohm, A., and Rotach, M. W. (2014). The impact of horizontal model grid resolution on the boundary layer structure over an idealized valley. *Monthly Weather Review*, 142(9):3446–3465.

Wang, S. and Stevens, B. (2000). Top-hat representation of turbulence statistics in cloud-topped boundary layers: A large eddy simulation study. *Journal of the atmospheric sciences*, 57(3):423–441.

Weigel, A. P., Chow, F. K., and Rotach, M. W. (2007). On the nature of turbulent kinetic energy in a steep and narrow alpine valley. *Boundary-layer meteorology*, 123:177–199.

Weigel, A. P. and Rotach, M. W. (2004). Flow structure and turbulence characteristics of the daytime atmosphere in a steep and narrow alpine valley. *Quarterly Journal of the Royal Meteorological Society: A journal of the atmospheric sciences, applied meteorology and physical oceanography*, 130(602):2605–2627.

Weinkaemmerer, J., Ďurán, I. B., and Schmidli, J. (2022a). The impact of large-scale winds on boundary layer structure, thermally driven flows, and exchange processes over mountainous terrain. *Journal of the Atmospheric Sciences*, 79(10):2685–2701.

Weinkaemmerer, J., Ďurán, I. B., Westerhuis, S., and Schmidli, J. (2022b). Stratus over rolling terrain: Large-eddy simulation reference and sensitivity to grid spacing and numerics. *Quarterly Journal of the Royal Meteorological Society*, 148(749):3528–3539.

Weinkaemmerer, J., Göbel, M., Serafin, S., Ďurán, I. B., and Schmidli, J. (2023). Boundary-layer plumes over mountainous terrain in idealized large-eddy simulations. *Submitted*.

Weissmann, M., Braun, F. J., Gantner, L., Mayr, G. J., Rahm, S., and Reitebuch, O. (2005). The alpine mountain–plain circulation: Airborne doppler lidar measurements and numerical simulations. *Monthly Weather Review*, 133(11):3095–3109.

Westerhuis, S. and Fuhrer, O. (2021). A locally smoothed terrain-following vertical coordinate to improve the simulation of fog and low stratus in numerical weather prediction models. *Journal of Advances in Modeling Earth Systems*, 13(8):e2020MS002437.

Westerhuis, S., Fuhrer, O., Bhattacharya, R., Schmidli, J., and Bretherton, C. (2021). Effects of terrain-following vertical coordinates on simulation of stratus clouds in numerical weather prediction models. *Quarterly Journal of the Royal Meteorological Society*, 147(734):94–105.

Westerhuis, S., Fuhrer, O., Cermak, J., and Eugster, W. (2020). Identifying the key challenges for fog and low stratus forecasting in complex terrain. *Quarterly Journal of the Royal Meteorological Society*, 146(732):3347–3367.

Whiteman, C. D. (2000). *Mountain meteorology: fundamentals and applications*. Oxford University Press.

Wicker, L. J. and Skamarock, W. C. (2002). Time-splitting methods for elastic models using forward time schemes. *Monthly weather review*, 130(8):2088–2097.

Williams, A. and Hacker, J. (1992). The composite shape and structure of coherent eddies in the convective boundary layer. *Boundary-layer meteorology*, 61(3):213–245.

Wyngaard, J. C. (2010). *Turbulence in the Atmosphere*. Cambridge University Press.

Wyngaard, J. C. and Moeng, C.-H. (1992). Parameterizing turbulent diffusion through the joint probability density. *Boundary-layer meteorology*, 60(1):1–13.

Xu, Z. and Shu, C.-W. (2005). Anti-diffusive flux corrections for high order finite difference weno schemes. *Journal of Computational Physics*, 205(2):458–485.

Zardi, D. and Serafin, S. (2015). An analytic solution for time-periodic thermally driven slope flows. *Quarterly Journal of the Royal Meteorological Society*, 141(690):1968–1974.

Zardi, D. and Whiteman, C. D. (2013). Diurnal mountain wind systems. *Mountain weather research and forecasting: Recent progress and current challenges*, pages 35–119.